

THE SOLID STATE CONVERSION REACTION OF COBALT OXIDE AND IRON FLUORIDE THIN FILMS

By

RYAN THORPE

A dissertation submitted to the
Graduate School—New Brunswick
Rutgers, The State University of New Jersey
in partial fulfillment of the requirements
for the degree of
Doctor of Philosophy
Graduate Program in Physics and Astronomy
written under the direction of
Robert A. Bartynski
and approved by

New Brunswick, New Jersey

October, 2016

ABSTRACT OF THE DISSERTATION

The Solid State Conversion Reaction of Cobalt Oxide and Iron Fluoride Thin Films

By RYAN THORPE

Dissertation Director:

Robert A. Bartynski

Iron (II) fluoride and cobalt (II) oxide are candidate electrode materials for a new class of rechargeable lithium ion batteries known as conversion batteries. Although the energy storage capacity of these materials represents a significant improvement over that of conventional electrode materials, many challenges must be overcome before conversion batteries can become commercially viable. Chief among these challenges is a loss of energy storage capacity as a function of the number of charge-discharge cycles. In this study, FeF_2 and CoO thin films have been studied as solid state analogues for lithium ion battery electrodes. These films were grown with different crystalline orientations and exposed to lithium in an ultra high vacuum chamber in order to simulate the discharge of a conversion electrode.

The electronic structure and chemical phase of the films before and after exposure to lithium were characterized using x-ray photoemission spectroscopy (XPS), ultraviolet photoemission spectroscopy (UPS), and inverse photoemission spectroscopy (IPS). The depth and homogeneity of the conversion reaction in the thin films was measured as a function of lithium exposure using angle-resolved XPS (ARXPS). The crystalline structure and morphology were studied using scanning tunneling microscopy (STM) and transmission electron microscopy (TEM).

For polycrystalline FeF_2 and CoO films, the products of the solid state conversion reactions were similar to those observed in electrochemical measurements. However, parasitic reaction pathways were identified for both reactions. The products of these reaction were found to inhibit the full conversion of the thin films, and are possibly responsible for the poor reaction kinetics in electrochemical cells. Furthermore, the diffusion of lithium into the FeF_2 and CoO surfaces, and the concomitant conversion reaction, was found to depend strongly on the orientation of the surface. These differences in diffusivity could partially be explained through geometric analyses of the crystalline structure of the films.

Acknowledgments

It takes a village to raise a PhD student, and this student is no exception. I owe a debt of gratitude to many people who have, in one way or another, made it possible for me to pursue my degree.

First and foremost I would like to thank my advisor, Bob Bartynski, whose knowledge about surface science is surpassed only by his patience. Bob first brought me into the lab as an undergraduate and has mentored me at every step of my education since then. I would also like to thank Sylvie Rangan, who has also been an invaluable teacher and an unofficial second advisor to me and many other graduate students. I also learned a great deal from the late Leszek Wielunski, who trusted me to run the tandem accelerator as a lowly undergraduate and gave me the confidence to pursue experimental physics as a graduate student.

I am grateful for my fellow Bartynski lab students Chaz Ruggieri, Senia Coh, Levan Tskipuri, and Eric Bersch, whose technical and moral support helped me get through the more difficult parts of my PhD. I am deeply indebted to Bill, Eric, and Ernie from the machine shop, who turned my napkin sketches into immaculately constructed pieces of equipment. I could devote an entire chapter of this thesis to the ways in which they helped me over the years.

My family has been a huge source of support over the years. I am forever grateful for my parents Wayne and Val and my siblings Eric, Sarah, and Adrienne, for teaching me to face adversity with a sense of humor. I am also grateful for my in-laws Dave, Julie, and Kelly, who taught me that running, hiking, and kayaking were great outlets for my frustrations. Finally, I would like to thank my wife, Alex, for her unconditional love and endless emotional support.

Dedication

To Alex, my wife and best friend.

Table of Contents

Abstract	ii
Acknowledgments	iv
Dedication	v
List of Tables	viii
List of Figures	ix
1. Introduction	1
1.1. Lithium Ion Batteries	1
1.2. Iron Fluoride and Cobalt Oxide as Electrode Materials	5
1.3. Thesis Outline	7
2. Experimental Methods	9
2.1. Introduction	9
2.2. Ultra High Vacuum	10
2.3. Sample Preparation	14
2.4. X-Ray Photoemission Spectroscopy	14
2.5. Ultraviolet and Inverse Photoemission Spectroscopy	24
2.6. Scanning Tunneling Microscopy	28
2.7. Transmission Electron Microscopy	30
2.8. Low Energy Electron Diffraction	32
2.9. Summary	34

3. Polycrystalline Iron Fluoride Films	35
3.1. Introduction	35
3.2. Sample preparation	35
3.3. Results	37
3.4. Conclusion	49
4. Epitaxial Iron Fluoride Films	51
4.1. Introduction	51
4.2. Sample Preparation	54
4.3. Results and Discussion	54
4.4. Conclusion	69
5. Polycrystalline Cobalt Oxide Films	70
5.1. Introduction	70
5.2. Sample preparation	71
5.3. Results and Discussion	72
5.4. Conclusion	87
6. Epitaxial Cobalt Oxide Films	89
6.1. Introduction	89
6.2. Sample Preparation and Characterization	89
6.3. Results and Discussion	98
6.4. Conclusion	113
Bibliography	114
Appendix A. Kinetic Theory of Gases	124
A.1. Monolayer Surface Contamination	124
A.2. Mean Free Path	127

List of Tables

1.1. Voltage, charge density, and energy density of selected electrode materials	5
4.1. Depth and homogeneity of the Li-FeF ₂ (110) reaction front for different amounts of Li exposure	66
4.2. Effective attenuation lengths of each iron compound calculated at normal emission using the NIST EAL Database.	68
6.1. Summary of ARXPS data for the Li-CoO(100) reaction	106
6.2. Summary of ARXPS data for the Li-CoO(111) reaction	112

List of Figures

1.1. Schematic of a Li-ion battery	2
2.1. Schematic of a rotary vane pump	11
2.2. Schematic of a turbomolecular pump	12
2.3. Schematic of an ion pump	13
2.4. Schematic of the photoemission process	15
2.5. Comparison of Co metal and CoO peak shapes	19
2.6. Angular dependence of the XPS signal	21
2.7. Schematic of a hemispherical analyzer	23
2.8. Schematic diagrams of UPS and IPS	26
2.9. IPS spectrum of polycrystalline FeF ₂	28
2.10. Schematic diagram of a scanning tunneling microscope	29
2.11. Schematic diagram of a transmission electron microscope	31
2.12. Schematic diagram of LEED	33
3.1. Ligand field splitting of Fe core levels	37
3.2. UPS and IPS spectra of a polycrystalline FeF ₂ thin film	38
3.3. Electronic structure of FeF ₂ during UPS and IPS	39
3.4. A d ⁵ Tanabe-Sugano diagram for an octahedral complex	40
3.5. A d ⁷ Tanabe-Sugano diagram for an octahedral complex	41
3.6. XPS spectra of the Fe 2p and F 1s core levels of polycrystalline FeF ₂	42
3.7. Peak fit of the Fe 2p _{3/2} core level of polycrystalline FeF ₂	43
3.8. TEM of a polycrystalline FeF ₂ thin film grown on SiO _x N _y	44
3.9. Evolution of the Fe 2p and F 1s core levels of FeF ₂ upon Li exposure	45
3.10. NRA spectrum from a fully lithiated polycrystalline FeF ₂ thin film	46
3.11. UPS and IPS spectra of a lithiated polycrystalline FeF ₂ thin film	47

3.12. TEM of a polycrystalline FeF_2 thin film after exposure to Li	48
4.1. Structure of FeF_2	52
4.2. XRR spectrum of $\text{FeF}_2(110)$ as grown	55
4.3. HIM image of an $\text{FeF}_2(110)$ film	56
4.4. XPS of $\text{FeF}_2(110)$ after degassing at 300°C in UHV	57
4.5. Fe 2p XPS spectrum of lithiated $\text{FeF}_2(110)$	58
4.6. Fe 2p XPS spectrum of $\text{FeF}_2(110)$ after 160 min of Li exposure	59
4.7. Evolution of the Fe 2p spectrum of $\text{FeF}_2(110)$ upon exposure to Li	61
4.8. Comparison of $R(\theta)$ and geometries for Li- $\text{FeF}_2(110)$ reaction	62
4.9. Linearized $R(\theta)$ plots for several different lithiations of $\text{FeF}_2(110)$	65
4.10. Detailed geometric model of the Li- FeF_2 reaction	67
5.1. Structure of CoO	72
5.2. XPS spectra of a polycrystalline CoO thin film	73
5.3. UPS and IPS of polycrystalline CoO	74
5.4. Ligand field splitting of Co core levels	75
5.5. TEM of polycrystalline CoO grown on SiO_xN_y	76
5.6. XPS spectra of polycrystalline CoO after a sequence of Li exposures	78
5.7. XPS spectra of a Cu sample after exposure to Li in UHV	79
5.8. TEM of polycrystalline CoO after lithiation at 150°C	81
5.9. Li 1s and Co 3p XPS spectra of lithiated CoO	83
5.10. Evolution of the CoO oxidation state with Li exposure	84
5.11. XPS spectra of an over-lithiated FeF_2 film	86
6.1. Schematics of the CoO(100) and (111) surfaces	90
6.2. STM of a clean Ag(100) surface	91
6.3. STM of CoO(100) films grown on Ag(100)	93
6.4. XPS of a CoO(100) film grown on Ag(100)	94
6.5. UPS spectrum of CoO(100)	95
6.6. STM of Ir(100) for several different surface treatments	96
6.7. STM of CoO(111) grown on Ir(100)	97

6.8. XPS of a CoO(111) film grown on Ir(100)	98
6.9. STM images of a 3 nm CoO(100) film after lithiation	99
6.10. STM images of a CoO(100) film before and after Li exposure	101
6.11. STM images of a fractional coverage CoO(100) film after lithiation	102
6.12. ARXPS spectra of lithiated CoO(100)	103
6.13. ARXPS data of CoO(100) for different Li exposures	105
6.14. Schematic of a CoO nanoparticle reaction	107
6.15. STM image of lithiated CoO(111)	108
6.16. STM image of lithiated CoO(111)	109
6.17. Structures of the CoO(111) and Li ₂ O(111) surfaces	110
6.18. ARXPS data of CoO(111) for different Li exposures	111
6.19. Schematic of a CoO nanoparticle reaction	113
A.1. A particle impinging on a surface	124
A.2. A particle moving through a gas	127

Chapter 1

Introduction

1.1 Lithium Ion Batteries

With the rise in popularity of portable electronic devices, electric/hybrid vehicles, and renewable energy generation in the past few decades, the need for high-capacity rechargeable (secondary) batteries has markedly increased. In stark contrast to data processing speed and memory storage capacity, battery capacity has failed to keep pace with Moore's law and is a limiting factor in many modern devices, motivating the search for new battery chemistries [1].

Lithium ion batteries are the most popular portable energy storage devices due to the high gravimetric and volumetric energy storage densities afforded by lithium, which has the lowest atomic weight of all metals [2]. A Li-ion battery consists of one or more electrochemical cells connected in series or parallel in order to produce the desired voltage and current output. Each cell consists of three main parts: the electropositive electrode (anode), the electronegative electrode (cathode), and the electrolyte, shown schematically in Figure 1.1. Both electrodes must be able to store lithium in either its elemental or ionic form and release it when driven either thermodynamically or electrically. The electrolyte is typically an insulating non-aqueous liquid containing a lithium salt, which facilitates the transfer of Li^+ ions while inhibiting electron transfer. During the discharge phase, positively charged lithium ions are thermodynamically driven from the anode to the cathode via the electrolyte. The details of the reaction energetics will be discussed in subsequent sections. In order to balance the transfer of electric charge, electrons are forced from the anode, through an external circuit, and into the cathode, thus generating an electric current. Recharging the battery is then accomplished by applying a negative bias to the cathode, thereby electrically driving electrons from the cathode to the anode. This forces Li^+ ions

to also flow back to the anode, where they are stored for the next discharge phase [3].

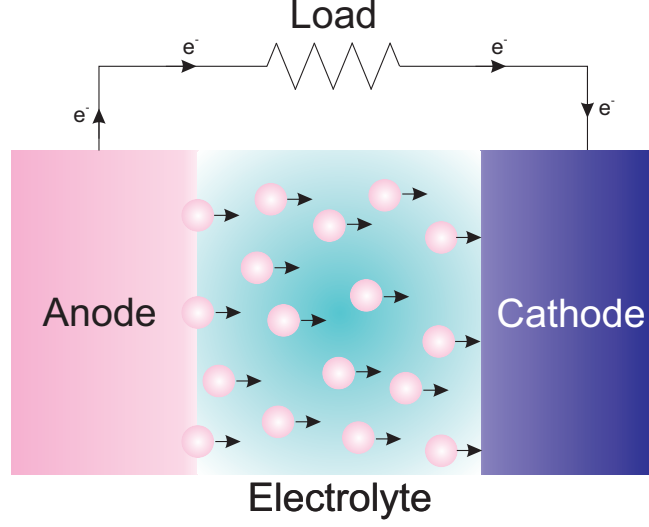
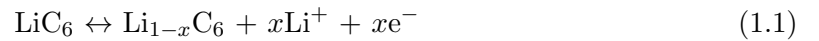


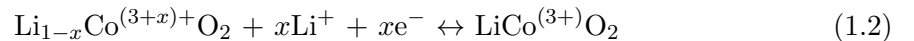
Figure 1.1: Schematic of a lithium ion battery during the discharge phase. Positive lithium ions are thermodynamically driven from the anode to the cathode, forcing negative electrons through an external circuit in order to balance the charge transfer.

1.1.1 Intercalation vs. Conversion

Modern lithium ion batteries are classified as intercalation batteries since they rely on the repeated insertion (intercalation) and removal of Li^+ ions from channels in both the cathode and the anode [4]. A typical Li-ion battery anode is composed of graphitic nanocomposites, which can accommodate Li intercalation between the loosely bound carbon sheets. The anodic half reaction can be written as

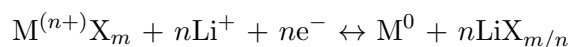


where the left-to-right reaction represents the discharge of the cell and right-to-left is the charging phase. The cathode usually consists of a layered lithium transition metal oxide, such as Li_xCoO_2 , where the value of x must be between 0.5 and 1 in order to preserve the structural integrity of the cathode material [4]. The cathodic half reaction can then be written as



using the same convention for the charge/discharge directions. For both electrodes, the insertion or removal of Li^+ ions does not significantly alter the crystalline structure of the constituent compound. This allows intercalation batteries to operate for hundreds or thousands of charge/discharge cycles without undergoing damage and losing significant amounts of charge storage capacity [5]. However, it is clear from the Equation 1.2 that the electrical current output of an intercalation cell is directly correlated to the change in oxidation state of the transition metal ion. This in turn is limited by the number of vacancies in the cathode that can accommodate lithium intercalation, which is usually 0.5 Li^+ per transition metal. Consequently, the charge storage capacity of intercalation batteries is intrinsically limited by the chemistry of the intercalation reaction, and significant improvements can only be made through the implementation of alternative reaction chemistries.

One alternative to intercalation-based electrodes is a so-called conversion cell, which relies on the complete reduction of a transition metal from a 2+ or 3+ oxidation state to its neutral (metallic) state in one or both electrodes, thereby accessing all available oxidation states of the metal [6]. In a conversion cathode, the half reaction reaction takes the form



where M is a transition metal; X=N, O, S, F; and m and n are integers between one and three [7–9]. Since the number n of Li^+ ions consumed by the cathode can be as high as 2-3 per formula unit, a conversion battery can theoretically store 4-6 times as much charge per transition metal ion as an intercalation battery can. However, this increase in charge storage comes at the cost of a decrease in material stability due to the structural reorganization of the electrode which accompanies the charge and discharge of the cell. The kinetic limitations imposed by these phase transitions have thus far prevented the implementation of conversion batteries.

1.1.2 Cell Voltage and Storage Capacity

The theoretical cell voltage or electromotive force (EMF) of a battery cell is determined by the Gibbs free energy of formation ($\Delta_f G$) of the reactants and the products of the full

(cathodic plus anodic) cell reaction. The value of $\Delta_f G$ is defined to be zero for elemental substances, e.g. nitrogen gas or graphite, and is negative for energetically stable compounds [3]. $\Delta_f G$ is typically expressed in kilojoules per mol of material, and is related to the EMF (E^0) of an electrochemical cell by the following equation:

$$\Delta_f G = -nFE^0 \quad (1.3)$$

where n is the number of electrons involved in the reaction, $F = eN_A$ is the Faraday constant which converts kJ/mol to eV/electron, and $N_A = 6.02 \times 10^{23} \text{ mol}^{-1}$ is Avogadro's number [3, 10]. An immediate results of this equation is that an electrochemical cell will only produce a voltage if the change in Gibbs free energy is negative during the discharge phase. In other words, the products must be more energetically favorable than the reactants [3]. However, the anodic discharge half reaction must have a *positive* value of $\Delta_f G$. That is, when isolated from the cell, the Li-rich phase of the anode must be more energetically stable than the Li-depleted phase. This is due to the need to avoid plating lithium metal during the charging phase of the electrochemical cell. Li metal dendrites have been known to form electrical shorts between the electrodes, leading to thermal runaway and, in some cases, combustion of the entire electrochemical cell [4]. Consequently, each electrode must have a negative value of $\Delta_f G$, i.e. a positive voltage, with respect to metallic lithium. Cathode materials should be optimized to produce the highest voltage possible, while anodes should have voltages close to zero in order to maximize the total voltage output of the cell.

Among the myriad combinations of potential conversion materials, only the transition metal fluoride compounds produce voltages ($E^0 = 1.9\text{-}3.5 \text{ V}$) that are high enough to warrant their use as cathode materials [9]. Metal nitrides, oxides, and sulfides produce lower voltages ($E^0 = 0.3\text{-}2.2 \text{ V}$) which are suitable for anodic applications. Table 1.1 shows a comparison of $\Delta_f G$, cell voltage, and capacity for two conversion compounds (FeF_2 and CoO), two intercalation compounds (LiCoO_2 and LiC_6), and several common conversion reaction products [10]. The values for the energy density assume that the electrode material is being used as a cathode, while the anode is lithium metal. From this table, it is clear that FeF_2 and CoO both outperform their intercalation-based counterparts in terms of charge

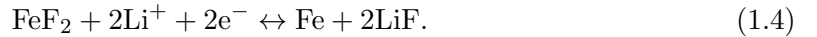
density when used as a cathode and anode respectively. Furthermore, these compounds both provide a significant improvement in the energy density over LiCoO_2 cathodes, despite their lower EMF values. These materials will be discussed in further detail in the following section.

Category	Compound	$\Delta_f G$ (kJ/mol)	EMF (V)	Charge Density (mAh/g)	Energy Density (Wh/g)
Cathodes	FeF_2	-663	-2.66	571	1.52
	LiCoO_2	-376	-3.90	272	0.79
Anodes	CoO	-214	-1.80	715	1.29
	LiC_6	-9.7	-0.10	372	-
Reaction Products	LiF	-589	-	-	-
	Li_2O	-562	-	-	-
	Li_2O_2	-578	-	-	-

Table 1.1: Gibbs free energy of formation, voltage, charge density, and energy density of FeF_2 , CoO , LiCoO_2 , and their relevant conversion reaction products. [10]

1.2 Iron Fluoride and Cobalt Oxide as Electrode Materials

Iron (II) fluoride-based nanocomposites have attracted significant attention for use as conversion cathodes, [11–13] Upon exposure to Li-ions in a conversion cell, the following reaction has been observed:

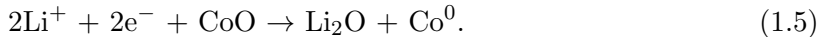


Prototype electrochemical cells based on carbon- FeF_2 nanocomposites have exhibited charge densities of more than 400 mAh/g, almost three times greater than the measured capacity of commercial LiCoO_2 cells (~ 140 mAh/g). [14] However, the capacity of FeF_2 cells quickly drops below 100 mAh/g over the course of 10 cycles, while most consumer batteries are expected to last for 1000 cycles or more. Additionally, slow reaction kinetics and a high voltage hysteresis have thus far prevented FeF_2 cells from becoming commercially viable. [14]

Many of the aforementioned issues have been attributed to the decomposition of the electrolyte at the cathode surface and subsequent formation of a passivating solid-electrolyte

interphase (SEI) layer. [14, 15] However, the drastic structural changes that accompany the charge and discharge of a conversion electrode could also lead to regions of active material being electronically or ionically insulated from the counterelectrode. Since Li-ion battery materials are typically studied as an aggregate system, i.e. cycling an electrochemical cell and then examining the components, [15–19] it is often difficult to separate fundamental electrode properties from electrolyte- or binder-related issues. To complement these previous studies, the following work uses a novel experimental approach, in which FeF_2 is studied independently of the other cell components.

The 3d transition metal oxides have attracted increasing attention as potential anode materials due to their stability, natural abundance, and the many methods by which they can be synthesized in nanostructured morphologies. [20–22] Their high gravimetric charge storage capacity and moderate voltage make metal oxides suitable for Li-ion anodes in applications where low voltage output and high charge density are required, e.g. mobile electronic devices. [10, 23] In particular, CoO has shown promising voltage output and capacity retention over dozens of cycles. In a study by Badway and coworkers, a CoO anode cycled with a LiCoO_2 cathode exhibited an output voltage of 2 V and a specific energy of 120 Wh/kg. [23] This compares well to the specific energy of 180 Wh/kg obtained for similar cells with LiC_6 anodes despite a significantly lower voltage output. Upon exposure to lithium, CoO undergoes the following two-electron conversion reaction: [24]



As with FeF_2 , the increased charge density of CoO electrodes comes at the expense of structural stability. While the morphology of intercalation compounds is largely unchanged by the incorporation of lithium ions, conversion materials undergo a phase separation that results in a total structural reorganization of the electrode. [9, 13] This pronounced change in morphology can lead to poor reaction kinetics and eventual capacity losses in an electrochemical cell. [7] These issues motivate the need for fundamental research into the reaction pathways involving Li and CoO.

1.3 Thesis Outline

The goal of this work is to characterize the Li-FeF₂ and Li-CoO conversion reactions without the need for counter-electrodes, electrolytes, binders, and other packaging materials. To that end, high-purity thin films of FeF₂ and CoO were prepared in ultra-high vacuum chambers and exposed to atomic lithium. The subsequent phase transformations and changes to the electronic structure of these materials were characterized using vacuum-based microscopy techniques (transmission electron microscopy and scanning tunneling microscopy) and photoelectron spectroscopies (x-ray photoelectron spectroscopy, ultraviolet photoemission spectroscopy, and inverse photoemission spectroscopy).

In Chapter 2, the vacuum-based experimental techniques mentioned in the preceding chapter are discussed, and the experimental setup is explained in detail. The theory behind photoemission is explained, with a particular emphasis on ARXPS, which is used extensively in subsequent chapters to obtain depth-resolved information from lithiated FeF₂ and CoO films.

Chapter 3 discusses the lithiation of FeF₂ nanoparticles, whose size, morphology, and electronic structure closely resembled the nanoparticle composites used in electrochemical cells. Despite the differences between this experimental design and a real Li-ion battery, the results obtained in this chapter closely mirror those seen in electrochemical cells. This chapter is based on Reference [25].

In Chapter 4, a more idealized FeF₂ system is considered. Epitaxially grown FeF₂(110) films were lithiated, in order to characterize the reactivity of this particular crystallographic orientation. The results of this study are found to agree with atomistic simulation in the literature. This chapter is based on Reference [26].

Chapter 5 is based on the work in Reference [27]. Following the experimental approach of Chapter 3, this chapter discusses the lithiation of polycrystalline CoO films. The behavior of the conversion reaction for these samples was found to be highly dependent upon the temperature at which the films were lithiated. Parasitic reaction pathways were identified as a significant factor in the Li diffusivity into the films.

Chapter 6 again uses more idealized samples in order to isolate the reactivities of different

CoO surfaces. For this chapter, epitaxial CoO(100) and (111) films were lithiated. The films were both found to follow the same conversion reaction as the polycrystalline CoO films. However, the diffusion of Li into these films and the subsequent geometry of the conversion reaction, was found to be drastically different between the two surface orientations. This is based on unpublished work. [28]

Chapter 2

Experimental Methods

2.1 Introduction

This thesis focuses on the reaction between lithium and thin films of cobalt oxide or iron fluoride. In order to maintain a clean sample surface and minimize parasitic reactions between lithium and external contaminants, all sample preparation, lithium exposures, and characterization were performed in an ultra-high vacuum (UHV) environment. The stoichiometry of the samples before and after exposure to lithium was probed with x-ray photoemission spectroscopy (XPS), while the band gap was measured using a combination of ultraviolet photoemission spectroscopy (UPS) and inverse photoemission spectroscopy (IPS). For epitaxial films, images of the pristine and partially reacted sample surfaces were acquired using scanning tunneling microscopy (STM). Angle-resolved XPS (ARXPS) was then used to obtain depth resolved chemical state information from the reacted films.

These measurements were performed in three different ultra high vacuum chambers whose base pressures were all below 1×10^{-9} Torr. XPS and some UPS measurements were performed in an ESCALAB 250Xi chamber, UPS/IPS measurements were performed in a home made vacuum chamber, and STM was performed using a Omicron VT Scanning Probe Microscope. When possible, CoO samples were grown and measured within a single chamber in order to prevent surface contamination from moisture or hydrocarbons. FeF₂ samples were all grown in separate chambers by collaborators before being transferred to the analysis chambers, necessitating some exposure to air. The subsequent sections will discuss some of the characteristics of UHV chambers and the theoretical and experimental details of the spectroscopy and microscopy techniques.

2.2 Ultra High Vacuum

Contamination on a sample surface mainly consists of water, hydroxyl groups, and organic species from exposure to air. [29] Simple calculations show that, assuming a sticking coefficient of one, the formation of one monolayer of surface contamination occurs within one nanosecond of exposure to gas at atmospheric pressure (See Appendix A for details). Since photoemission and microscopy experiments typically take hours or days ($10^4 - 10^5$ seconds) to complete, the pressure in a vacuum chamber must be a factor of $\sim 10^{13}$ lower than atmospheric pressure. This corresponds to a pressure of about 10^{-10} Torr. Additionally, a vacuum environment is necessary for experiments which use electrons, e.g. photoemission and inverse photoemission, since the mean free path of the electron must be long enough to reach the sample surface or the detector without interacting with gas particles. This necessitates a vacuum pressure of at least $10^{-5} - 10^{-6}$ Torr.

Achieving a vacuum of 10^{-10} Torr or lower requires a specialized chamber and the use of several types of pumps. UHV chambers are typically made of stainless steel and designed to have low internal surface areas to prevent the accumulation of water and other contamination. Chamber flanges are sealed by compressing copper gaskets between stainless steel knife edges on each side of the flange. Motion control in the chamber can be accomplished through the use of flexible bellows or magnetic coupling between internal and external components.

A typical pumping procedure for a vacuum chamber involves first pumping with a rotary vane pump through the flange of a turbomolecular pump. When the chamber pressure reaches 100 mTorr or lower, the turbomolecular pump may be turned on. The chamber will then pump to a pressure of $10^{-7} - 10^{-8}$ Torr over the course of several hours. In order to remove water vapor, grease, and other contaminants, the chamber is then baked (heated) to at least 100°C for a period of 12-72 hours. If ion pumps are used, they are typically heated to at least 250°C in order to remove the gases trapped in their walls. While baking, the chamber pressure increases drastically and then decreases slowly due to the evaporation and subsequent removal of volatile species. A pressure of $< 5 \times 10^{-8}$ while the chamber is hot typically indicates that the heating can be stopped. While the vacuum chamber is

cooling, the ion pump may be turned on, and various components of the chamber can be degassed. A description of each kind of vacuum pump is given below.

2.2.1 Rotary Vane Pumps

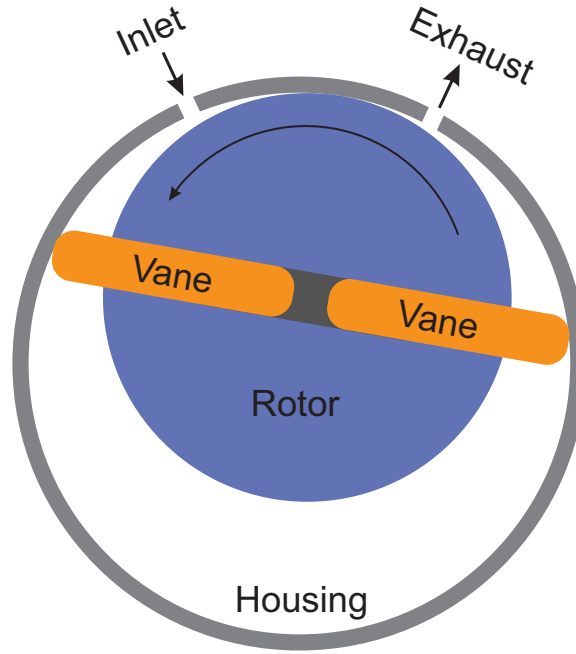


Figure 2.1: Schematic of a rotary vane pump

Figure 2.1 shows a schematic of a rotary vane pump. These pumps are designed to remove large volumes of gas from the vacuum chamber and operate at pressures as high as 1 Atmosphere (760 Torr). The main pumping mechanism in a rotary vane pumps consist of a cylindrical rotor enclosed within a cylindrical pump housing, also known as a stator. The axis of rotation of the rotor is parallel to the central axis of the housing, but offset (eccentric) so that the top of the rotor is within $2\text{-}3\text{ }\mu\text{m}$ of the inner wall of the housing. [30, 31]

Two rectangular blades known as vanes are held in a diametrical slot in the rotor and make contact with the inner walls of the housing. The vanes are pushed outward by a spring, thereby forming a seal with the housing and creating separate volumes which can increase and decrease in size as the rotor rotates. The entire rotor-housing assembly is submerged in oil in order to lubricate the moving parts and seal the interface between the vanes and the housing. [30]

When the rotor spins, the increasing volume between the rotor and the housing draws in gas from the inlet, while the decreasing volume expels gas through the exhaust. In a dual stage rotary vane pump, two assemblies are connected in series so that the exhaust of one assembly is connected to the inlet of another. [30] The ultimate pumping pressure of a rotary vane pump can be less than 10^{-3} Torr.

2.2.2 Turbomolecular Pumps

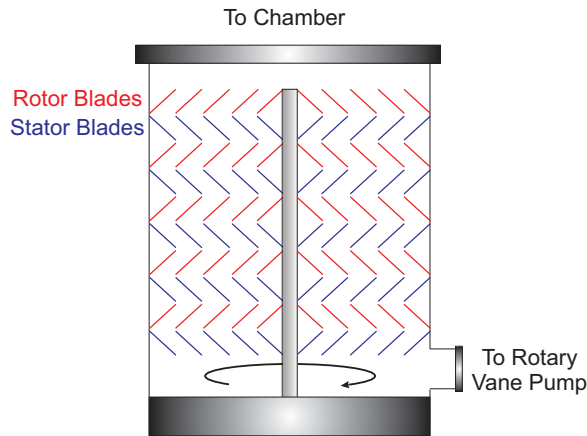


Figure 2.2: Schematic of a turbomolecular pump

Turbomolecular pumps operate at pressures below 10^{-3} Torr and are typically turned on after a chamber has been pumped for several minutes by a rotary vane pump. A turbomolecular pump consists of alternating sets of rotating and stationary angled blades, known as rotors and stators respectively, within a cylindrical housing. A schematic of this blade arrangement is shown in Figure 2.2. While pumping, rotors within a pump spin at 24,000 to 100,000 rotations per minute, transferring momentum to gas molecules in the direction of the pump outlet. [31] When the pump is running at full speed, each rotor or stator is capable of maintaining a pressure ratio of between 1.6 (for H_2) 4 (for Ar), and hence a set of 10 blades (5 rotors and 5 stators) can maintain a ratio of $100\text{-}10^6$ or greater between the intake flange of the pump to the outlet. [31] The pump outlet is typically connected to a rotary vane pump, and hence a chamber pressure of below 10^{-9} Torr can be achieved via this combination. Turbomolecular pumps are particularly adept at pumping heavy, nonreactive gases such as Ar and N_2 and are less effective at pumping light or reactive gases such

as H_2 and He .

2.2.3 Ion Pumps

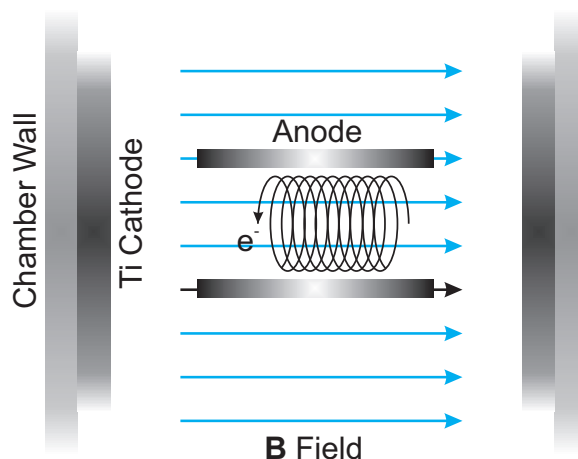


Figure 2.3: Schematic of an ion pump

Ion pumps are often used in vacuum chambers in which pressures below 10^{-9} Torr are required. An ion pump consists of two parallel Ti-coated cathode plates and an array of stainless steel cylindrical anode tubes, as shown in Figure 2.3. [30, 31] A strong magnetic field is applied along the axis of the anode cylinders. A voltage of up to 6 kV is applied between the cathode and anode, causing the emission of electrons from the anodes. These electrons follow helical paths through the ion pump. Collisions between these electrons and gas particles within the pump ionize the gas, which then follows a helical path before embedding into or chemisorbing onto the cathode walls. Ion pumps are useful for trapping reactive gases like H_2O and O_2 , but are not effective in removing nonreactive gases such as Ar and N_2 . The performance of ion pumps can be enhanced through the use of a titanium sublimation pump (TSP), which passes a high current through Ti filaments in order to sublime metallic Ti on the walls of the chamber. Since Ti metal is highly reactive, the freshly sublimated material is effective in trapping reactive gas molecules, notably water vapor and oxygen.

2.3 Sample Preparation

Several different crystalline orientations of FeF_2 and CoO were studied in order to characterize the reactivity of each surface. Polycrystalline FeF_2 samples were grown via a reaction of clean Fe foil with XeF_2 gas in vacuum. Epitaxial FeF_2 and CoO films were all grown with physical vapor deposition (PVD). The details of these sample growth techniques will be presented in subsequent chapters.

2.4 X-Ray Photoemission Spectroscopy

X-ray photoemission spectroscopy (XPS) is a powerful technique used to measure the elemental and chemical compositions of surfaces. The following section will discuss the physics underlying XPS with a particular focus on angle-resolved XPS (ARXPS).

2.4.1 The Photoelectric Effect

X-ray photoemission spectroscopy utilizes the photoelectric effect to probe the occupied electronic states in a material. In this work, all x-rays were produced using a monochromatic Al $K\alpha$ source with a primary energy of $h\nu = 1486.6$ eV. The angle between the x-ray source and the electron detector was 54° for all measurements.

The photoemission of an electron from the 1s core level of an atom is shown schematically in Figure 2.4. When an x-ray photon impinges on a material, it can impart its energy ($h\nu$) to a single electron. [29] If the photon energy is greater than the sum of the electron binding energy (BE) and the work function (ϕ_{sample}) of the material, then the electron can be ejected from the material with a kinetic energy (KE) given by

$$\text{KE} = h\nu - \text{BE} - \phi_{\text{sample}} - E_r \quad (2.1)$$

where E_r accounts for both the intra-atomic and solid state relaxation energies of the material in response to the loss of a photoelectron. [32] The photoelectron detector, often a channeltron, is typically connected electrically to the sample so that the Fermi energy (E_F) is equilibrated. This leads to a contact potential given by $\phi_{\text{sample}} - \phi_{\text{det}}$, which can either

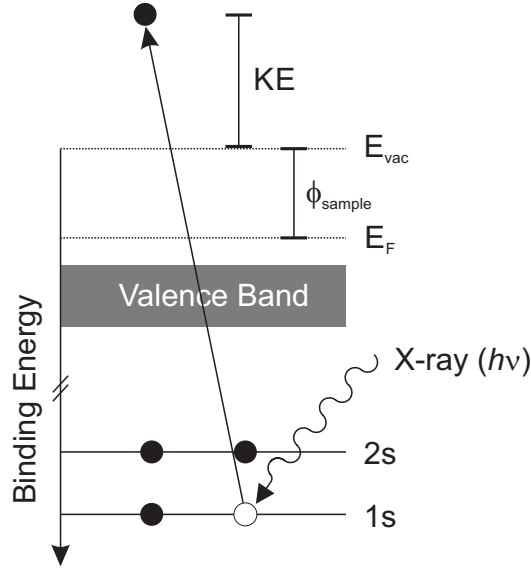


Figure 2.4: Schematic of the photoemission process

accelerate or retard photoelectrons as they move through the electron analyzer. [32] Hence, the kinetic energy of the electron upon reaching the detector is

$$KE = h\nu - BE - \phi_{\text{sample}} - (\phi_{\text{sample}} - \phi_{\text{det}}) - E_r \quad (2.2)$$

$$= h\nu - BE - \phi_{\text{det}} - E_r. \quad (2.3)$$

In practice, the detector work function is calibrated using a clean gold or silver samples so that the Fermi energy E_F lies at 0 eV. The binding energy of all electronic states can then defined using this reference. The relaxation energy can sometimes be neglected, but it has an important impact on the shape and energy distribution of XPS core level features, which will be discussed in subsequent sections.

2.4.2 The Photoionization Cross Section

The Hamiltonian of a bound electron in a solid can be expressed as

$$H_0 = \frac{\mathbf{p}^2}{2m} + V(\vec{r}) \quad (2.4)$$

where \mathbf{p} is the momentum operator and $V(\mathbf{r})$ is the electric potential. [32] The interaction of such an electron with an electromagnetic field $\mathbf{A}(\mathbf{r}, t) + \Phi(\mathbf{r}, t)$ can then be expressed as

$$H' = \frac{1}{2m} \left[\mathbf{p} - \frac{e}{c} \mathbf{A}(\mathbf{r}, t) \right]^2 + e\Phi(\mathbf{r}, t) + V(\mathbf{r}) \quad (2.5)$$

$$= \frac{1}{2m} \left[\mathbf{p}^2 - \frac{e}{c} (\mathbf{p} \cdot \mathbf{A} + \mathbf{A} \cdot \mathbf{p}) + \frac{e^2}{c^2} \mathbf{A}^2 \right] + e\Phi(\mathbf{r}, t) + V(\mathbf{r}) \quad (2.6)$$

$$= \frac{\mathbf{p}^2}{2m} + V(\mathbf{r}) + \frac{e}{2mc} [\mathbf{p} \cdot \mathbf{A} + \mathbf{A} \cdot \mathbf{p}] + \frac{e^2}{2mc^2} \mathbf{A}^2 + e\Phi(\mathbf{r}, t) \quad (2.7)$$

$$= H_0 + H_{\text{int}} \quad (2.8)$$

where

$$H_{\text{int}} = \frac{e}{2mc} [\mathbf{p} \cdot \mathbf{A} + \mathbf{A} \cdot \mathbf{p}] + \frac{e^2}{2mc^2} \mathbf{A}^2 + e\Phi(\mathbf{r}, t) \quad (2.9)$$

Since we are free to choose as gauge in which $\Phi = 0$ and \mathbf{A}^2 is negligibly small, the interaction Hamiltonian may be approximated as [32]

$$H_{\text{int}} = -\frac{e}{2mc} [\mathbf{p} \cdot \mathbf{A} + \mathbf{A} \cdot \mathbf{p}] \quad (2.10)$$

$$= -\frac{e}{2mc} [2\mathbf{A} \cdot \mathbf{p} + i\hbar \nabla \cdot \mathbf{A}] \quad (2.11)$$

where we have used the commutation relation $\mathbf{A} \cdot \mathbf{p} - \mathbf{p} \cdot \mathbf{A} = -i\hbar \nabla \cdot \mathbf{A}$. Since electron core levels are highly localized within a solid ($r \sim 1 \text{ \AA}$) and x-ray photons have wavelengths on the order of 1 nm, the sinusoidal spatial variation of the vector potential can be approximated by its Maclaurin series expansion and truncated to only the first term:

$$\mathbf{A}(\mathbf{r}) = A_0 \hat{\epsilon} e^{i\mathbf{k} \cdot \mathbf{r}} = A_0 \hat{\epsilon} \left(1 + i\mathbf{k} \cdot \mathbf{r} - \frac{1}{2} (\mathbf{k} \cdot \mathbf{r})^2 + \dots \right) \approx A_0 \hat{\epsilon} \quad (2.12)$$

where \mathbf{k} is the photon wave vector and $\hat{\epsilon}$ is the polarization unit vector. Hence, the $\nabla \cdot \mathbf{A}$ term can be neglected and the interaction Hamiltonian can be expressed as

$$H_{\text{int}} = -\frac{e}{mc} \mathbf{A} \cdot \mathbf{p}. \quad (2.13)$$

If we treat the incident photon as a perturbation to the initial bound electronic state, then the transition rate for photoexcitation can be found using Fermi's golden rule: [33]

$$\Gamma \propto \frac{2\pi}{\hbar} \left| \left\langle \psi_f \left| -\frac{e}{mc} \mathbf{A} \cdot \mathbf{p} \right| \psi_i \right\rangle \right|^2 \delta(E_f - E_i - h\nu). \quad (2.14)$$

where ψ_i and ψ_f are the initial and final electronic states respectively and we have neglected many-body relaxation effects in the analyzed material. Again neglecting the spatial dependence of the vector potential, we may rewrite the transition rate as

$$\Gamma \propto \frac{2\pi}{\hbar} \left| -\frac{e}{mc} \mathbf{A} \cdot \langle \psi_f | \mathbf{p} | \psi_i \rangle \right|^2 \delta(E_f - E_i - h\nu). \quad (2.15)$$

Using the relationship

$$\langle \psi_f | \mathbf{r} | \psi_i \rangle = \frac{i\hbar}{(E_f - E_i)m} \langle \psi_f | \mathbf{p} | \psi_i \rangle = \frac{i\hbar}{(h\nu)m} \langle \psi_f | \mathbf{p} | \psi_i \rangle \quad (2.16)$$

we can express the transition rate in terms of the position operator \mathbf{r} :

$$\Gamma \propto \frac{2\pi}{\hbar} \left| -\frac{2i\pi\nu}{c} \mathbf{A} \cdot \langle \psi_f | e\mathbf{r} | \psi_i \rangle \right|^2 \delta(E_f - E_i - h\nu) \quad (2.17)$$

Equations 2.15 and 2.17 are known as the dipole momentum and dipole length approximations of the photoionization cross section respectively. [32]

Ignoring many-body relaxation effects, ψ_i is a core level wavefunction and ψ_f is a plane wave in the continuum. Hence, although in principle the transition matrix restricts the types of transitions allowed in XPS, there will always be a continuum wave function with the proper symmetry. [34] This leads to an important property of XPS: the intensity of a core level photoelectron signal depends only upon its parent element and energy level; it is not modified by the band structure or chemistry of a material. This property allows XPS to be used quantitatively to measure the amount of a particular element or chemical state [32, 34].

The photoionization cross sections for elements up to $Z = 101$ and photon energies up to 1500 keV were first calculated by James Scofield in 1973 [35] and are often known as

Scofield factors. Typically the Scofield factor of the C 1s orbital is set to unity and all other elements are normalized to it. From Equation 2.17, it is clear that the Scofield factor of an electronic state is strongly related to its radial wavefunction. In particular, core levels whose nodal radii are close in value to their wavelengths upon photoionization have relatively high cross sections. [34] Electrons ejected with kinetic energies of 200-1500 eV have wavelengths on the order of 30-90 pm, which matches the radial extent of tightly bound core level states. [36] Conversely, valence electrons whose radii are typically greater than 100 pm, tend to have much lower cross sections in XPS. [32, 34]

2.4.3 Peak Shapes and Satellites

Several factors contribute to the broadening of XPS features, arising from both instrumental properties and material properties. The energy distribution of a monochromated Al K α source can typically be approximated by a Gaussian function with full width half maximum (FWHM) of about 0.3 eV. [32, 37] The electron analyzer, in this case a hemispherical analyzer, typically has a resolution of 0.1 eV when operated at low (10-20 eV) electron pass energies, adding a small amount of additional Gaussian broadening. In this work, the total instrumental resolution was about 0.5 eV for core level XPS spectra as measured by the FWHM of the Au 4f_{7/2} peak of a clean gold sample.

Further broadening arises from the finite lifetime of the XPS process. After emitting a photoelectron, an atom can relax via the emission of an x-ray photon or an Auger electron. This relaxation process has a lifetime $\tau \sim 1 \times 10^{-14}$ s which introduces a Lorentzian contribution to the spectral broadening due to the Heisenberg uncertainty principle ($\Delta E \Delta t \geq \hbar/2$). [33] The intensity I of the resulting distribution is given by

$$I = I_0 \frac{\Gamma^2}{(E - E_0)^2 + \Gamma^2} \quad (2.18)$$

where E_0 is the center of the peak and $\Gamma = \hbar/\tau \sim 0.1$ eV is the half-width at half maximum. [38] Additional Gaussian broadening can be caused by inhomogeneities in the surface chemistry and particle size effects. [39] The resulting convolution of Gaussian and Lorentzian curves is known as a Voigt profile. In this work, most 1s core levels were fit with Voigt

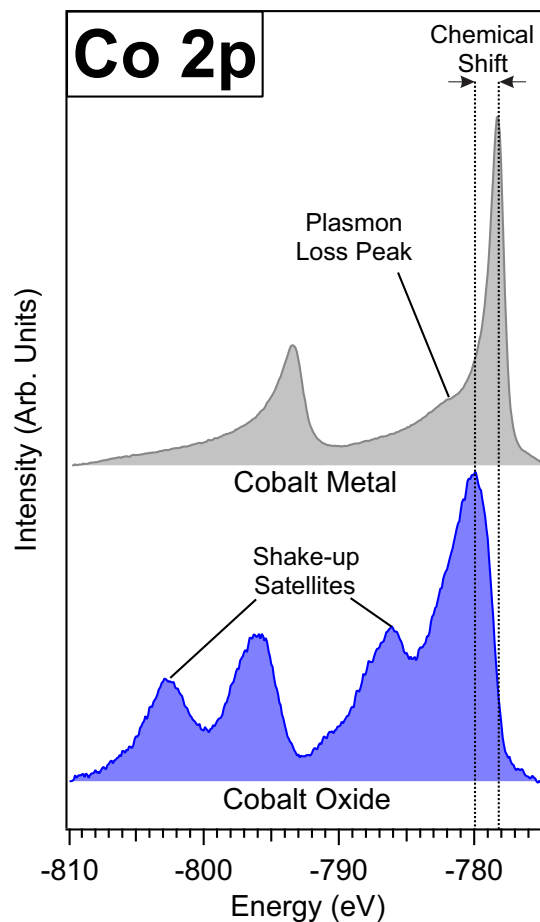


Figure 2.5: Co 2p XPS spectra for cobalt metal and cobalt oxide. The metallic spectrum exhibits a Doniach Sunjic lineshape due to low energy electron-hole excitations by the photoelectron. The CoO spectrum exhibits shake-up satellites as well as a chemical shift due to the ionic bond between the cobalt and oxygen.

profile curves composed of 80% Gaussian and 20% Lorentzian components.

Additional complications in the spectral shape arise in metals due to the excitation of electron-hole pairs by photoelectrons. Since metals typically have a high density of states at the Fermi level, the excitation of an electron from an occupied state to an unoccupied state requires very little energy compared to the kinetic energy of the photoelectron. As a result, photoelectrons excited from metallic samples can lose continuous amounts of energy to these electron-hole excitations. The resulting lineshapes in metallic core level spectra are known as Doniach Sunjic curves, which are characterized by a tail on the low kinetic energy (high binding energy) side of the core level peaks. [40] This is illustrated in the Co

2p spectrum of cobalt metal shown in Figure 2.5.

A similar energy loss process can occur in oxides and semiconductors, although electron excitations in these cases are limited by the band structure of the material. A photoelectron induced excitation from the valence band to the conduction band of the material is known as a shake-up event, while excitation into the continuum is known as a shake-off event. These excitations give rise to corresponding shake-up and shake-off satellite peaks on the high binding energy side of core level peaks. [41] Since shake-up peaks are highly dependent upon the electronic structure of the sample, they are often useful for identifying chemical compounds, as is the case for both FeF_2 and CoO . Figure 2.5 shows Co 2p spectrum obtained from CoO , which exhibits shake-up satellite peaks.

2.4.4 Core Level Intensities

The preceding discussion accounted for the intrinsic physical properties of photoionization, i.e. the absorption of a photon and subsequent emission of an electron from an atom or ion. However, many extrinsic properties must be considered in order to properly correlate measured XPS intensities to the composition of a sample. This section discusses some of the important parameters affecting photoelectron intensities.

The measured intensity of a photoelectron peak depends on a number of factors, including the number of photons impinging upon each atom, the number of atoms present, the probability that an impinging photon results in the emission of a photoelectron (Scofield factor), the probability that each photoelectrons is able to reach the detector, and the efficiency of the detector in measuring electrons of a particular energy. [29] This can be expressed by the following equation:

$$I_A = J \times \sigma_A(h\nu) \times T(E_A) \int_{z=0}^{\infty} \rho_A(z) \exp\left(-\frac{z}{\lambda(E_A, z) \cos \theta}\right) dz \quad (2.19)$$

where J is the photon flux, σ_A is the Scofield factor, $T(E_A)$ is the transmission function and efficiency of the electron detector, $\lambda(E_A, z)$ is the material- and energy-dependent electron attenuation length, $\rho_A(z)$ is the density of atomic of material A at depth z , and θ is the emission angle of the photoelectron measured with respect to the surface normal. Typically,

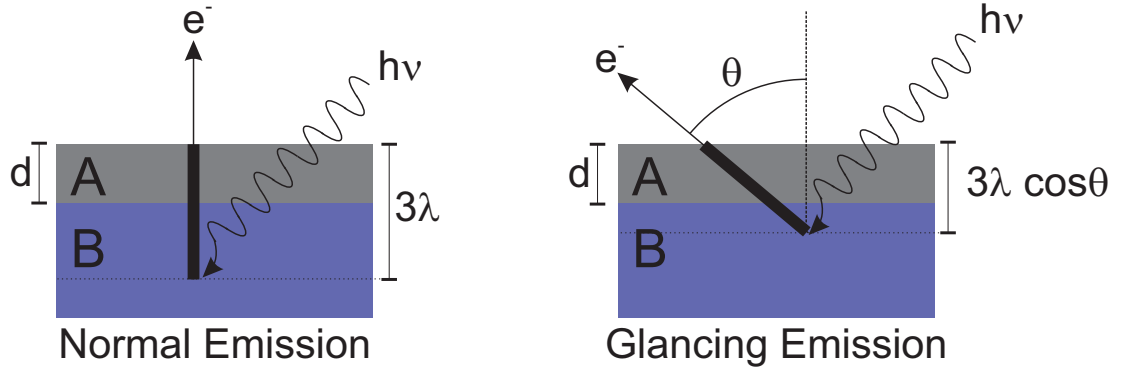


Figure 2.6: Angular dependence of the XPS signal

the x-ray intensity is assumed to be constant over the duration of an experiment and the instrumental factors are calibrated for each electron energy and the experimental geometry.

The exponential dependence on the depth of the photoemitting atom arises from the Beer-Lambert equation and is an important aspect of XPS. [29] The inelastic mean free path for 1000 eV photoelectrons is about 1-2 nm in most materials, so 95% of the XPS signal emanates from a depth of less than 3λ or about 3-6 nm. XPS is thus a surface sensitive experimental technique.

2.4.5 Angle Resolved X-Ray Photoemission Spectroscopy

Angle-resolved x-ray photoemission spectroscopy (ARXPS) utilizes the surface sensitivity of XPS to obtain depth-resolved chemical information from samples. If we consider the layered sample shown in Figure 2.6, we can calculate the intensities of layers *A* and *B* by integrating Equation 2.19 over the relevant depths: [29]

$$I_A = I_A^0 \int_0^d e^{-z/\lambda_{AA} \cos \theta} dz \quad (2.20)$$

$$= I_A^\infty \left[1 - e^{-d/\lambda_{AA} \cos \theta} \right] \quad (2.21)$$

where I_A^0 is the intensity of a thin layer of material *A* with thickness dz , I_A^∞ is the intensity of an infinitely thick slab of material *A*, and λ_{AA} is the attenuation length of electrons from

A passing through material A . Similarly,

$$I_B = I_B^0 \int_d^\infty e^{-z/\lambda_{BA} \cos \theta} dz \quad (2.22)$$

$$= I_B^\infty \left[e^{-d/\lambda_{BA} \cos \theta} \right]. \quad (2.23)$$

The ratio R of these signals is then

$$R = \frac{I_A}{I_B} = \frac{I_A^\infty}{I_B^\infty} \frac{1 - e^{-d/\lambda_{AA} \cos \theta}}{e^{-d/\lambda_{BA} \cos \theta}}. \quad (2.24)$$

It should be emphasized here that the angular dependence of R is not due to the attenuation of x-ray photons with depth. Indeed, Al $K\alpha$ x-rays have attenuation lengths on the order of $1 \mu\text{m}$ in most materials, so the difference between the x-ray flux at the surface and at a depth of 10nm is less than 2%. [39]

In the following work, peak ratios were calculated using Equation 2.24. However, it is often useful to make the approximation that $\lambda_{AA} \approx \lambda_{BA} = \lambda$ and simplify the expression for R :

$$R \approx R^\infty \left(e^{d/\lambda \cos \theta} - 1 \right) \quad (2.25)$$

where $R^\infty \equiv I_A^\infty/I_B^\infty$. Rearranging the terms and taking the natural logarithm results in the following expression:

$$\ln \left(1 + \frac{R}{R^\infty} \right) = \frac{d}{\lambda} \sec \theta. \quad (2.26)$$

Thus, for a uniform layer of material A on a substrate of material B , a plot of $\ln(1 + R/R^\infty)$ vs. $\sec \theta$ should be a straight line whose slope is proportional to the overlayer thickness and whose extrapolated intercept is the origin. This graphical interpretation will be utilized in subsequent chapters as an intuitive way of interpreting ARXPS data. In this work, the error in Equation 2.25 can be estimated as

$$\sigma_R = R^\infty e^{-d/\lambda_{AA} \cos \theta + d/\lambda_{BA} \cos \theta} \quad (2.27)$$

$$\approx \frac{R^\infty}{\cos \theta} \left(\frac{d}{\lambda_{AA}} - \frac{d}{\lambda_{BA}} \right) \quad (2.28)$$

$$\leq 2R^\infty \quad (2.29)$$

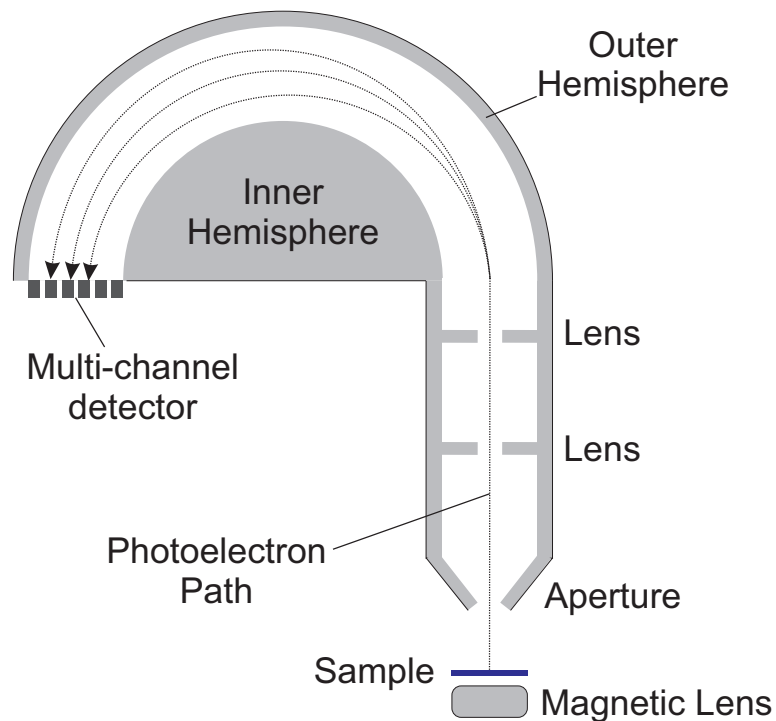


Figure 2.7: Schematic of a hemispherical analyzer

where $\cos \theta \leq 1$, the values of λ_{AA} and λ_{BA} can differ by a factor of two, and d is up to three times larger than these attenuation lengths.

2.4.6 Instrumentation

All XPS spectra in this work were acquired using a Thermo ESCALAB 250Xi equipped with a monochromated Al $K\alpha$ x-ray source, which produced 1486.6 eV photons. The x-ray source was positioned at an angle of 54° from the vertical axis. X-rays were produced by bombarding an Al anode with 10-15 keV electrons. These x-rays were monochromated by reflecting the beam off a toroidal quartz (10 $\bar{1}$ 0) crystal. Photons were diffracted according to the Bragg equation, $n\lambda = 2d\sin\theta$, and those whose energy was 1486.6 ± 0.1 eV were reflected onto the sample surface.

The electron detector, a concentric hemispherical analyzer (CHA) was oriented vertically so that the angle between the x-ray source and analyzer was fixed for all XPS measurements, regardless of the tilt angle of the sample. A schematic of a CHA is shown in Figure 2.7.

A CHA consists of a pair of concentric hemispheres which are biased such that the inner hemisphere is more positively charged than the outer hemisphere during XPS measurements. Photoelectrons from the sample can pass through the analyzer to a detector if their kinetic energy satisfies the equation:

$$\text{KE} = e\Delta V \left(\frac{R_1 R_2}{R_2^2 - R_1^2} \right) \quad (2.30)$$

where ΔV is the potential applied between the hemispheres and R_1 and R_2 are the radii of the inner and outer hemispheres respectively. [29] The energy resolution of a CHA is proportional to the kinetic energy of the electrons as they travel between the hemispheres. Consequently, a retarding lens is typically used to decelerate the photoelectrons before they enter the CHA. The energy of photoelectrons after this deceleration is known as the pass energy of the detector. [29] Core level spectra in this work were acquired in constant analyzer energy mode, so that the pass energy of all electrons was fixed at 20 eV. This ensures that the energy resolution and detector efficiency were constant for all measured core levels. Survey spectra were acquired at 100 eV pass energy in order to increase the total count rate at the expense of energy resolution.

2.5 Ultraviolet and Inverse Photoemission Spectroscopy

Ultraviolet photoemission spectroscopy (UPS) is schematically the same technique as XPS, but the energy of the photons used is typically less than 150 eV. [42] In this work, photons were generated using a He-II discharge lamp with a primary energy of 40.8 eV, and electrons were detected using a CHA at a pass energy of 2 eV. At these low photon energies, the photoemission signal from occupied states near the Fermi energy of a material is greatly enhanced. [39, 42] Additionally, the energy resolution of UPS is typically much better than that of XPS (~ 0.1 eV), making it a very effective tool for characterizing narrow valence band features. Since photoexcitation conserves electron momentum, k -resolved photoemission can be used to map the band structure of a material. [32, 42] In this work, UPS was performed in angle-integrated mode with the electron detector in line with the surface normal in order to measure the total density of states (DOS) of the valence band.

The distinct lineshapes of the CoO and FeF₂ valence bands were then used as fingerprints for these materials.

Although UPS and XPS are similar, it is often illuminating to differentiate between the two by rewriting Equation 2.3 as

$$\text{KE} = h\nu - (E_N - E_{N-1}) - \phi \quad (2.31)$$

where E_N is the initial energy of the system and E_{N-1} is the energy of the ($N-1$)-electron system after photoionization. This expression emphasizes the fact the photoemission does not measure the true ground state of a material, but rather an excited state in which valence band features may depend upon interactions between bound electrons and the generated hole. This will be an important consideration in the discussion of FeF₂ in subsequent chapters.

Inverse photoemission spectroscopy (IPS) is a complementary technique to UPS, wherein a highly collimated mono-energetic electron beam is directed at the sample. These incident electrons can couple to high lying unoccupied states and decay into the conduction band via the emission of a photon. [32] Similar to photoemission, the photon energy can be related to the binding energy of the unoccupied electron state by the following equation:

$$h\nu = \text{KE} + (E_N - E_{N+1}) - \phi \quad (2.32)$$

which has been written to emphasize the fact that the final state in IPS is not the ground state of the material, nor is it the same as the final state in UPS or XPS. Rather, the sample is measured in an excited ($N+1$)-electron state so caution must be exercised when interpreting IPS spectra. Similar to UPS, momentum conservation in IPS allows for k -resolved measurements, known as KRIPES. [32]

In this work, all IPS spectra were acquired in an angle integrated mode in order to map the total DOS of the conduction band. Electrons were produced using a Stoffel-Johnson type electron gun using a BaO cathode. [43] During operation, the cathode temperature was approximately 2300°C, introducing a thermal energy spread of about 0.2 eV to the electron beam. The incident electron energy could be varied from 4-50 eV in order to access

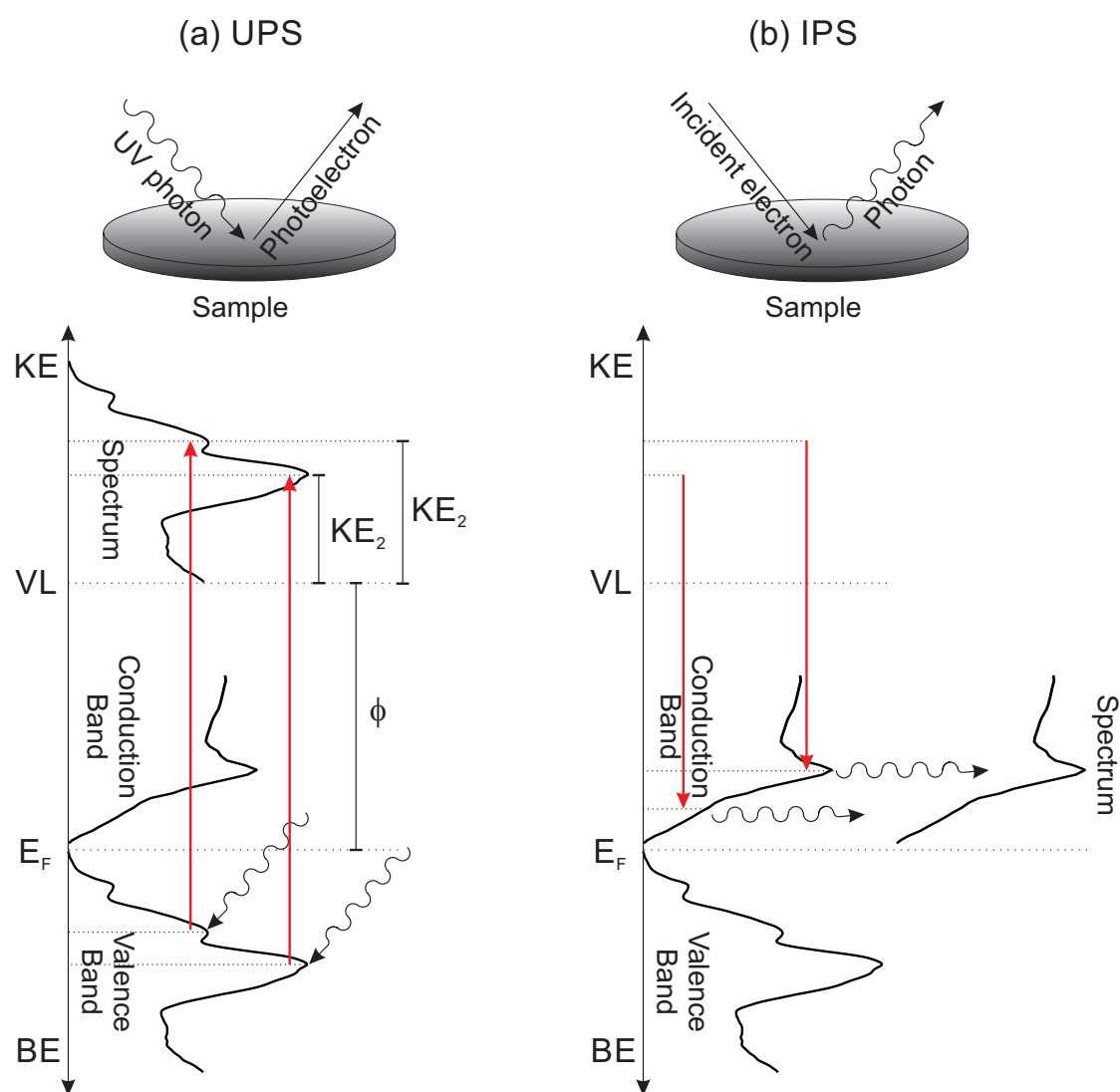


Figure 2.8: Schematic diagram of (a) ultraviolet photoemission spectroscopy and (b) inverse photoemission spectroscopy.

different unoccupied energy states. The electron beam diameter was approximately 1 mm at the sample surface. A fraction of the emitted photons reflected off a concave spherical diffraction grating with parallel grooves at a spacing of $d = 1200 \text{ nm}^{-1}$. This diffraction grating reflected photons onto a two-dimensional position sensitive detector. The dispersion of photons from the grating with respect to their wavelength λ is given by:

$$\frac{dE}{dl} = \frac{hc \cos \beta}{\lambda^2 m R d} \left(\frac{10^4 \text{ \AA}}{\text{mm}} \right) \quad (2.33)$$

where m is an integer, β is the angle of the reflected photons with respect to the surface normal of the grating, and R is the distance between the detector and the grating (given in meters). [44] Hence, after calibrating the detector by measuring the position of the Fermi energy of a clean gold sample, the energy of a photon could be determined by its position on the detector. The total resolution of the IPS system was limited to about 0.3 eV due to the thermal spread of the incident electrons (0.2 eV) and the resolution of the detector (0.2-0.3 eV). This resolution was measured by fitting the derivative of the Fermi level of a gold sample with a Gaussian curve.

Since the energy window of the IPS spectrometer used in this study is about 7 eV, some IPS spectra were constructed as a composite of different incident electron energies. were used in order to probe a wide range of electronic states high above the Fermi level. An electron energy of 20.3 eV was used to measure states near the Fermi level, whereas electron energies as high as 34.3 eV were used to access high lying unoccupied states 30 eV above the Fermi energy. Figure 2.9 shows one such composite spectrum from a polycrystalline FeF₂ thin film. The different colored areas correspond to different incident electron energies, and the resulting spectrum (shown in black) uses a smoothed average of the component spectra. The intensity spikes at the high energy end of each spectrum are experimental artifacts caused by the low count rate at the edge of the spectrometer.

The combined use of UPS and IPS in the same vacuum chamber enables the characterization of both the occupied and unoccupied states of a sample near the Fermi level. Plotting both sets of spectra with respect to the Fermi Energy (which is set to zero) allows for a simple measurement of the material band gap, which is given by the energy gap between

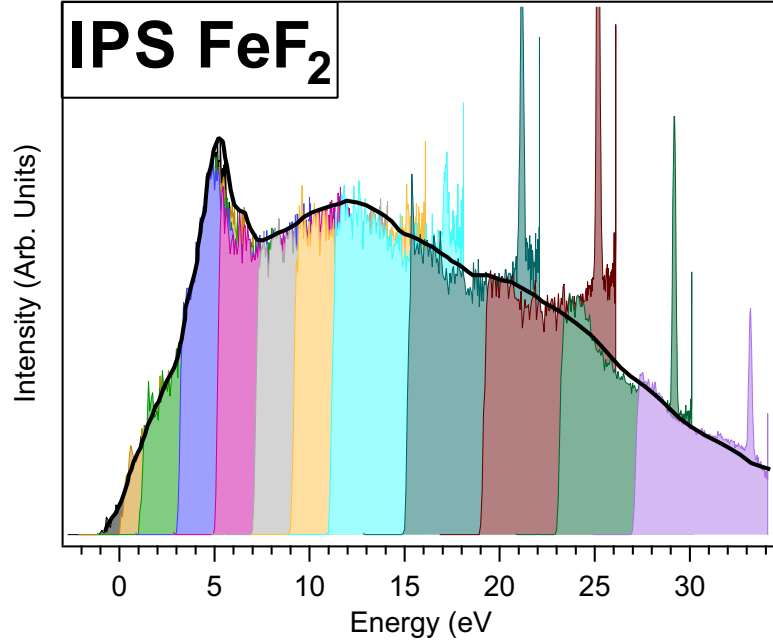


Figure 2.9: Composite inverse photoemission spectrum of a polycrystalline FeF_2 thin film using incident electron energies of 20.3 – 34.3 eV.

the onsets of the valence band maximum and the conduction band minimum. [45] Since the combined final states of UPS and IPS consist of a hole in the valence band and an electron in the conduction band, this measured band gap is closely related to the transport gap of the material.

2.6 Scanning Tunneling Microscopy

Scanning tunneling microscopy (STM) is a surface sensitive microscopy technique that can probe the atomic scale topography of a flat conductive sample. In this work, STM was used to image the surface of epitaxially grown CoO thin films. In STM, an atomically sharp tungsten tip is brought to within 0.1-1 Å of a sample surface through the use of piezoelectric transducer, which is a ceramic device that expands and contracts by microscopic amounts in response to an applied voltage. A bias applied between the tip and the sample can cause quantum mechanical tunneling of electrons from the tip to the sample or vice versa. [42] This tunneling current is proportional to the wave function overlap between the two

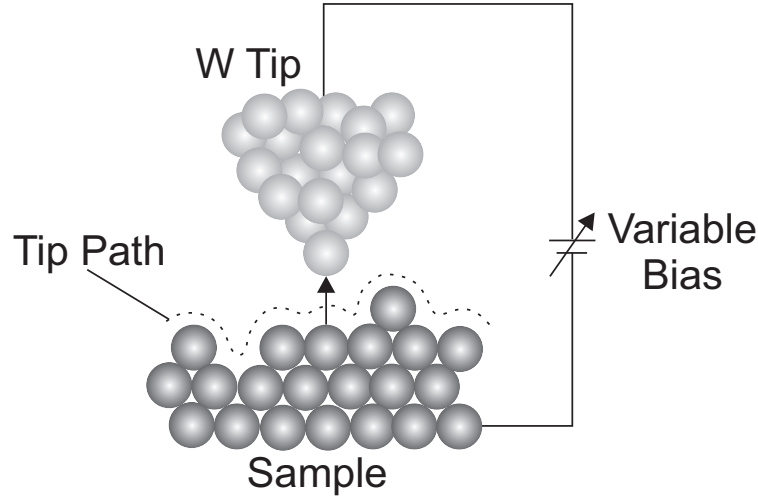


Figure 2.10: Schematic diagram of a scanning tunneling microscope

materials and can be expressed as:

$$I \propto \exp \left(-2d \frac{\sqrt{2m\phi}}{h} \right) \quad (2.34)$$

where d is the distance from the tip to the sample, m is the electron mass, and ϕ is the work function of the materials. [42] The tip is then rastered across the surface of the sample using two more mutually perpendicular piezoelectric transducers. The exponential dependence of the tip on the distance d makes the tunneling current very sensitive to changes in the surface topography. The current is also highly sensitive to the density of electronic states at the surface, so STM can also be used to probe local chemical or elemental differences in sample surfaces. This property will be vital to the STM measurements on CoO presented in subsequent chapters.

The STM was operated at room temperature in constant current mode, in which a feedback mechanism keeps the tip at a constant tunneling current by continuously adjusting the height as the tip moves along the sample surface. Typical scan parameters were a voltage of ± 2.5 V and a tunneling current of 1-2 nA.

The lateral resolution of the STM, typically on the order of 1 Å, is highly dependent upon the sharpness and cleanliness of the STM tip. Ideally, the tunneling current from the

tip should originate from a single atom at the apex of the tip, as shown in Figure 2.10. However, contaminants on the surface of the tip or diffusion of tungsten atoms can cause the current to originate from multiple points, thus leading to a loss of resolution or the appearance of artifacts in the resulting image. In order to rectify this issue, the tip can be cleaned by prolonged tunneling to/from a clean metal surface at high voltage and high current (± 10 V and 50 nA).

To minimize the effects of external vibrations while imaging, the STM stage is mounted on a series of springs which mechanically isolate it from the walls of the UHV chamber. Periodic noise from electrical and mechanical sources can also be removed from the STM images by performing a fast Fourier transform (FFT) of the STM image and removing these artificially induced peaks from the resulting FFT image.

2.7 Transmission Electron Microscopy

The polycrystalline FeF_2 and CoO films studied in this work were too rough to image using STM. Instead, samples were prepared on SiO_xN_y membranes (SiMPore Inc), and transmission electron microscopy (TEM) was used to characterize the structural and phase evolution of these films upon exposure to lithium. In TEM, a beam of high energy electrons is transmitted through a thin film, and the intensity and/or energy of the electrons that pass through the film are measured. Several different TEM modes are illustrated in Figure 2.11. TEM measurements were performed using a JEOL 2010F Field Emission STEM operated at 197 kV and equipped with a Gatan GIF 200 spectrometer. The lateral resolution of the microscope was approximately 0.2 nm, which is two orders of magnitude larger than the wavelength of the incident electrons (0.025 Å). This resolution limit can be attributed to aberrations in the electromagnetic lenses used in the scope. [46]

2.7.1 Annular Dark-Field Imaging

Annular dark-field scanning TEM (ADF-STEM) was used to image the FeF_2 and CoO films. In this imaging mode the electron beam was rastered across the sample, and scattered electrons were detected by an annular detector placed beyond the sample, as shown in Figure

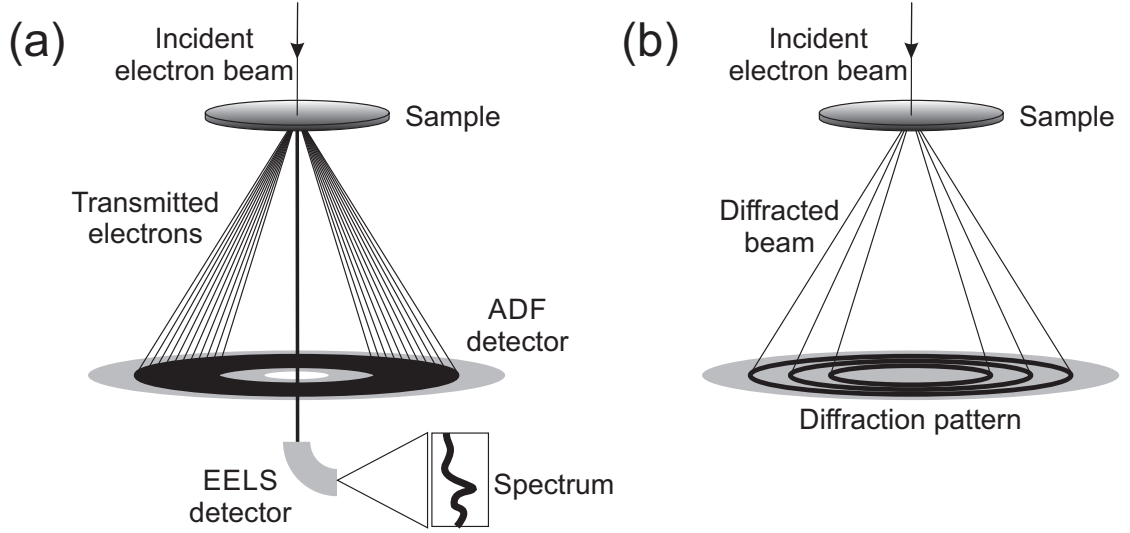


Figure 2.11: Schematic diagram of (a) ADF-STEM and EELS and (b) SAED in a transmission electron microscope.

2.11(a). Since electron scattering is more probable for collisions with high- Z elements, bright regions (those with high scattering intensities) could be attributed to Fe or Co, while dark regions were attributed to Li, O, F, or Si. [46]

2.7.2 Electron Diffraction

Selected area electron diffraction (SAED) was used to probe the local crystalline structure of the samples. In SAED, incident electrons are diffracted by the periodic lattice of the sample, and the resulting pattern is projected onto a two-dimensional detector, as shown in Figure 2.11(b). The diffraction of electrons is governed by the lattice spacing d of the target material and the wavelength of the incident beam, as described by Bragg's law: [46]

$$2d \sin \theta = n\lambda \quad (2.35)$$

where n is an integer. For randomly-oriented samples, the diffraction pattern is a series of rings, whose radii correspond to the dimensions of the lattice in k -space. In this work, SAED was used to identify the crystalline structure of the initial films and the conversion reaction products.

2.7.3 Electron Energy Loss Spectroscopy

Electron energy loss spectra (EELS) can be used in conjunction with ADF-STEM imaging to obtain a two-dimensional elemental map of a sample, as illustrated in Figure 2.11(a). In EELS, the energy of inelastically scattered electrons is measured, and the amount of energy loss can be attributed to phonon/plasmon excitations, band transitions, and inner shell ionizations. The inner shell ionization loss is characteristic of the element from which the incident electron scattered, while band transition losses provide chemical information about the target material. [46] This allows EELS to be used for elemental and chemical identification with precise spatial resolution. The EELS spectra in this work were obtained with a collection half angle of 27 mrad and convergence angle of 10 mrad and with an energy resolution of 1.1 eV. EELS spectrum images (32×32 pixels) obtained with a 0.3 nm probe size and a 1.25 nm spatial resolution were collected to obtain information on the spatial distribution of Co or Fe species in the reacted films.

2.8 Low Energy Electron Diffraction

Low energy electron diffraction (LEED) is schematically a similar process to SAED, which was discussed in the previous section, except that LEED utilizes electron reflection rather than transmission. In LEED measurements, a well collimated beam of monoenergetic electrons is directed at a crystalline sample surface. The electron energy can be varied over the range of 20-300 eV, with a current of approximately $1 \mu\text{A}$ and a beam diameter of about 1 mm. The energy spread of the beam is determined by the temperature of the thermionic source and is usually $\sim 0.5 \text{ eV}$. Owing to the macroscopic spot size of the electron beam, LEED measurements provide area-averaged information about sample surfaces, and hence LEED is useful for obtaining structural information from highly ordered single crystals or epitaxial films.

For a well-ordered surface, incident electrons are coherently backscattered from the surface according to Bragg's law, forming a diffraction rods which can be intercepted by a phosphorescent screen in order to produce a LEED spot pattern. A series of five concentric hemispherical grids are placed in front of the sample such that the sample surface lies at

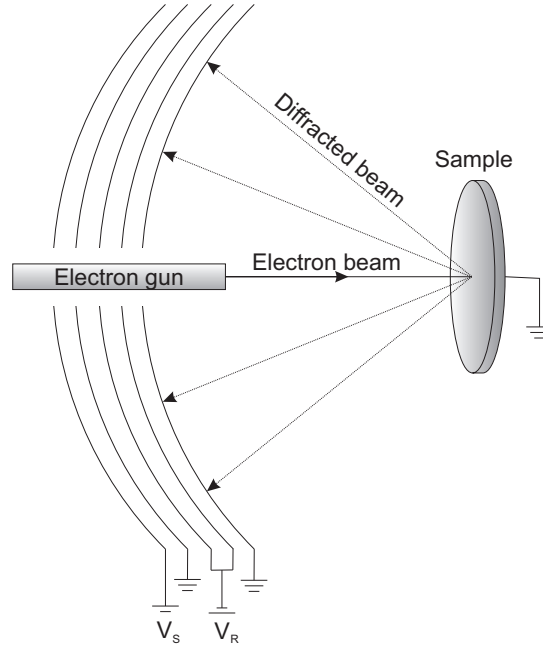


Figure 2.12: Schematic diagram of low energy electron diffraction.

the focal point of the hemispheres, as shown in Figure 2.12. The grid closest to the sample is held at ground potential in order to avoid altering the trajectories of scattered electrons. The next two grids are held at a potential V_R close to the energy of the electron beam in order to retard all electrons except those that were elastically scattered. A fourth grid is placed beyond the retarding grid and is held at ground potential. The final grid is coated in a phosphorescent or fluorescent material and is held at a potential of $V_S = 3\text{-}5\text{ kV}$. Electrons that pass through the first four grids are accelerated into this final grid and produce a visible pattern which can be viewed through a window. [32] Due to the low energy of the incident electron beam, the inelastic mean free path of these electrons is on the order of 1 nm, making LEED a highly surface sensitive technique. [32] Consequently, LEED is useful for determining the long-range order of a sample surface. In this work, LEED was used to determine whether a single crystal substrate was sufficiently well-ordered for epitaxial film growth and also to determine the surface structure of the subsequently grown metal oxide films.

2.9 Summary

Iron fluoride and cobalt oxide films have been prepared in a variety of surface orientations in order to probe the reactivity of different crystalline faces with lithium. The initial films were characterized using x-ray photoemission spectroscopy (XPS) to determine their purity, stoichiometry, and chemical composition. Ultraviolet and inverse photoemission spectroscopy (UPS and IPS) were used to determine the electronic structure near the Fermi level, particularly the band gap of both materials. Scanning tunneling microscopy (STM) of CoO surfaces before and after small lithium exposures was used to determine the initial reaction sites. Lastly, angle-resolved x-ray photoemission spectroscopy (ARXPS) was used to characterize the progression of the Li-FeF₂ and Li-CoO reactions as they progressed from the surface into the bulk of the films. The structures of the films were characterized using scanning tunneling microscopy (STM) and transmission electron microscopy (TEM).

Chapter 3

Polycrystalline Iron Fluoride Films

3.1 Introduction

To isolate the fundamental properties of FeF_2 during conversion, it was first necessary to synthesize high-purity samples which were compatible with UHV environments and electron-based spectroscopic techniques. Ultra-thin films grown in UHV by exposure of Fe metal to XeF_2 precursors were found to produce extremely pure FeF_2 films (less than 1% O and C contamination) that were sufficiently conductive for photoelectron spectroscopy. This eliminated the need for carbon black, which is typically added to FeF_2 to enhance its conductivity in Li-ion batteries. [14] The use of thin films was also compatible with transmission electron microscopy (TEM) measurements, which require the transmission of electrons through a sample in order to acquire an image. Lithiation was performed in UHV chamber by exposing the FeF_2 film to a beam of Li atoms emitted from a getter source, thus eliminating the need for electrolytes and solvents. Since the discharge of a cathode, represented by reading Equation 1.4 from left to right, is exothermic, this reaction proceeded without the need to apply a potential between the cathode and anode. Changes upon lithiation to the electronic structure and chemical phase of the FeF_2 film were then characterized using XPS, UPS, and IPS, while the structural and morphological changes were characterized with TEM.

3.2 Sample preparation

For the photoemission studies, FeF_2 samples were grown on 99.99% pure polycrystalline Fe foil substrates (Alfa Aesar). The Fe substrate was first degreased using acetone and ethanol before being loaded into the vacuum chamber to remove any macroscopic contamination. The foils were then cleaned in UHV by sputtering with 1.5 kV Ar^+ ions for several hours,

which resulted in a surface with less than 0.1% C and O contamination as measured by XPS. These clean Fe surfaces were then exposed to about 10^5 Langmuirs (L, $1 \text{ L} = 10^{-6} \text{ Torr}\cdot\text{sec}$) of XeF_2 gas in order to fluorinate the surface of the Fe foil.

The XeF_2 -induced growth of FeF_2 is believed to follow a self-limited Mott-Cabrera mechanism. First the weakly bound XeF_2 molecule approaches the Fe surface and dissociates into $\text{Xe} + 2\text{F}^-$ by picking up two electrons from the metallic surface. The F^- ions, attracted by their positive image potential induced in the substrate, diffuse into the Fe where they react to form FeF_2 . [47] When the insulating fluoride layer reaches a critical thickness, in this case about 5.5 nm, electrons can no longer diffuse through the FeF_2 to initiate the dissociation of the XeF_2 molecule, and the growth of the FeF_2 layer ceases. [48, 49]

For TEM measurements, about 5 nm of Fe metal was deposited via electron-beam physical vapor deposition onto a well-degassed SiO_xN_y TEM membranes (20 nm thickness, SiMPore Inc). The Fe thin film was then fluorinated using XeF_2 . The initial metallic layer was sufficiently thin so that all Fe was reacted with XeF_2 , and hence no Fe^0 was visible in subsequent XPS measurements. Furthermore, no evidence of membrane etching or fluorination was observed during exposure to XeF_2 .

After fluorination, both sets of FeF_2 films were briefly exposed to atmosphere during transfer to their respective analysis chambers. A small amount of iron oxidation ($< 1\%$) was induced by this step, as measured by XPS. Most of the hydroxyl and organic species adsorbed during this transfer were removed by annealing the samples for 10 minutes in UHV at 285°C . This annealing temperature was chosen to be as high as possible without reducing the FeF_2 film.

Lithiation was performed in a UHV chamber by passing 6.5-7.0 A through a well degassed Li getter source (SAES Getters) containing a lithium zeolite. This heated the zeolite to about 800°C , causing the emission of high purity metallic Li. The lithium dose was controlled by the amount of time the source was heated. Typical lithiations were 5-10 min at 6.5 A, which deposited lithium at a rate of approximately 0.07 nm/min. After an initial several-hour outgassing procedure for the getter source upon installation, the chamber pressure could be kept to less than 1×10^{-9} Torr during Li deposition.

3.3 Results

3.3.1 FeF₂ Thin Film Characterization

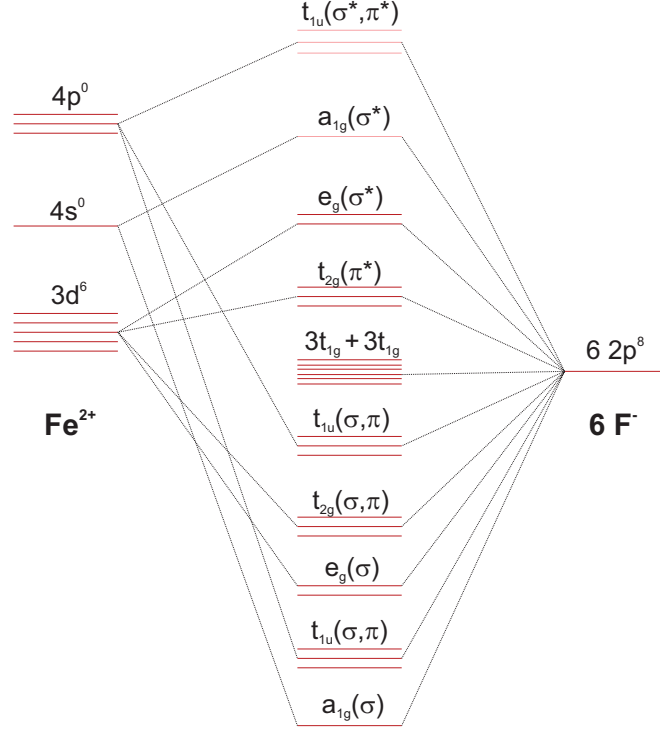


Figure 3.1: Ligand field splitting of Fe core levels in an octahedral FeF₆ arrangement.

Iron (II) fluoride has rutile-type tetragonal ($P4_2/mnm$) crystalline structure composed of edge-sharing FeF₆ octahedra with lattice parameters $a = b = 4.697 \text{ \AA}$ and $c = 3.309 \text{ \AA}$. [50, 51] Since F is a weak-field ligand, this octahedral geometry causes the energetically degenerate 3d⁶ electronic states of Fe²⁺ to split into a high-spin t_{2g}(4)e_g(2) configuration. The ligand field splitting of FeF₂ is shown schematically in Figure 3.1. FeF₂ is antiferromagnetic and has a Néel temperature of 78.3 K in the bulk. [51] Since the measurements presented here were all performed at room temperature ($\sim 298 \text{ K}$), no long-range magnetic ordering is expected in the FeF₂ crystallites.

Despite the insulating nature of FeF₂, [52] no sign of sample charging (i.e. peak broadening or binding energy shifts) was observed during photoemission or inverse photoemission. This confirms that the FeF₂ films were thin enough for the escaping negative charge to be replenished via the electrically grounded metal substrate. Figure 3.2 shows the valence

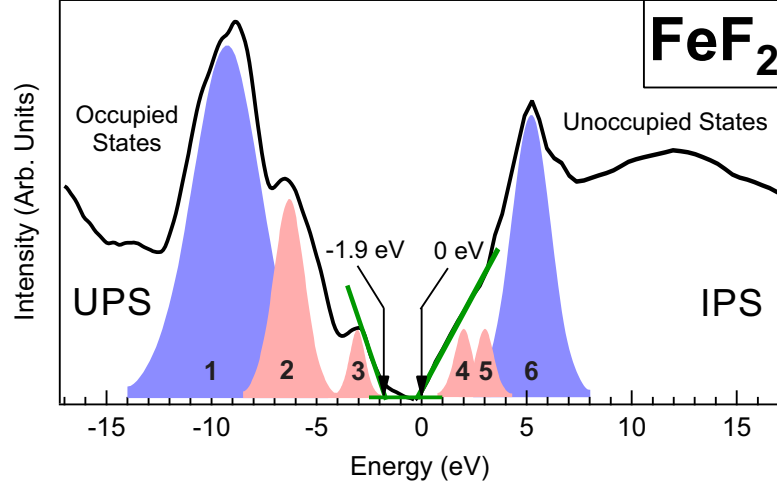


Figure 3.2: UPS and IPS spectra of a polycrystalline FeF₂ thin film. Peak positions and intensities were determined by a crystal field model as explained in the text. The band gap was determined to be 1.9 eV.

band and conduction band spectra of the degassed FeF₂ film obtained from UPS (left) and IPS (right) measurements respectively. Both spectra are referenced to the Fermi energy ($E_F = 0$). The IPS spectrum is a composite of several different incident electron energies ranging from 20.3 eV to 48.3 eV. This was done in order to measure a wide range of conduction band states using a grating spectrometer with a limited energy range. For UPS, valence band electrons were excited using 40.8 eV photons from a He II discharge lamp. The peaks labeled in each spectrum are related to the final state crystal field multiplets, which are discussed in more detail below.

In UPS measurements, an electron is removed from the n -electron valence band of FeF₂, resulting in $3d^{n-1}$ multiplet states. Figure 3.3 lists the possible electron configurations of FeF₂ resulting from photoemission. The relative energies of these states can be determined through a d^5 Tanabe-Sugano diagram, as shown in Figure 3.4 [53–56] and their relative intensities are determined by their degeneracy. Kambara estimated the crystal field splitting of FeF₂ to be $\Delta_0 \approx 0.8$ eV and the Racah parameter to be $B \approx 0.1$ eV [57]. Using these values, we find that the 6A_1 state, which consists of five unpaired electrons, is the lowest energy configuration. The small UPS peak at -3 eV (peak 3 in Figure 3.2) can then be attributed to this state. The 4T_1 , 4T_2 and ${}^4E(G)$ states, which lie at about $E/B = 30$ or 3 eV above the 6A_1 state, are almost energetically degenerate. Their total statistical weight is five times

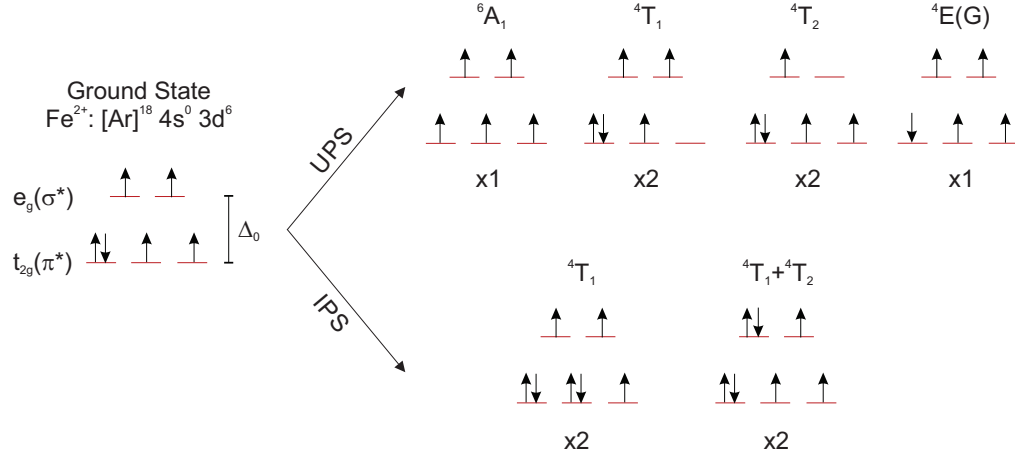


Figure 3.3: The electronic structure of FeF₂ near the Fermi level and final states multiplets resulting from UPS and IPS.

greater than that of the ⁶A₁ state. Hence, peak 2 in Figure 3.2 is attributed to these states. Peak 1 is attributed to non-bonding F 2p states, which are present in photoemission and x-ray emission spectra of FeF₂ and several other metal fluorides. [58, 59]

In IPS, an electron is added to the conduction band of FeF₂, resulting in a 3dⁿ⁺¹ electron configuration, whose energetics can be estimated from a d⁷ Tanabe-Sugano diagram, as shown in Figure 3.5. [53–56] The resulting ⁴T₁ and ⁴T₁ + ⁴T₂ states are separated by about 0.6 eV and give rise to the broad rising edge of the conduction band spectrum from 0-4 eV (peaks 4 and 5). The sharp peak at 5 eV can be attributed to unoccupied nonbonding F 2p states. This last peak assignment is supported by the similarities between x-ray absorption and electron energy loss spectra of FeF₂ and various other metal fluorides. [59–62]

The band gap of FeF₂ can be estimated by a linear extrapolation of the band edges down to the background intensity as shown in Figure 3.2, resulting in a measured band gap of 1.9 eV. As discussed in the previous chapter, the final state of UPS is a hole in the valence band, while the final state of IPS consists of an extra electron in the conduction band. Consequently, this measured band gap is closely related to the electron transport gap, which is the energy gap necessary to create an unbound electron-hole pair. The value measured here is consistent with the ~1.5 eV edge found in optical absorption measurements. [63] Note that the optical gap should be lower than the electron transport gap due to the energy required to separate the electron-hole pair.

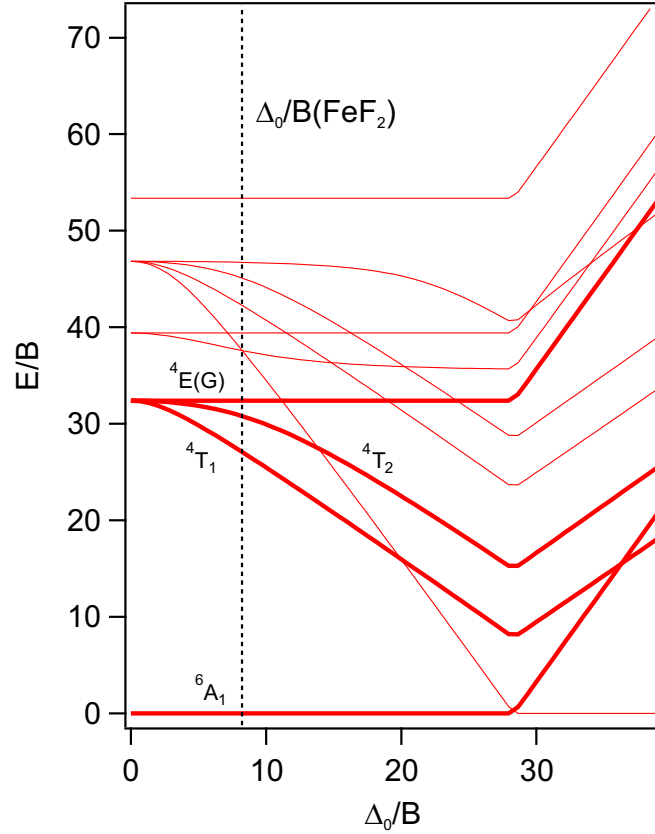


Figure 3.4: A d^5 Tanabe-Sugano diagram for an octahedral complex. Relevant electron configuration symmetries are bolded.

XPS was used to determine the stoichiometry of the FeF_2 films. The Fe 2p and F 1s core levels measured on a similarly prepared FeF_2 thin film are shown in Figure 3.6. The F 1s peak consists of a single component at -685.1 eV. The Fe 2p lineshape is characteristic of FeF_2 and is composed of two broad doublet peaks, whose centroids are separated by about 14 eV. Each component of the doublet has an associated satellite feature at ~ 6 eV higher binding energy. [64, 65] The formation of a doublet is caused by the spin-orbit coupling of the Fe 2p electrons with the Fe nucleus. This interaction splits the $\ell = 1$, $s = \frac{1}{2}$ state into $j = \frac{3}{2}$ and $j = \frac{1}{2}$ states, denoted as the $2p_{3/2}$ and $2p_{1/2}$ electronic states respectively. The relative intensity of each component is determined by its degeneracy (given by $2j + 1$), so the ratio of the $2p_{3/2}$ and $2p_{1/2}$ peak areas is 2:1.

A peak fitting scheme for the Fe $2p_{3/2}$ core level based on the work of Grosvernor and coworkers is shown in Figure 3.7. [66] This peak fit is not intended to be definitive, but

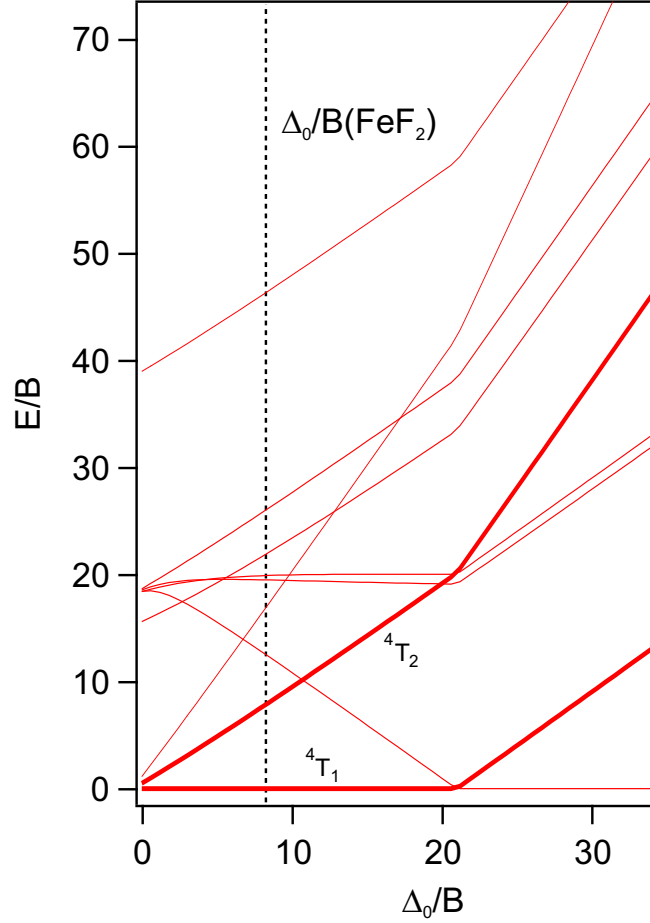


Figure 3.5: A d^7 Tanabe-Sugano diagram for an octahedral complex. Relevant electron configuration symmetries are bolded.

it is presented in order to illustrate the complexity of the Fe 2p lineshape for FeF₂. The large intrinsic widths of the 2p doublets is mainly caused by multiplet coupling of unpaired Fe 2p core electrons and unpaired electrons in the valence band. The relative intensities and energy separation of the resulting Fe²⁺ multiplets were calculated by Gupta and Sen. [67, 68] These multiplets are shown in red in Figure 3.7. The blue peak at -714.1 eV is attributed to Fe ions near the surface of the film, for which the crystal field strength is lower than that of bulk Fe ions and the symmetry of the crystalline structure is altered. In principle, this envelope should exhibit the same multiplet splitting as the bulk Fe²⁺ states. Since the F 1s core level is very close in binding energy to the Fe 2p, its surface and bulk plasmon loss peaks (shown in green) overlap with the 2p_{3/2} intensity. The positions and

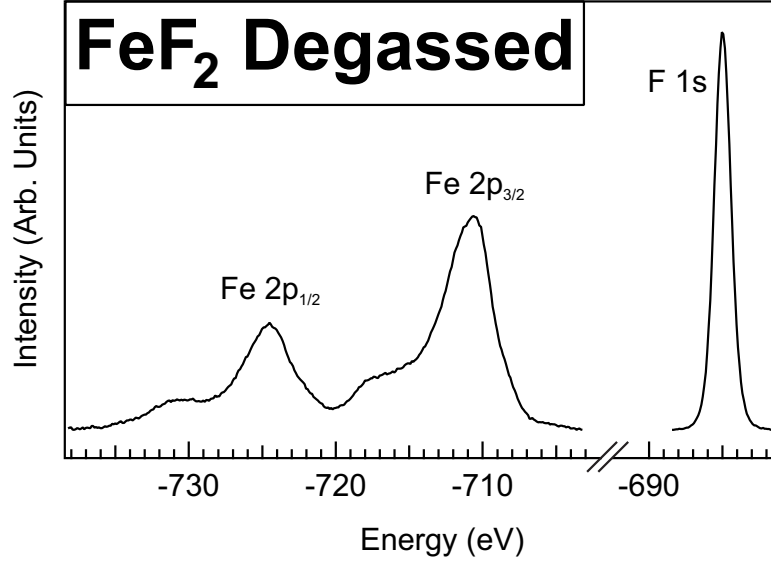


Figure 3.6: XPS spectra of the Fe 2p and F 1s core levels of polycrystalline FeF₂

intensities of these features were estimated by the plasmon loss peaks of CaF₂, which are well isolated from other core level peaks. [66] However, plasmon loss peaks should decrease in intensity as $I_n \propto \alpha^n/n!$,¹ so part of the intensity attributed to the high binding energy loss features may be due to other sources. Lastly, the satellite feature at -718.1 eV is attributed to the shake-up process, whereby an ejected 2p photoelectron loses a portion of its energy by exciting a 3d electron into an unoccupied 4s level. [70] This loss of kinetic energy is interpreted in XPS as a gain in binding energy. No metallic iron from the substrate is visible in the Fe 2p spectrum (BE=-707 eV), suggesting that the films were at least 5 nm thick and were homogeneous.

Figure 3.8 shows a series of TEM measurements that were performed on the FeF₂ film grown on SiO_xN_y in order to characterize its morphology and crystalline structure. Figure 3.8(a) shows an ADF-STEM image of the FeF₂ film, which appears as bright (high-*Z*) features on a dark (low-*Z*) background. Under this assumption, the FeF₂ in this image appears as a collection of interconnected particles with an average lateral size of 9.1 nm. This size is very close to the initial particle size of FeF₂ used in conversion cathodes, which

¹This is due to the fact that plasmon losses by a photoelectron are independent events and hence are governed by Poisson statistics: $P(n) = \frac{1}{n!} \left(\frac{t}{L}\right)^n e^{-t/L}$ where e is Euler's number, t is the film thickness, and L is the average distance between scattering events. [69]

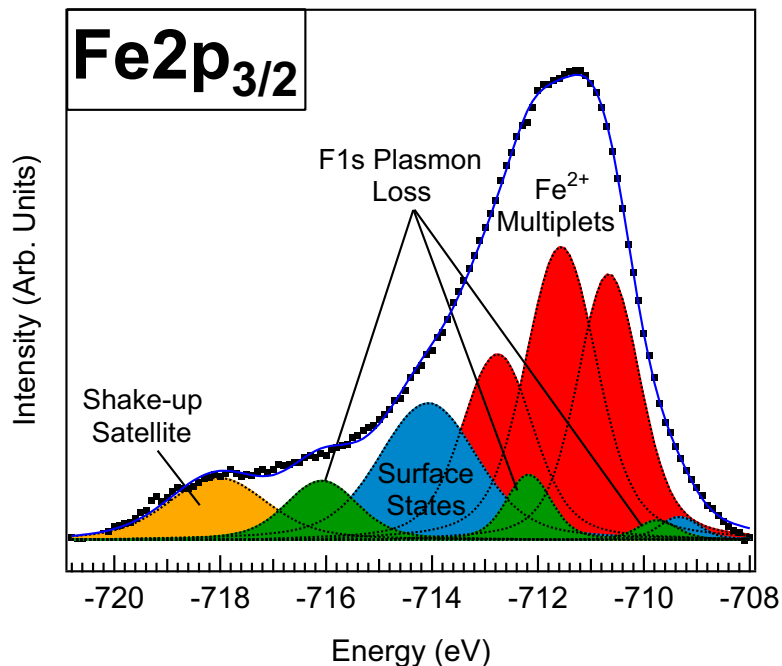


Figure 3.7: Peak fit of the Fe $2p_{3/2}$ core level of polycrystalline FeF_2 , which exhibits multiplet splitting, F 1s plasmon loss peaks, and shake up satellites. [66]

suggesting that this film should be an appropriate analogue for a true FeF_2 cathode. [11, 12]

The elemental interpretation of the ADF-STEM image is supported by the small scale STEM image in Figure 3.8(c) and its corresponding STEM-EELS elemental maps in Figures 3.8(d) and (e) obtained from the intensities of the Fe M edge and Si L edges at each pixel in the image. The apparent inhomogeneity in the thickness of the FeF_2 film in these images is attributed to either poor wetting of the initial Fe metal film on the TEM grid or to reorganization of the film upon exposure to XeF_2 . The SAED pattern in Figure 3.8(b) is characteristic of rutile $P4_2/mnm$ FeF_2 , and the Fe $L_{2,3}$ EELS near-edge structures (not shown) obtained from the film are indicative of pure FeF_2 . [71]

3.3.2 Lithiation of FeF_2 thin films

The following section discusses the electronic and structural evolution of the FeF_2 thin films upon exposure to atomic lithium. XPS, UPS, and IPS measurements were all performed in the same UHV chambers as their respective lithiations, while TEM samples were briefly exposed to atmosphere during transfer to the microscope.

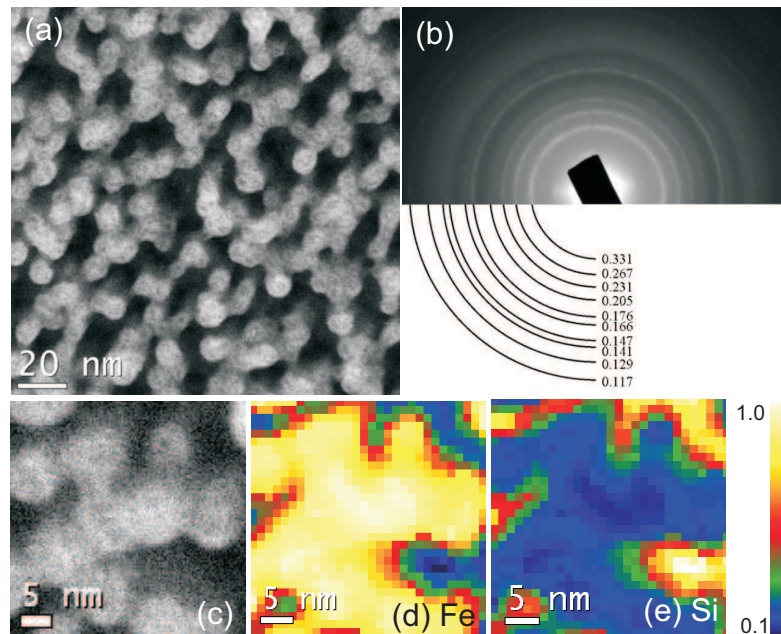


Figure 3.8: (a) ADF-STEM image of the initial FeF_2 thin film on a TEM grid. The dark area is the SiO_xN_y membrane substrate. (b) SAED pattern indicating a rutile structure ($P4_2/mnm$). (c) Small scale STEM image and the corresponding elemental maps from the FeF_2 thin film for (d) Fe and (e) Si relative intensities.

Figure 3.9 shows the Fe 2p and F 1s core levels of the FeF_2 film after each of a series of Li exposures. After the first lithium exposure (~ 0.5 nm Li), a new feature appears in the Fe 2p_{3/2} region at a binding energy that is 4.5 eV lower than the centroid of the FeF_2 2p_{3/2} peak. A corresponding peak also appears in the Fe 2p_{1/2} region. These peaks are attributed to the Fe 2p doublet of metallic Fe^0 . This suggests that the deposited lithium induced the conversion of FeF_2 to Fe^0 . The intensity of these features increases monotonically with increasing Li exposure while the peaks associated with FeF_2 decrease. This is consistent with a direct conversion from Fe^{2+} to Fe^0 . After the eighth lithium exposure (~ 5 nm Li), the Fe 2p spectrum resembles that of pure metallic Fe, which is shown at the top of Figure 3.9, suggesting that the film was completely reacted. During the series of Li exposures, the FWHM of the F 1s peak increased slightly from 1.6 eV to 1.8 eV and the peak centroid shifted from 685.1 eV to 686.9 eV, which is consistent with the formation of LiF. [72] However, the abrupt shift in binding energy upon the final lithium exposures, can also possibly be attributed to preferential charging of the LiF-rich regions of the sample during the XPS measurements.

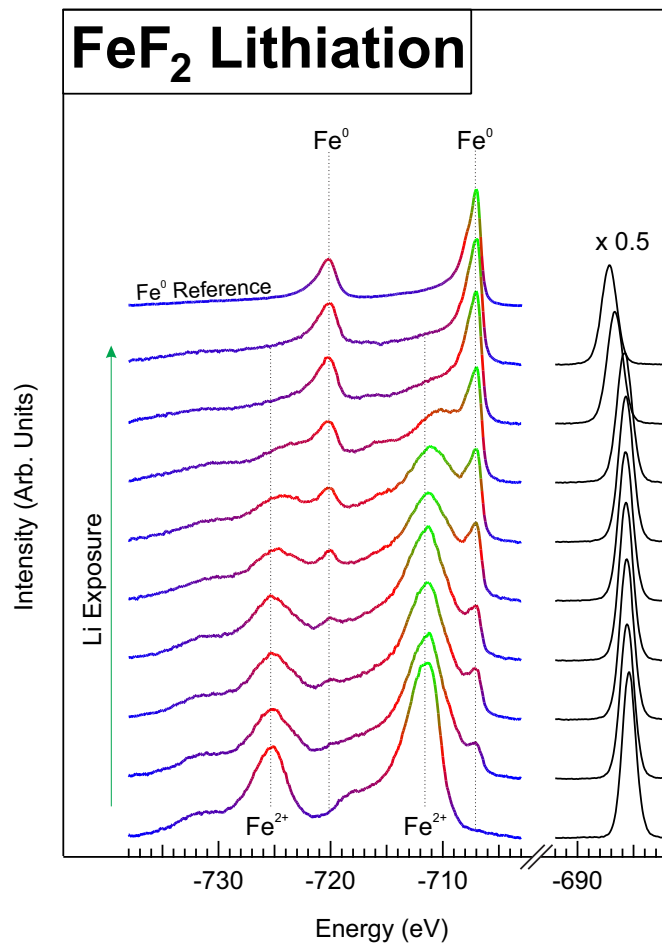


Figure 3.9: Evolution of the Fe 2p and F 1s core levels of FeF₂ upon Li exposure. The topmost spectrum was taken from an Fe metal reference sample.

Owing to the low cross section of the Li 1s core level in XPS and its overlap with the Fe 3p core level, nuclear reaction analysis (NRA) was used to quantify the amount of Li and F in the fully reacted sample. This measurement was performed in a separate vacuum chamber, necessitating another exposure to atmosphere. However, LiF is stable in air, and hence should not have been affected by this brief exposure. In NRA, a 2 MeV proton beam was used to induce the ${}^7\text{Li}(\text{p},\alpha)\alpha$ and ${}^{19}\text{F}(\text{p},\alpha){}^{16}\text{O}$ reactions and detect Li and F respectively. Using these measurements, the fluorine coverage was estimated to be $(20 \pm 5) \times 10^{15}$ atoms/cm², while the Li coverage was estimated at $(23 \pm 3) \times 10^{15}$ atoms/cm². The relatively high errors in these measurements were due to the extremely low count rate of NRA. Nevertheless, the similarity in the amounts of Li and F suggest that full conversion of

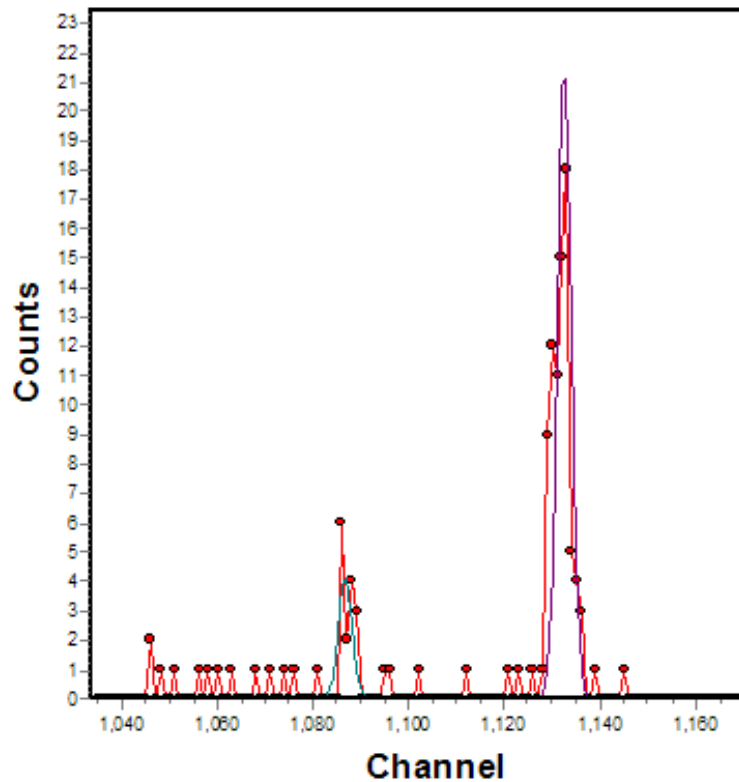


Figure 3.10: Nuclear reaction analysis spectrum of a fully lithiated FeF_2 film showing $^7\text{Li}(p,\alpha)\alpha$ and $^9\text{F}(p,\alpha)^{16}\text{O}$ peaks.

the film had occurred, and the final products were Fe^0 and LiF , as expected from Equation 1.4.

UPS and IPS spectra of the FeF_2 surface after each of a series of Li exposures are shown in Figure 3.11. Similar to the spectra in Figure 3.2, the spectra are referenced to the Fermi energy. In this figure, the spectra were offset from one another in order to see features close to the Fermi energy in both the valence and conduction bands. The bottom two spectra are replicated from the pristine spectra in Figure 3.2 and exhibit the initial 1.9 eV band gap of FeF_2 . Upon exposure to Li, a Fermi edge, which is characteristic of metallic samples, appears in both UPS and IPS. This suggests the formation of metallic Fe^0 , which is in agreement with the XPS results. Simultaneously, the F 2p states in the valence band shift to a slightly lower binding energy and splits into two electronic states whose final energies are -9 eV and -11 eV. These peaks, denoted by filled circles in Figure 3.11, are characteristic of the F 2p electronic states of LiF . [73, 74] The hybridized F 2p states at 5 eV in the

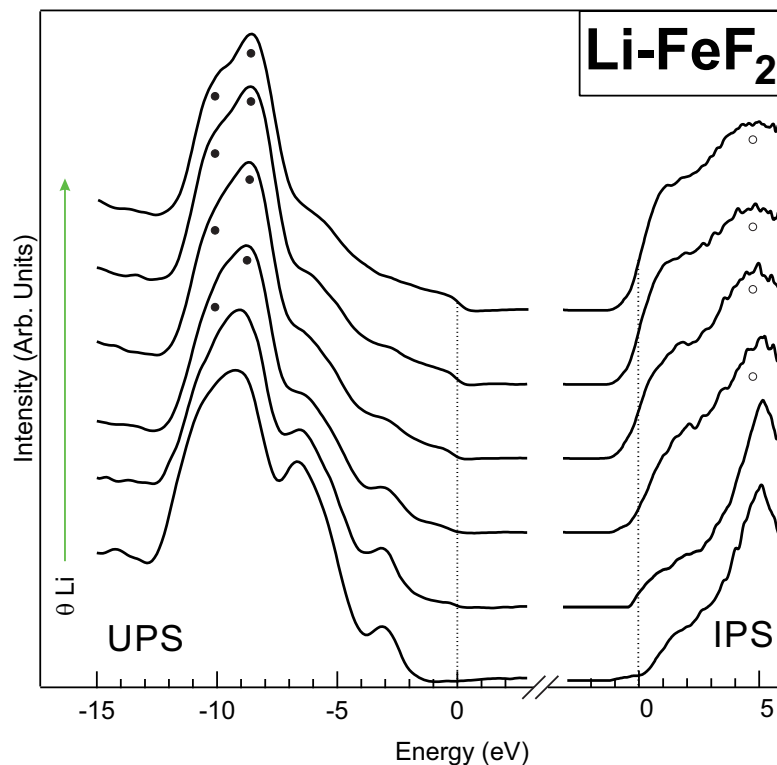


Figure 3.11: UPS and IPS spectra of a lithiated polycrystalline FeF_2 thin film. The band gap has been artificially broadened in order to more easily identify features close to the Fermi level (0 eV).

conduction band, shown as open circles, broaden with increasing Li exposure but do not shift greatly in IPS. The energy gap between the occupied LiF states in the valence band and the unoccupied LiF states in the conduction band is about 14 eV, which is consistent with the 13.6 eV band gap of LiF. [75]

From the preceding spectroscopic results, it is clear that atomic Li is able to reduce FeF_2 in a manner than is consistent with previous electrochemical studies. [10–13] Of particular note is the fact that very little unreacted FeF_2 remains in the film after the last Li exposure, suggesting that Li is mobile enough in the polycrystalline $\text{FeF}_2/\text{Fe}/\text{LiF}$ nanocomposite to reach all regions of the film.

In order to characterize the morphology of the reacted FeF_2 , a fully lithiated film was measured using TEM. The images obtained from this film are shown in Figure 3.12. After lithiation, the film appears in ADF-STEM as a collection of interconnected particles whose average lateral size is now 3.3 nm, as compared to 9.1 nm for the pristine FeF_2 film. This

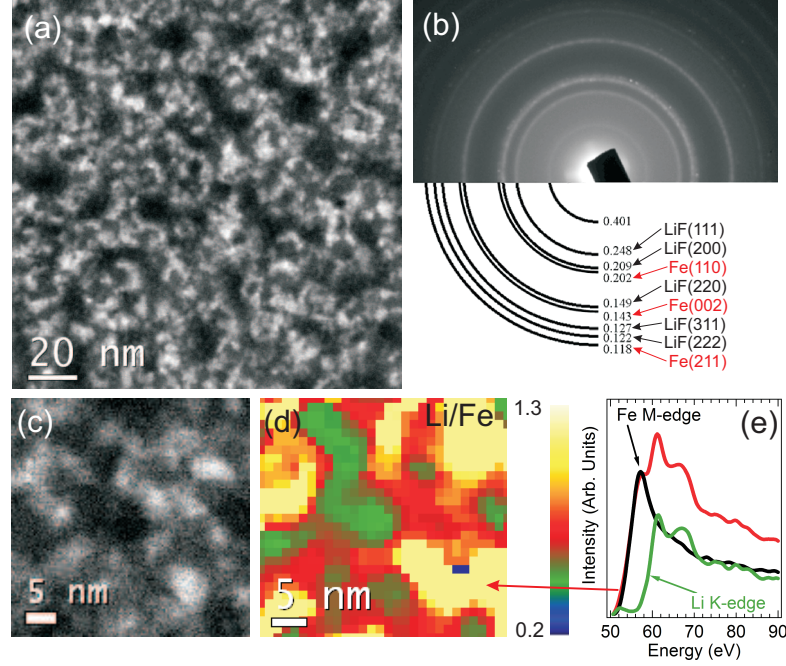


Figure 3.12: (a) ADF-STEM image of a lithiated FeF_2 thin film on a TEM grid. The dark area is attributed to the SiO_xN_y TEM membrane; (b) SAED pattern indicating complex structure due mainly to the overlap of a cubic ($\text{Im}\bar{3}\text{m}$) Fe^0 and a cubic ($\text{Fm}\bar{3}\text{m}$) LiF pattern; (c) Small scale STEM image and the corresponding elemental map (d) of the Li-K:Fe-M intensity ratio from the lithiated FeF_2 thin film. (e) EELS spectrum extracted from a Li-rich region can be decomposed into a Fe-M edge and a Li-K edge.

is shown in Figure 3.12(a). Similar to the image shown in Figure 3.8(a), bright features should correspond to regions with high- Z elements, i.e. Fe. The small scale STEM image and STEM-EELS elemental map shown in Figure 3.12(c) and (d) respectively, show the variation of the Li:Fe ratio as determined by a peak fit of the overlapping Fe-M and Li-K edges of EELS spectra taken at each pixel. An example of this peak fit for a lithium rich region is shown in Figure 3.12(e). The Fe and Li peak shapes in these EELS spectra indicate the presence of both metallic and oxidized Fe as well as LiF. [76] Oxidation of the Fe is believed to have occurred during transfer to the microscope when the sample was briefly exposed to air. The EELS results are confirmed by the SAED pattern shown in Figure 3.12(b), which can be fit with a linear combination of bcc Fe (space group, $\text{Im}\bar{3}\text{m}$, $a = 0.2859 \text{ nm}$) and cubic rock salt LiF (space group, $\text{Fm}\bar{3}\text{m}$, $a = 0.402 \text{ nm}$). No Li_2O , LiSi_x , or LiN_x phases, which would indicate the reduction of the SiO_xN_y membrane, were visible in the SAED pattern. However, the presence of the cubic rocksalt FeO (space group

$Fm\bar{3}m$, $a = 0.469$ nm) is likely, and its diffraction pattern probably overlaps with that of LiF. A weak feature observed at $d = 0.401$ nm could not be identified.

These combined photoemission and TEM results confirm the similarity between the reaction of atomic Li in UHV on a clean FeF_2 film, and its electrochemical counterpart where Li^+ ions react with FeF_2 in a conversion battery. The reduction in the Fe particle size upon lithiation is attributed to the high mobility of Li relative to that of Fe. During conversion, Fe is reduced and precipitates locally without diffusing, resulting in an interconnected array of metallic nanoparticles. This is an important aspect of FeF_2 conversion batteries, since this metallic array is believed to facilitate ionic and electronic transport during both the charging and discharging phases of Li-ion battery operation.

3.4 Conclusion

Polycrystalline FeF_2 thin films were prepared by exposing polycrystalline Fe to XeF_2 gas in a UHV chamber. These films were determined to be about 5 nm in thickness with an average lateral particle size of about 10 nm. Their electronic structure was characterized by XPS, UPS, and IPS, while their morphology and crystalline structure were characterized by TEM. The films were determined to be very high purity, exhibiting small amounts of surface oxidation resulting from their exposure to atmosphere. The electronic structure of the FeF_2 was described by a simple approach which considered the ligand field splitting of the Fe $3d^6$ electrons due to the octahedral bonding geometry of the FeF_2 crystal.

The preparation conditions of the FeF_2 films were chosen such that the resulting films closely resembled the FeF_2 nanocomposites used in lithium ion conversion batteries. This similarity enabled a direct comparison to be made between the solid state reaction and the electrochemical reactions characterized in previous studies. Upon exposure to atomic lithium, a spontaneous solid state conversion reaction occurred, as predicted by Equation 1.4. FeF_2 was transformed into a mixed phase composed of interconnected metallic Fe^0 nanoparticles and LiF. The reaction proceeded until all of the FeF_2 was exhausted, at which point the lithiation was stopped intentionally.

The complete conversion of the film and the accompanying reduction in particle size

of the Fe from 10 nm to 3 nm suggest that Li atoms were much more mobile than iron in the initial FeF_2 film as well as in the mixed nanocomposite. This caused the Fe metal to precipitate locally, which enabled the formation of a conductive network of interconnected metal nanoparticles. An instructive counterexample of this phenomenon is the conversion of CuF_2 . Electrochemical studies of CuF_2 electrodes have shown that Cu^{2+} ions are highly mobile compared to Li, which leads to the growth of large isolated Cu^0 particles during conversion. [16] The lack of a conductive framework within the reacted CuF_2 electrode results in poor electronic conductivity and subsequent difficulties during the reconversion (charging) reaction. The results shown here indicate that the formation of this conductive network is an intrinsic property of FeF_2 and is not (primarily) caused by binders, electrolytes, or other additives.

Despite the differences between the solid state UHV reaction presented here and the electrochemical lithiation performed in previous studies, the results are remarkably similar. [11–13] These results can thus be viewed as a proof of concept, which suggests that UHV measurements of Li-ion battery materials are useful for analyzing fundamental material properties which otherwise might not be apparent in electrochemical studies. The following chapter will build upon these results and focus on the UHV reaction of epitaxial $\text{FeF}_2(110)$ films in an attempt to isolate the reactivity of a single crystalline face of FeF_2 . This will elucidate the mechanism by which lithium diffuses into and reacts with FeF_2 on a sub-nanometer scale.

Chapter 4

Epitaxial Iron Fluoride Films

4.1 Introduction

Having characterized the solid state reaction of iron fluoride nanoparticles, which were morphologically similar to the nanocomposite cathodes used in conversion batteries, we now turn our attention to more idealized systems in order to isolate the properties of different crystalline faces of FeF_2 . This chapter discusses the characterization of the $\text{FeF}_2(110)$ crystalline surface upon exposure to atomic Li.

FeF_2 has two high-symmetry planes along which nanoparticle surfaces could be expected to terminate. These are shown schematically in Figure 4.1. The $\text{FeF}_2(001)$ surface exposes $[001]$ channels whose cross sections can be approximated as $3.32 \times 3.32 \text{ \AA}^2$ squares. The (110) surface has much narrower channels whose dimensions are approximately equal to the Fe-F bond length ($2.10 \times 2.10 \text{ \AA}$). Since these channel dimensions are very close to the diameters of Li atoms and Li^+ ions (2.90 \AA and 1.43 \AA respectively), this difference in surface geometry could be expected to affect greatly the diffusivity of Li into these FeF_2 surfaces. [78, 79]

The role of geometric constraints in the reaction of FeF_2 with lithium ions has been explored via molecular dynamics (MD) simulations by Ma and Garofalini, [77] which predicted a Li^+ diffusion barrier of less than 50 meV along the $[001]$ channel. This value is considerably lower than the 200-300 meV diffusion barrier calculated for layered Li_xCoO_2 , which reacts solely through Li^+ diffusion. [80] Conversely, the $[110]$ channel of FeF_2 has a predicted diffusion barrier of about 1000 meV. The dependence of the diffusivity Γ upon the diffusion barrier E_B can be approximated as:

$$\Gamma = v^* \exp(\Delta E_B/kT) \quad (4.1)$$

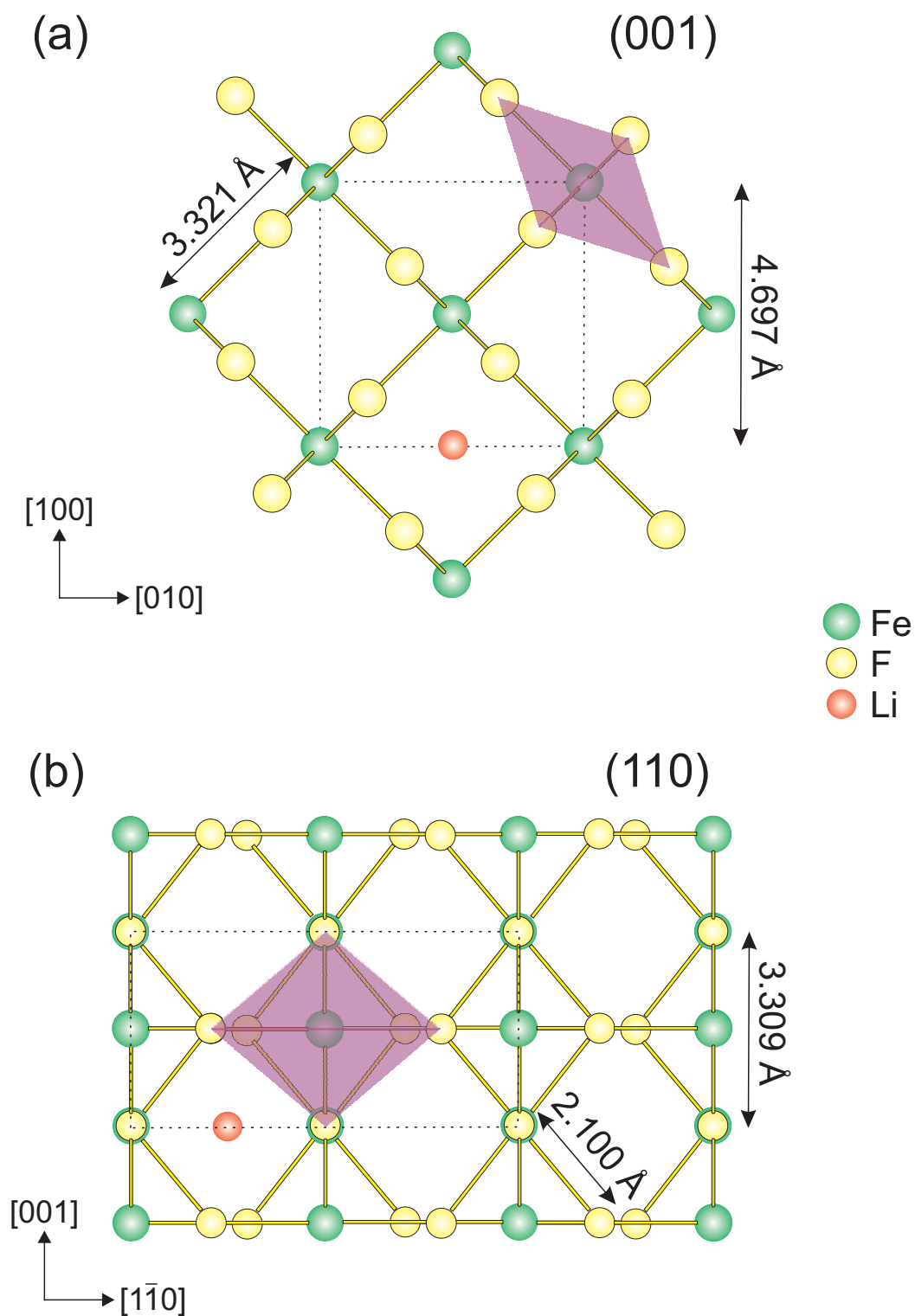


Figure 4.1: Schematic of the (a) $\text{FeF}_2(001)$ and (b) $\text{FeF}_2(110)$ surfaces showing the channels in each surface. Unit cells boundaries are shown as dotted lines. One FeF_6 octahedra surface is shown in purple as an example in each image. Adapted from reference [77].

where v^* is a vibrational frequency on the order of 10^{13} s^{-1} , k is Boltzmann's constant, and T is the temperature. [81] Using this equation, the Li diffusivity along the [001] direction is expected to be 16 orders of magnitude higher than that of the [110] direction.

In the aforementioned MD simulations, the morphology of the Li-FeF₂ reaction was shown to depend heavily on the surface of the FeF₂ crystal that was exposed to lithium. [77, 82] In the conversion reaction of the FeF₂(001) surface, the [001] channels facilitate lithium diffusion into the bulk of the crystal. This leads to an inhomogeneous reaction front progression, where the bulk of the crystal begins to react before the surface reaction has completed. Conversely, the reaction with the FeF₂(110) surface initiates in a layer-by-layer fashion due to the inability of Li to diffuse directly into the lattice. However, as the reaction proceeds several layers into the FeF₂ surface, grain boundaries between Fe nanoparticles and the LiF matrix provide pathways for lithium diffusion into the crystal. In particular, the lithium diffusion barrier along the Fe(111)/LiF(001) interface (300 meV) was found to be significantly lower than that of any other Fe/LiF interface (~ 2000 meV). The FeF₂ beneath these specific interfacial regions then become preferential nucleation points for the sub-surface conversion reaction, causing a non-planar reaction front as the conversion reaction proceeds into the FeF₂(110) crystal. This inhomogeneity in Li diffusivity causes regions of unreacted FeF₂ to remain in the near-surface region of the film.

In order to characterize the Li-FeF₂(110) reaction in a way that complements these MD simulations, high-purity epitaxial FeF₂(110) thin films were grown and exposed to atomic lithium in an ultra-high vacuum chamber. The (110) orientation has the lowest surface energy of the FeF₂ crystalline faces, so this surface is expected to dominate the nanocrystalline FeF₂ composites used in electrochemical cells. [82] The resulting solid state reaction that occurred upon Li exposure was then characterized by ARXPS in order to produce a nanometer-scale model of the reaction progression. The results obtained from these ARXPS measurements indicate that the reaction front initially progresses in a layer-by-layer fashion, forming a planar interface between the reacted overlayer and the unreacted FeF₂ substrate. This is consistent with MD simulations for small lithium exposures. [77] However, when the reacted layer reaches a depth of ~ 1.2 nm into the film, the reaction front deviates from this planar geometry and the reacted overlayer acquired a non-uniform thickness. This behavior

is consistent with a model in which preferential reaction nucleation occurs in the sub-surface regions of the $\text{FeF}_2(110)$ crystal due to selective Li diffusion along Fe/LiF interfaces. The chemical composition of the reaction products and the phase evolution of the FeF_2 film agree with the results of x-ray pair distribution function (PDF) studies, galvanostatic intermittent titration technique (GITT) studies, and prior XPS studies of cycled FeF_2 electrodes, each of which found evidence of the formation of an intermediate compound identified as $\text{Fe}_x\text{Li}_{2-2x}\text{F}_2$. [14, 15]

4.2 Sample Preparation

Epitaxial $\text{FeF}_2(110)$ films were prepared by the Schuller group at the University of California San Diego. [83, 84] These films were grown on $\text{MgF}_2(110)$ single crystal substrates by electron beam evaporation of FeF_2 powder (Cerac Inc.) at a rate of 0.05 nm/s. The temperature of the MgF_2 substrates was maintained at 300°C to enhance the crystallinity of the film. During deposition, the chamber pressure was less than 2×10^{-7} Torr. The FeF_2 structure and crystallinity were investigated using x-ray reflectometry (XRR), x-ray diffraction (XRD), and helium ion microscopy (HIM). The XRR data was acquired using a D8 Discover Bruker rotating anode diffractometer with Cu $K\alpha$ ($\lambda = 1.54 \text{ \AA}$, 8047 eV) radiation. The film was exposed to air during the transfer from the growth chamber to the ultra-high vacuum analysis chamber. In order to remove adsorbates from the surface, the FeF_2 film was degassed at 300°C in UHV for 30 minutes.

Similar to the polycrystalline FeF_2 study, atomic lithium was deposited onto the surface of the FeF_2 film at room temperature using a lithium getter source (SAES Getters). A set of ARXPS measurements was taken after each Li exposure in order to examine changes in the composition, thickness, and homogeneity of the reacted layer.

4.3 Results and Discussion

4.3.1 Characterization of the $\text{FeF}_2(110)$ Film

Figure 4.2 shows x-ray reflectivity (XRR) data from the as-grown $\text{FeF}_2(110)$ thin film. In XRR, a beam of monoenergetic x-rays is directed at the sample surface at a glancing angle,

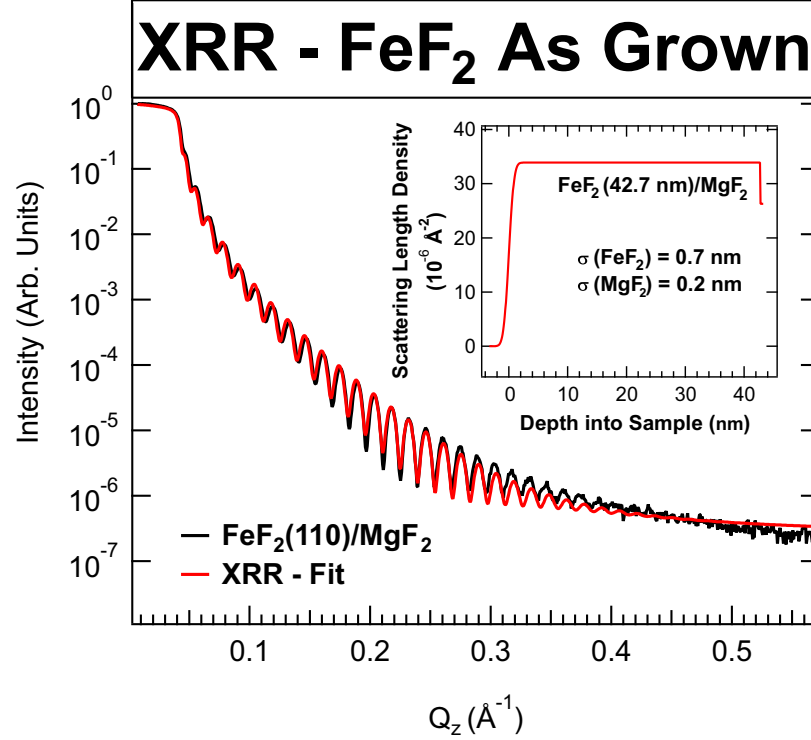


Figure 4.2: X-ray reflectometry data from the as-grown FeF₂(110) film indicating a film thickness of 42.7 nm and a surface roughness of $\sigma = 0.7$ nm.

and the intensity of the reflected beam is measured as a function of the polar angle. Due to the different electron densities of the MgF₂ substrate and the FeF₂ overlayer, x-rays reflect from the interface of the film and the substrate. The interference of x-rays reflected at the surface with those reflected from the interface leads to oscillations in the total reflected intensity known as Kiessig fringes. [85] The period of these oscillations is determined by the overlayer thickness, while their intensity depends on the surface and interface roughness. [85] The fit to the XRR data was performed with MOTOFIT software by assuming a slab model density profile which is shown in the inset. [86] The film thickness was assumed to have a Gaussian distribution with a standard deviation σ . These measurements indicate an FeF₂ film thickness of 42.7 nm, a surface roughness of $\sigma = 0.7$ nm, and an FeF₂/MgF₂ interface roughness of 0.2 nm. Helium ion microscopy images of the film, shown in Figure 4.3, indicated that the lateral dimensions of the FeF₂ domains were 10-15 nm, suggesting a dense pillar-like growth mode.

After transferring the FeF₂(110) film to the XPS chamber and annealing at 300°C to

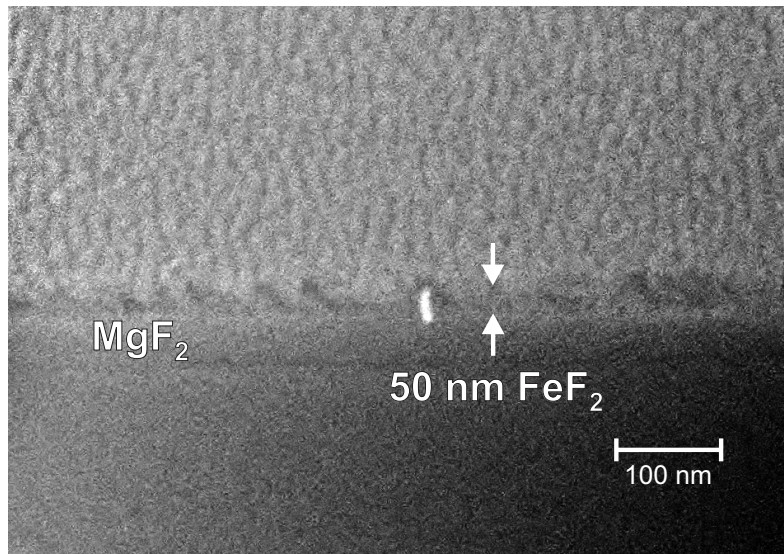


Figure 4.3: Helium ion microscopy image of an $\text{FeF}_2(110)$ film showing lateral domain sizes of 10-15 nm. The image was acquired with an acceleration voltage of 35.0 kV and a current of 0.1 pA.

remove surface contamination, a series of normal emission XPS spectra was taken to assess the purity and stoichiometry of the film. These spectra are shown in Figure 4.4. The Fe 2p core level spectrum (inset (a)) is composed of broad $2p_{3/2}$ and $2p_{1/2}$ states at binding energies of -711 eV and -725 eV and small satellite features whose centroids are at ~ 6 eV higher binding energy than the main doublet peaks. The F 1s core level spectrum (inset (b)) is composed of a single feature at -685 eV. The line shapes and binding energies of these Fe 2p and F 1s features are consistent with those of polycrystalline FeF_2 discussed in the preceding Chapter 3 as well as previous XPS studies of FeF_2 . [66] Normalizing the F 1s and Fe 2p intensities by their respective Scofield factors and detector functions yielded a F:Fe ratio of $(1.8 \pm 0.1):1$, confirming the stoichiometry of the film. The O 1s core level spectrum (inset (c)) is composed of three peaks. The main peak at a binding energy of -530 eV is attributed to FeO, which formed due to the oxidation of the FeF_2 film in air. [87] The F:O ratio suggests that only the topmost layer of FeF_2 was oxidized. The smaller O 1s peaks at -531.5 and -532 eV are attributed to hydroxyl and water contamination on the surface of the sample. [88, 89] These intensities are consistent with one monolayer of surface contamination. The C 1s spectrum (inset (d)) exhibits a large component at -284.8 eV and

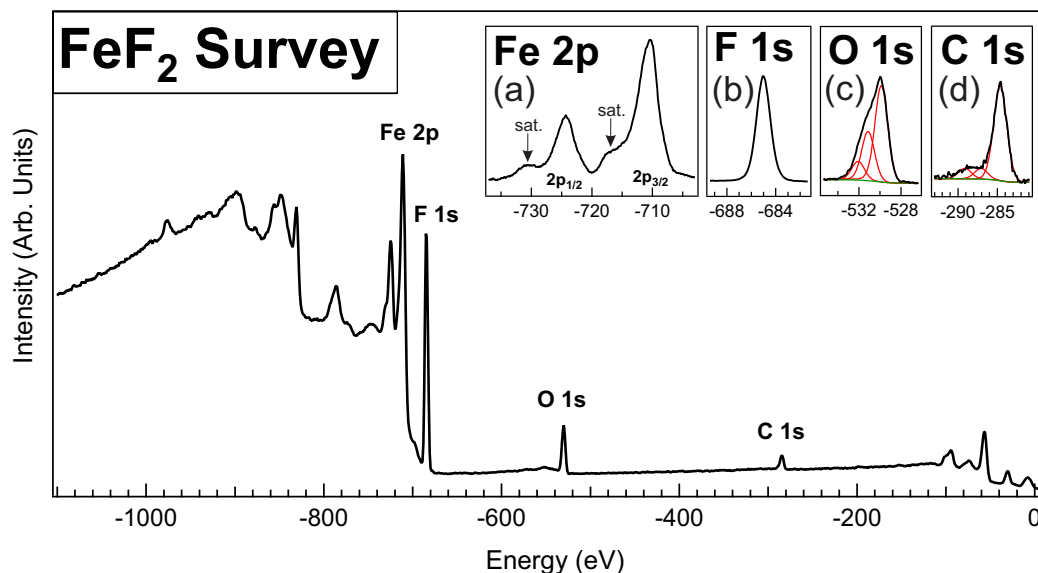


Figure 4.4: XPS Survey spectrum of an $\text{FeF}_2(110)$ film after degassing at 300°C in UHV. Inset, core level spectra indicate the presence of small amounts of hydroxyl and carbon containing species at the surface and the formation of FeO in the topmost layer of the film.

two smaller components at -287.5 and -289.0 eV. These carbon peaks are indicative of so-called “adventitious carbon” contamination, which is found on all surfaces that have been exposed to atmosphere. The total intensity of the C 1s peaks is consistent with slightly less than one monolayer of contamination on the surface of the film. [90] Despite the surface contamination present on the FeF_2 film, the formation of lithium oxides, hydroxides, and carbonates was not observed upon exposure to lithium. Indeed, the O 1s and C 1s spectra were unchanged after the lithium depositions, and hence these contaminants were not believed to significantly affect the Li- FeF_2 reaction. Due to its energy overlap with the Fe 3p core level, the Li 1s peak was again not evaluated.

4.3.2 Chemical State Analysis

The $\text{FeF}_2(110)$ film was exposed to lithium in intervals ranging from 5 to 20 minutes at a rate of about 0.07 nm/min (0.35 - 1.40 nm of Li per exposure), for a total lithiation time of 160 minutes. After each lithiation, a series of XPS spectra was acquired. In order to extract quantitative chemical information from the XPS data, a least squares fit was performed for each Fe 2p spectrum using a linear combination of reference spectra taken from pure Fe metal and FeF_2 samples (Alfa Aesar). Figure 4.5 shows a normal emission Fe 2p XPS

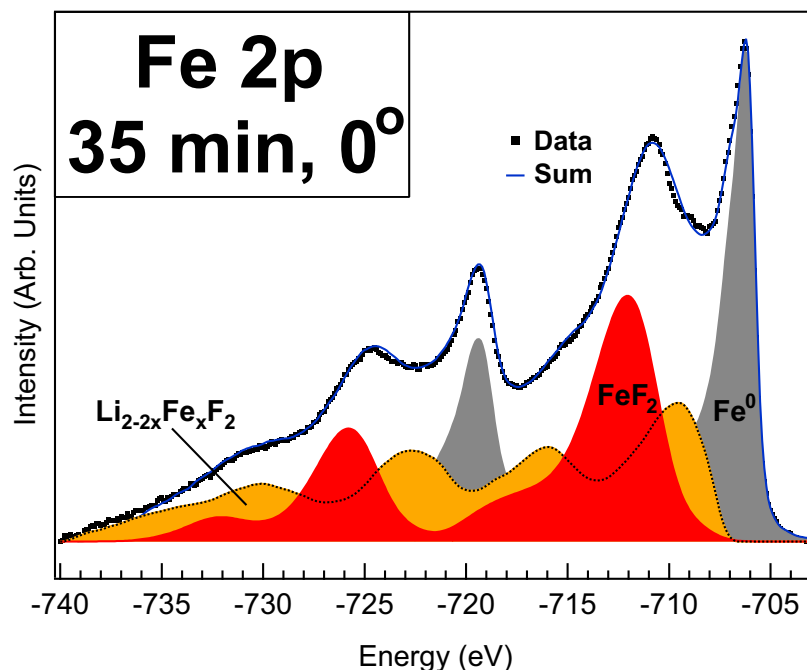


Figure 4.5: XPS spectrum of the Fe 2p core level at normal emission after the $\text{FeF}_2(110)$ film underwent 35 minutes of total Li exposure. The data is shown as black dots, and the sum of the spectral components is a solid blue line. Iron metal and iron fluoride reference spectra were obtained from high-purity samples (Alfa). Three components are needed to fit this and all other Fe 2p spectra upon lithiation, suggesting the presence of a ternary Li-Fe-F compound.

spectrum obtained after exposing the film to lithium for a total of 35 minutes. The XPS data, shown as black dots, exhibits multiple peaks corresponding to different chemical states of iron. The Fe^{2+} (FeF_2 , red) and Fe metal (Fe^0 , gray) reference spectra were not sufficient to fit the data, suggesting the presence of a third iron compound.

To account for this missing intensity, an additional spectral component was constructed from the final (160 minute) lithiation spectrum by subtracting Fe metal and FeF_2 components from the Fe 2p lineshape, as shown in Figure 4.6. This spectrum exhibited distinct peaks at -716 eV and -730 eV that could not be attributed to either Fe^0 or FeF_2 . The resulting lineshape, shown in orange in Figures 4.5 and 4.6, exhibited 2p doublet peaks at binding energies of -709 eV and -723 eV and intense satellite features at -716 eV and -730 eV.

The peak positions and lineshape of this unidentified chemical species are not consistent with any known iron fluoride, oxide, or oxyfluoride compounds. [25, 66, 91, 92] However, several recent studies provide insight into the possible nature of this compound. First,

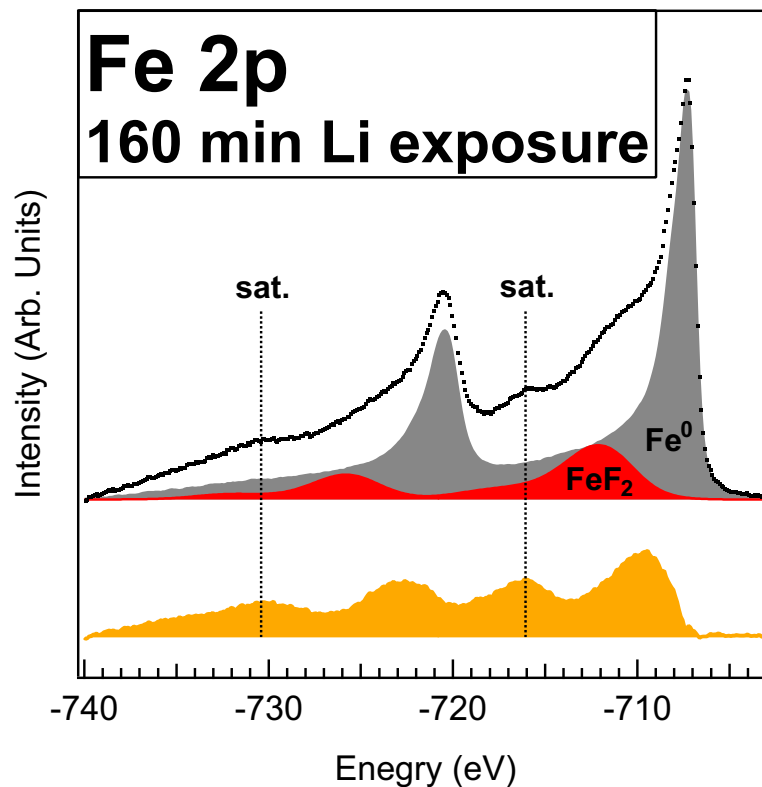
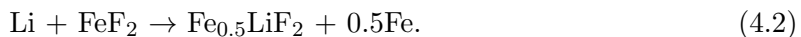


Figure 4.6: Fe 2p XPS spectrum of the FeF₂(110) sample after 160 minutes of total Li exposure. The satellite features of the Fe_xLi_{2-2x}F₂ component are clearly visible, and are not fit by any combination of iron fluoride or oxide reference spectra.

recent x-ray pair distribution function (PDF) studies of electrochemically cycled FeF₂ by Ko and coworkers [15] observed an expansion of the LiF rocksalt lattice upon delithiation. This was attributed to the incorporation of iron in the LiF lattice to form Fe_xLi_{2-2x}F₂, with x estimated to be between 0.4 and 0.5. Additionally, MD simulations by Ma and Garofalini predicted the formation of a ternary Fe-Li-F compound upon the lithiation of both FeF₂(110) single crystals and FeF₂ nanoparticles. [77, 82] Consequently, the additional Fe 2p component observed in the lithiated FeF₂ spectrum is attributed to the ternary compound Fe_xLi_{2-2x}F₂.

The Fe_xLi_{2-2x}F₂ spectral component was necessary to fit every Fe 2p spectrum acquired after the initial lithiation, and its integrated intensity was found to be between 85% and 110% that of the Fe⁰ component for every Li exposure, which is consistent with $x \approx 0.5$. This chemical species was also identified in XPS spectra of electrochemically cycled FeF₂

electrodes. [14] Using $x = 0.5$, this compound can be written as $\text{Fe}_{0.5}\text{LiF}_2$, and an alternative FeF_2 conversion reaction pathway can be described by



In the following sections, it will be assumed that $x = 0.5$, and this chemical compound will be referred to as $\text{Fe}_{0.5}\text{LiF}_2$. In subsequent measurements of thinner (5 nm) $\text{FeF}_2(110)$ films, the $\text{Fe}_{0.5}\text{LiF}_2$ component was observed to disappear completely after the FeF_2 was almost fully reacted, suggesting that it is an intermediate metastable product of the Li- FeF_2 conversion reaction.

4.3.3 Modeling the Li- FeF_2 Reaction

Figure 4.7(a) shows the normal emission Fe 2p spectra acquired after each lithium exposure. The spectra have been normalized to their maximum intensities for ease of visual comparison. The bottom spectrum in Figure 4.7(a) is the same as the Fe 2p spectrum shown in Figure 4.4. Upon exposure to lithium, new features appeared at binding energies of -707 eV and -720 eV, attributed to the $2p_{3/2}$ and $2p_{1/2}$ electronic states of iron metal, consistent with the reduction of polycrystalline FeF_2 described in Chapter 3. [25] The intensity of these features increased monotonically as a function of Li exposure while the FeF_2 intensity decreased simultaneously, in accordance with the conversion reaction proposed in Equation 4.2. The topmost Fe 2p spectrum, acquired after 160 minutes (~ 10 nm) of total Li exposure, mainly exhibits Fe^0 and $\text{Fe}_{0.5}\text{LiF}_2$ features with FeF_2 accounting for only 12% of the spectral intensity.

In order to obtain depth-resolved information from the lithiated FeF_2 film, a series of angle-resolved XPS spectra was taken at 5° increments after each lithiation. Figure 4.7(b) shows one such series acquired after 35 minutes of total Li exposure and the three Fe 2p components required to fit each spectrum. These spectra are representative of the ARXPS data acquired after each lithiation step and are presented as an example. The heights of the spectra have been normalized to the intensity of the Fe^0 features in order to enhance their visual differences. At normal emission (0°), the Fe 2p spectrum exhibits features from

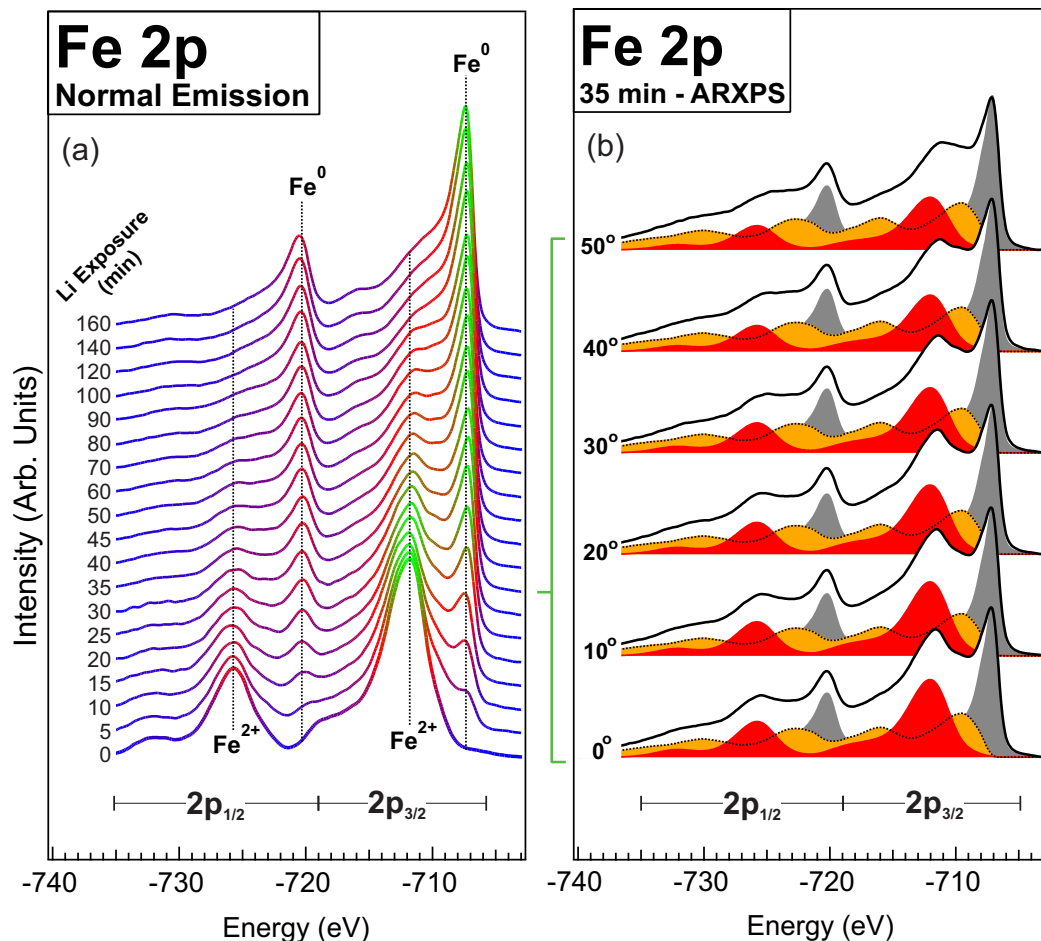


Figure 4.7: (a) Evolution of the normal emission Fe 2p XPS spectra from FeF₂(110) before and after sequential Li exposures. (b) Angular dependence of the Fe 2p spectrum after 35 minutes of total Li exposure. The spectra have been normalized by height in order to accentuate the differences between their lineshapes.

FeF₂, Fe⁰, and Fe_{0.5}LiF₂ chemical states. As the photoelectron emission angle increases, the integrated intensity of the FeF₂ component decreases relative to the Fe⁰ component. Conversely, the Fe_{0.5}LiF₂ component maintains a 1:1 ratio with the Fe⁰ component for all angles. Hence, both the Fe⁰:FeF₂ and Fe_{0.5}LiF₂:FeF₂ ratios increased as a function of emission angle. This suggests that the Fe⁰ and Fe_{0.5}LiF₂ species formed an overlayer atop the FeF₂ film. Since no angular variation in the Fe⁰:Fe_{0.5}LiF₂ ratio was observed for any Li exposure, no layering of these species is believed to occur. Furthermore, only the Fe⁰:FeF₂ ratio was necessary to calculate the thickness and uniformity of the reacted Fe_{0.5}LiF₂+Fe⁰ overlayer. Hence, the Fe⁰:FeF₂ ratio, hereafter referred to as R , was analyzed after each lithium exposure.

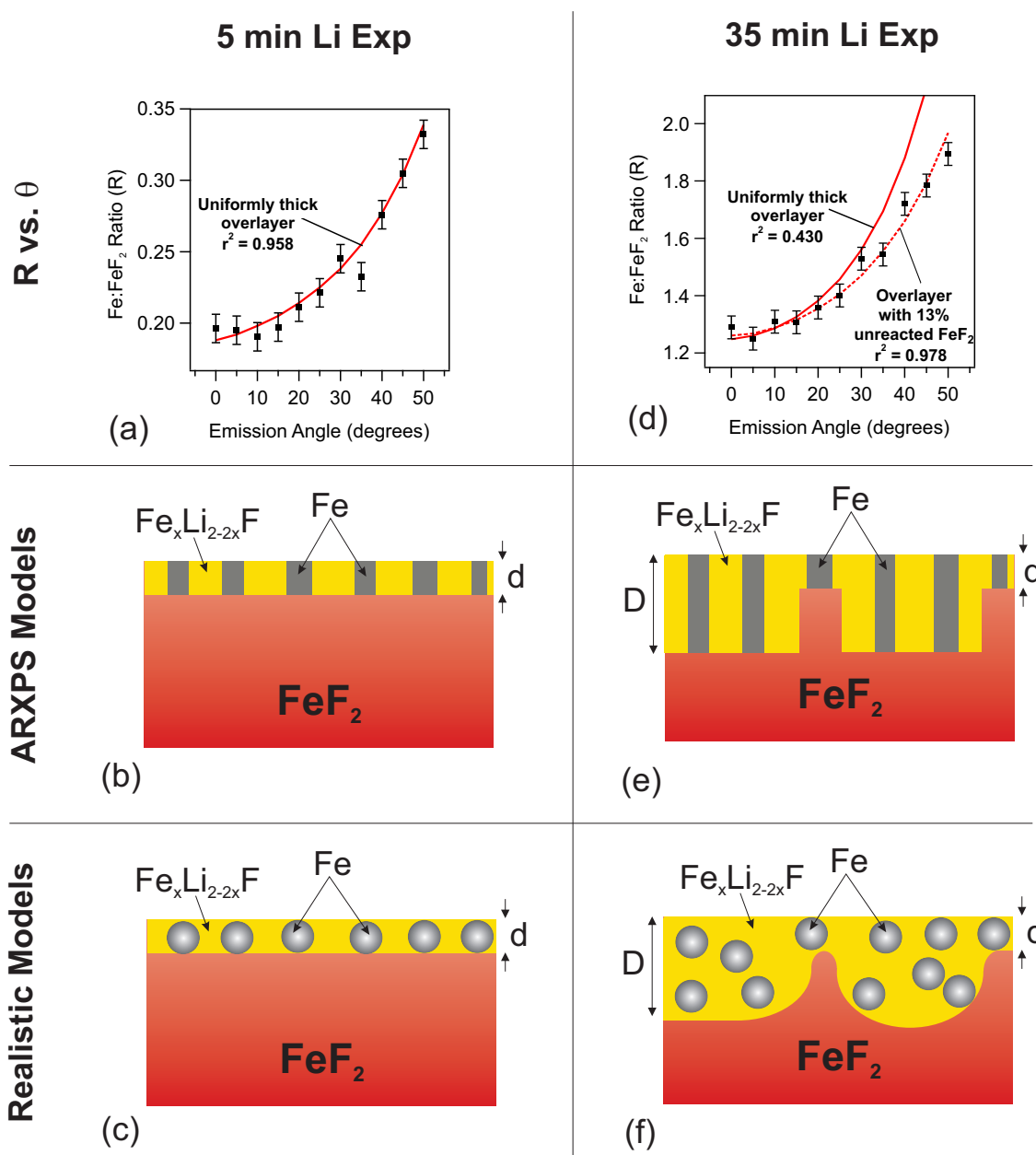


Figure 4.8: (a) The Fe⁰:FeF₂ ratio (R) versus the electron emission angle after 5 minutes of total lithium exposure, (b) corresponding ARXPS model used to generate the fit, and (c) realistic reaction model model based on MD simulations and microscopy. (d) R vs. θ for 35 minutes of exposure and corresponding (e) ARXPS and (f) realistic models.

Recall from Chapter 2 that, for a uniform layer of material A on a substrate B, the ratio $R = I_A/I_B$ of photoemission intensities is given by

$$R \approx R^\infty \left(e^{-d/\lambda \cos \theta} - 1 \right) \quad (4.3)$$

where R^∞ is a material dependent constant. Figures 4.8(a) and (d) show the function $R(\theta)$ after 5 minutes and 35 minutes of total lithium exposure respectively. The solid and dashed lines represent fits to these data based on a geometric model described below. For both 5 minute and 35 minute Li exposures, the value of R (shown as black dots) increases monotonically as a function of θ while the Fe:Fe_{0.5}LiF₂ ratio (not shown) is unchanged, again consistent with a mixed overlayer of Fe and Fe_{0.5}LiF₂ on the FeF₂ substrate. The error bars shown were calculated from the sum of the squares of the Fe 2p fit residuals. Further uncertainty is introduced by variations in the position and shape of the x-ray beam spot as the sample was tilted. However, due to the lateral homogeneity of the film and of the Li flux at the surface of the sample, this is not expected to contribute greatly to the error in the data, except after very high Li exposures for which the FeF₂ intensity is very low in XPS (and hence the value of R is very sensitive to small variations).

Figure 4.8(b) shows the idealized model of the Li-FeF₂ reactions used to generate the fit to the 5 min ARXPS data and 4.8(c) shows the corresponding realistic model based on MD simulations and prior microscopy measurements. [16, 17, 25, 77, 82] The model in Figure 4.8(b) consists of a uniformly thick overlayer composed of distinct regions of Fe⁰ and Fe_{0.5}LiF₂ which both occupy the surface of the sample. This model is motivated by the constant Fe⁰:Fe_{0.5}LiF₂ ratio. For small overlayer thicknesses ($d < 5$ nm), this approximation should be accurate since the typical dimensions of the Fe nanoparticles are expected to be between 2-5 nm. [25, 77, 82] Consequently, the particles should extend from the sample surface to the reaction interface, as illustrated in the realistic model in Figure 4.8(c). The reacted overlayer thickness is estimated to be 0.5 ± 0.1 nm based on this model, which is consistent with the conversion of about one bilayer of FeF₂. The reaction front remains planar for overlayer thicknesses up to 1.2 ± 0.1 nm (15 minutes of Li exposure).

Figure 4.8(d) shows the values of R (black data points) obtained after 35 minutes of

total Li exposure, and two fits based on Equation 2.24 assuming a uniformly thick reacted overlayer (solid red line) and a reacted overlayer with non-uniform thickness (dashed red line). The model with a non-uniform overlayer thickness, shown in Figure 4.8(e), agrees well with the data. The coefficient of determination (quality of fit) is calculated as

$$r^2 = 1 - \frac{\sum_{\theta} (f_{\theta} - R_{\theta})^2}{\sum_{\theta} (\bar{R} - R_{\theta})^2} \quad (4.4)$$

where f_{θ} is the value of the fit function at emission angle θ and \bar{R} is the mean value of R . The coefficient of determination for the fit assuming a non-uniform overlayer thickness is $r^2 = 0.978$. Hence, for this and subsequent Li exposures, the reaction model was modified to account for a non-planar interface between reacted and unreacted materials. The best fit for the 35 min data was obtained for a geometric model in which $(87 \pm 2)\%$ of the reaction front area proceeded to a depth of $D = 3.8 \pm 0.3$ nm, while the remaining $(13 \pm 2)\%$ remained at a depth of $d = 1.2 \pm 0.1$ nm. In other words, $(13 \pm 2)\%$ of the near-surface FeF_2 remained unreacted after the reaction front proceeded beyond 1.2 nm into the film. This can be understood by considering the preferential diffusion of Li along $\text{Fe}_{0.5}\text{LiF}_2/\text{Fe}$ boundaries, which leads to an inhomogeneous distribution of nucleation points in the sub-surface FeF_2 as shown in Figure 4.8(f). Again, this variation in the reacted overlayer thickness over the $\text{FeF}_2(110)$ surface is consistent with MD simulations. [77, 82]

4.3.4 Intuitive Interpretation of ARXPS Data

Equation 4 can be linearized by rearranging terms and taking the natural logarithm of both sides of the equation:

$$\ln \left(1 + \frac{R}{R^{\infty}} \right) = \frac{d}{\lambda} \sec \theta. \quad (4.5)$$

Thus, by plotting $\ln(1 + R/R^{\infty})$ versus $\sec \theta$, the curves that correspond to uniform reacted overlayers should appear as straight lines whose slopes are proportional to the overlayer thickness and whose artificially extrapolated y -intercepts are at the origin. This is explained in further detail in Chapter 2. Figure 4.9 shows the linearized $R(\theta)$ plots, which were constructed from the approximation shown in Equation 4.9.

Using this simple method of analysis provides an intuitive explanation of the relationship

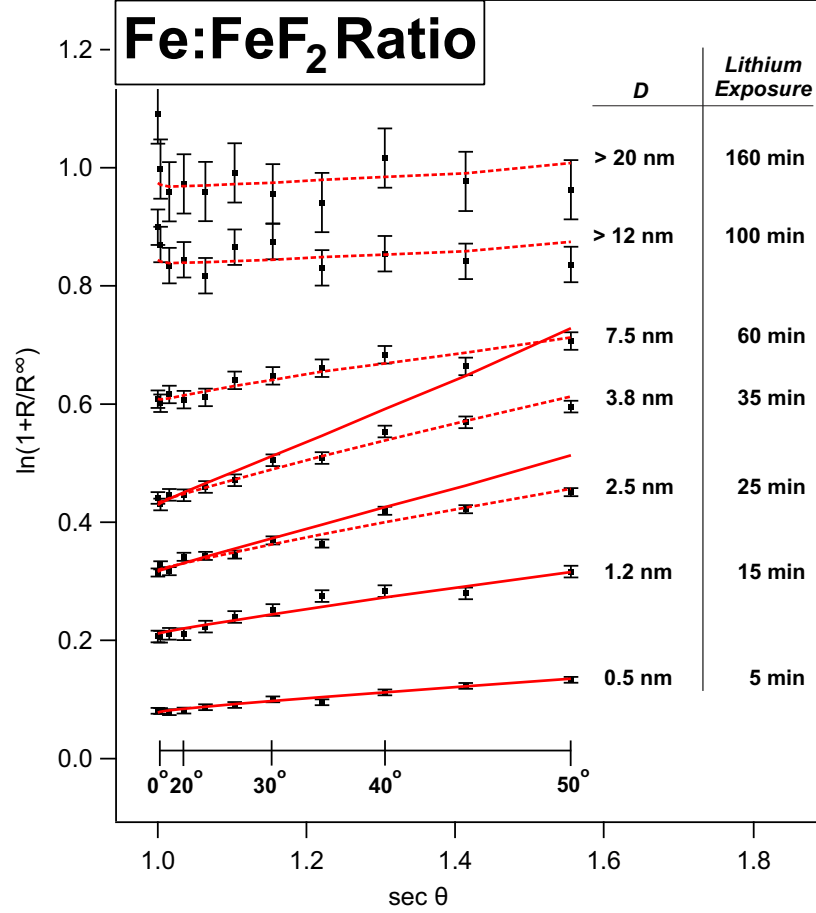


Figure 4.9: Linearized $R(\theta)$ plots for several different Li exposures. Solid red lines correspond to fits assuming a uniformly thick reacted overlayer (cf., Figs. 4.8(b) and 4.8(c)), while dashed lines correspond to fits assuming overlayers with non-uniform thickness (cf., Figs. 4.8(e) and 4.8(e)). The quality of each fit is given in Table 4.1.

between the $R(\theta)$ curves and the diagrams in Figure 4.8. The values of d , D , and the percentage of unreacted FeF_2 covered by a thin overlayer are summarized in Table 4.1. For small Li exposures (overlayer thicknesses less than ~ 1.2 nm), the reaction front proceeds uniformly through the film. Consequently, the data corresponding to 5 minutes (0.5 nm) and 15 minutes (1.2 nm) of total Li exposure are well-fit by $R(\theta)$ curves derived from uniformly thick overlayer models (shown as solid red lines). For greater overlayer thicknesses, the reaction front becomes non-planar, and hence the curves corresponding to > 25 minutes (2.5 nm and thicker) are not well fit by uniformly thick overlayer models, but instead by models with non-uniform overlayers (dashed red lines). When the reaction front proceeds deeper than the escape depth of the Fe 2p photoelectrons ($D > 10$ nm), the film appears

as a mixture of Fe, $\text{Fe}_{0.5}\text{LiF}_2$, and unreacted FeF_2 . At these large lithium exposures, the XPS data no longer varies with emission angle, and hence no information can be garnered about the depth of the reaction front. However, the amount of unreacted FeF_2 is observed to slowly decrease from $(13 \pm 2)\%$ to $(8 \pm 1)\%$, as seen by the increase in the Fe: FeF_2 ratio between the $> 12\text{ nm}$ and $> 20\text{ nm}$ curves in Figure 4.9. For these $R(\theta)$ curves, the low intensity of the FeF_2 component in the Fe 2p spectra causes a large uncertainty in the value of R . However, the position and shape of the x-ray beam on the sample also contributed to the error, which likely caused the R values for the 0° data points to differ significantly from the $R(\theta)$ fits. Despite the low coefficient of determination for the 160 minute data ($r^2 = 0.322$), the consistent increase in the R values for all angles indicates a reduction of the amount of FeF_2 in the near-surface region.

Li Exposure	d (nm)	D (nm)	% Thin Layer	r^2
5 min	0.5 ± 0.1	0.5 ± 0.1	$< 2\%$	0.958
15 min	1.2 ± 0.1	1.2 ± 0.1	$< 5\%$	0.938
25 min	1.2 ± 0.2	2.5 ± 0.3	$13 \pm 2\%$	0.955
35 min	1.2 ± 0.2	3.8 ± 0.3	$13 \pm 2\%$	0.978
40 min	1.2 ± 0.2	4.8 ± 0.4	$13 \pm 2\%$	0.938
45 min	1.2 ± 0.2	5.5 ± 0.5	$12 \pm 2\%$	0.979
60 min	1.2 ± 0.2	7.5 ± 0.7	$13 \pm 2\%$	0.907
100 min	1.2 ± 0.2	> 12	$10 \pm 1\%$	0.800
160 min	1.2 ± 0.2	> 20	$8 \pm 1\%$	0.322

Table 4.1: Depth and homogeneity of the Li- $\text{FeF}_2(110)$ reaction front for different amounts of Li exposure

These ARXPS results show that the progression of the conversion reaction into the $\text{FeF}_2(110)$ surface occurs in three distinct stages. At low lithium exposures the reaction front is planar, and hence the reacted region forms a uniformly thick overlayer on the $\text{FeF}_2(110)$ substrate. This is consistent with MD simulations, [77] and can be understood intuitively since the $[110]$ channels into the $\text{FeF}_2(110)$ film have a high kinetic barrier for Li transport which prevent lithium diffusion directly into the bulk of the film. Consequently, reaction front remains planar until the reacted overlayer reaches a thickness of $\sim 1.2\text{ nm}$. Upon further lithium exposures, the reacted overlayer thickness becomes non-uniform and can be modeled by a thick ($> 2.5\text{ nm}$) $\text{Fe}^0/\text{Fe}_{0.5}\text{LiF}_2$ overlayer occupying $\sim 87\%$ of the FeF_2

surface, while the remainder of the overlayer remains ~ 1.2 nm thick. This can also be interpreted as 13% of the near-surface FeF_2 remaining unreacted. One possible mechanism causing this non-planar reaction front is preferential Li diffusion along the $\text{Fe}^0/\text{Fe}_{0.5}\text{LiF}_2$ interfaces, resulting in localized regions in which Li is able to reach the underlying FeF_2 and react. Lastly, when the reacted overlayer becomes thicker than ~ 7.5 nm, the percentage of unreacted FeF_2 is observed to decrease from 13% to 8% upon further lithium exposures. The persistence of these unreacted FeF_2 regions suggest that the FeF_2 becomes trapped within the $\text{Fe}_{0.5}\text{LiF}_2$ matrix. This loss of active cathode material could partially explain the capacity losses observed in cycled FeF_2 cells.

4.3.5 Details of the ARXPS Calculations

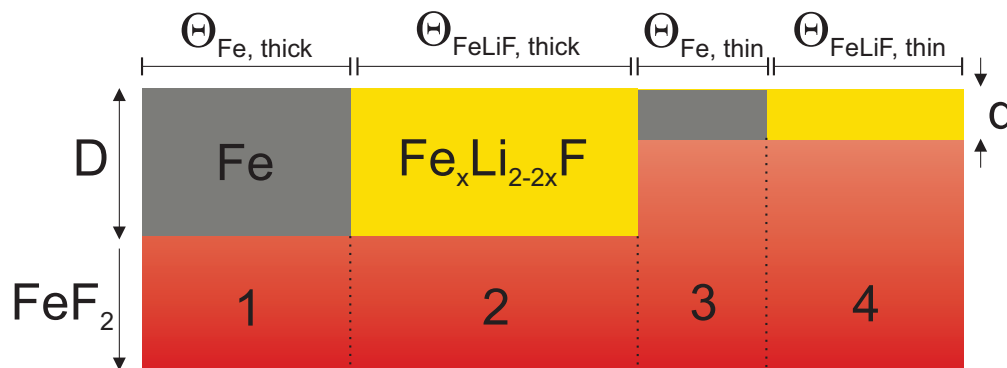


Figure 4.10: Model of the Li- FeF_2 conversion reaction used to generate $R(\theta)$ curves. The FeF_2 substrate is divided into four distinct regions of overlayer thicknesses and compositions.

The ARXPS model assumed that that FeF_2 film was infinitely thick, and the number of FeF_2 photoelectrons passing through each overlayer species was proportional to the predicted volume of that species. This is mathematically equivalent to dividing the overlayer vertically into discrete regions of thick/thin $\text{Fe}_{0.5}\text{LiF}_2$ and Fe layers (labeled 1-4 in Figure 4.10) whose fractional surface coverages are proportional to their molar volume and their stoichiometry as given by Equation 4.2. Hence, 85% of the surface was covered with $\text{Fe}_{0.5}\text{LiF}_2$, while the remaining 15% was covered by Fe^0 . This film geometry is shown schematically in Figure 4.10. The FeF_2 photoelectron signal was then calculated by summing the attenuated

photoelectron signal over the four regions labeled in Figure 4.10: [29]

$$I_{\text{FeF}_2}(d, \theta) = I_{\text{FeF}_2}^{\infty} \sum_{i=1}^4 \Theta_i \left[\exp \left(-\frac{d_i}{\lambda_i(d, \theta) \cos \theta} \right) \right] \quad (4.6)$$

where Θ_i is the fractional coverage of each region and $\lambda_i(d, \theta)$ was calculated for each species, thickness, and emission angle using a procedure described below. Similarly, the Fe^0 and $\text{Fe}_{0.5}\text{LiF}_2$ signals were then calculated by:

$$I_{\text{Fe}}(d, \theta) = I_{\text{Fe}}^{\infty} \sum_{i=1}^4 \Theta_i \left[1 - \exp \left(-\frac{d_i}{\lambda_i(d, \theta) \cos \theta} \right) \right]. \quad (4.7)$$

The ratio R was then calculated by dividing the total Fe^0 signal by the total FeF_2 signal:

$$R(\theta) = \frac{I_{\text{Fe}}(d, \theta)}{I_{\text{FeF}_2}(d, \theta)}. \quad (4.8)$$

The effective attenuation lengths were calculated using the NIST EAL Calculator. [93–96] Table 4.2 shows the EALS calculated at normal emission for each species. Similar tables were calculated at each 5° increment from $0 - 50^\circ$.

d (nm)	λ_{FeF_2} (nm)	λ_{Fe} (nm)	$\lambda_{\text{Fe}_{0.5}\text{LiF}_2}$ (nm)
0.2	1.44	1.04	2.35
0.4	1.42	1.03	2.33
0.6	1.41	1.01	2.32
0.8	1.40	1.01	2.30
1.0	1.40	1.00	2.29
2.0	1.38	0.98	2.26
3.0	1.36	0.96	2.24
4.0	1.35	0.95	2.23
5.0	1.35	0.96	2.22

Table 4.2: Effective attenuation lengths of each iron compound calculated at normal emission using the NIST EAL Database.

4.4 Conclusion

Epitaxial $\text{FeF}_2(110)$ thin films were exposed to atomic Li in an ultra-high vacuum environment as a solid state analogue for the discharge of FeF_2 conversion batteries. Chemical state analysis using XPS showed the presence of an iron compound identified as $\text{Fe}_{0.5}\text{LiF}_2$, which agrees with pair distribution function and XPS measurements of electrochemically cycled FeF_2 electrodes. [14, 15] ARXPS of the lithiated FeF_2 showed that the reaction initially proceeded in a layer-by-layer manner. This is attributed to the low diffusivity of lithium into FeF_2 [110] channels. When the reacted region became thicker than 1.2 nm, grain boundaries between the metallic Fe^0 and $\text{Fe}_{0.5}\text{LiF}_2$ facilitated preferential Li diffusion into the film, leading to a non-planar reaction front and hence regions of unreacted FeF_2 , in agreement with MD simulations. [77]

This work shows that the $\text{FeF}_2(110)$ crystalline face is reactive with Li despite the high kinetic barrier for Li diffusion directly into the crystal. However, the incomplete reduction of FeF_2 in the near surface regions suggests that FeF_2 might become trapped in the $\text{Fe}_{0.5}\text{LiF}_2$ matrix that forms upon lithiation. This could lead to a loss of active conversion material and hence a loss in capacity upon cycling as seen in FeF_2 conversion materials. Additionally, the formation of $\text{Fe}_{0.5}\text{LiF}_2$ prevents iron ions in the cathode from being fully reduced upon lithium exposure, further diminishing the charge storage capacity of FeF_2 electrodes.

In order to gain more insight into the reactivity of FeF_2 , additional ARXPS studies should be performed on the $\text{FeF}_2(001)$ surface. A thorough characterization of the $\text{Fe}_{0.5}\text{LiF}_2$ compound with TEM to determine its structure and location in lithiated FeF_2 will be crucial in developing a complete understanding of the Li- FeF_2 reaction. Additionally, a comprehensive study of the effect of Li exposure rate would shed light on the nature of the kinetic limitations of the Li- FeF_2 reactions. Lastly, the use of thin FeF_2 films on conducting substrates could also allow for STM imaging of the FeF_2 surface after small Li exposures. This would further elucidate the mechanism by which Li reacts with both the (110) and (001) surfaces.

Chapter 5

Polycrystalline Cobalt Oxide Films

5.1 Introduction

Cobalt oxide is a candidate anode material for lithium ion conversion batteries and has a theoretical charge storage capacity that is nearly double that of conventional LiC_6 anodes. In this chapter, we will discuss the reactivity of polycrystalline CoO thin films with lithium. The experimental methods will closely mirror those used to study FeF_2 . In this sense, CoO will be treated as a cathode material. The results presented here are thus relevant for the charging phase of a CoO -based conversion cell.

In order to understand the phase progression during the conversion reaction of CoO , we have performed a study of high-purity CoO polycrystalline films grown in ultra-high vacuum, sequentially exposed to atomic Li . Similar to the study of polycrystalline FeF_2 discussed in Chapter 3, the electronic structure of the pristine films and of the products of lithiation was studied using x-ray photoemission spectroscopy, UV photoemission spectroscopy and inverse photoemission spectroscopy. The crystal structure and film reorganization were examined in parallel with transmission electron microscopy.

Again, by avoiding the use of electrolytes, separators, and packaging materials, we aim to observe the intrinsic properties of the Li-CoO reaction. Similar to the studies of FeF_2 , it should be noted that these solid state chemical conversion reaction differ from typical electrochemical reactions since electrons do not flow through an external circuit, but instead arrive with the atomic Li at the surface of the active material.

Although the chemical conversion of CoO upon lithium exposure was readily observed at room temperature for low Li doses, it was found that kinetic effects resulted in significant differences in the rate of the chemical conversion process at 25°C as compared to 150°C .

This has been attributed to lithium diffusion in lithium oxide phases, which formed due to a parasitic reaction between lithium and residual gases in the vacuum chamber. These results contrast with the facile conversion of FeF_2 with lithium exposure, and subsequent formation of LiF and Fe discussed in the preceding chapters. The results presented here are relevant for conversion batteries based on various binary transition metal oxides, as the reaction products are expected to be similar for these materials. Moreover, these results might have significant implications for Li-air batteries, where the formation of lithium oxide phases and subsequent kinetic limitations are key issues. [97–102]

5.2 Sample preparation

For the spectroscopic measurements, 5 nm thick CoO films were prepared by e-beam evaporation of Co metal in a 1×10^{-7} Torr background O_2 pressure onto clean copper foil at room temperature. Copper was chosen as an inert, non-reducing substrate, which was compatible with the annealing temperatures used in this study. The Cu substrates were degreased with acetone and ethanol before loading into the vacuum chamber. They were then sputtered and annealed to at least 300°C in order to remove water and hydrocarbons from the surface before the CoO films were grown. For TEM measurements, CoO films were grown on thoroughly degassed SiO_xN_y TEM membranes from SiMPore. The rate of CoO growth in both cases was about $1 \text{ \AA}/\text{min}$, as estimated by a quartz crystal microbalance located near the substrate during film growth. Hence, each 5 nm film took about 1 hour to grow. The final thickness was confirmed *ex-situ* by Rutherford backscattering spectrometry.

As-grown samples were briefly exposed to air during transfer to the ESCALAB instrument or to the TEM. To remove surface contaminants after transfer in atmosphere, the films were degassed at 300°C for 5 minutes in the ESCALAB. XPS was used to confirm the purity and stoichiometry of the resulting CoO films. Lithiation was performed *in-situ* using a Li getter source (SAES Getters) at a rate of about $0.7 \text{ \AA}/\text{min}$ while maintaining the CoO films either at 20°C or 150°C . TEM sample were not degassed after the short exposure to air, but the effects of surface contamination using this bulk sensitive technique are expected to be negligible.

5.3 Results and Discussion

5.3.1 Characterization of the CoO Polycrystalline Films

Before discussing the conversion reaction itself, it is useful to consider the geometric and electronic structure of the initial CoO films. CoO has a cubic rock salt $Fm\bar{3}m$ structure with lattice constant $a_0 = 4.26 \text{ \AA}$. [103] The unit cell, which is shown in Figure 5.1, contains four Co^{2+} ions and four O^{2-} ions with nearest neighbor distances equal to half of the unit cell dimensions (2.13 \AA). CoO is antiferromagnetic with a Néel temperature of 289 K. [104]

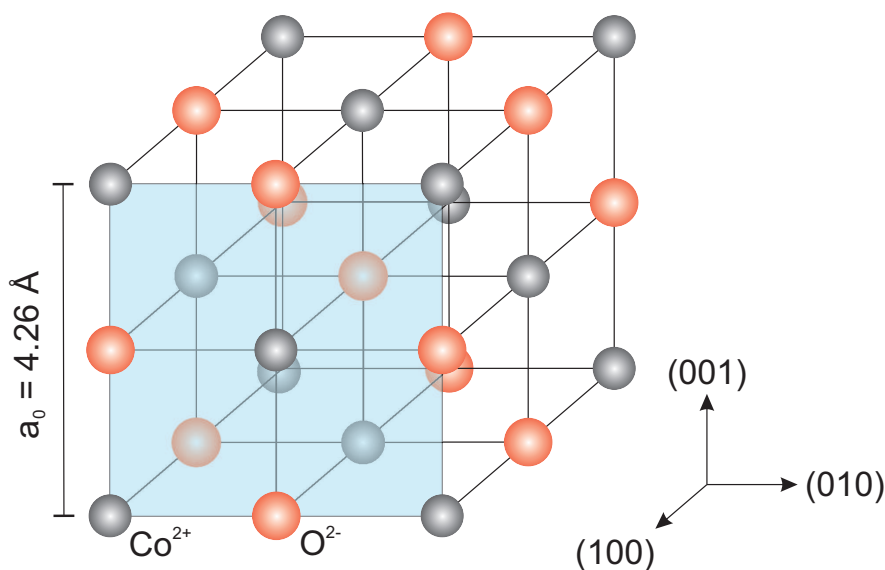


Figure 5.1: A unit cell of the rock salt CoO structure. Cobalt ions are shown in gray and oxygen ions are shown in red. The (100) surface (shaded blue) is equivalent to each of the other unit cell surfaces due to the cubic symmetry of CoO.

Figure 5.2 shows an XPS survey spectrum of the CoO film prior to lithiation, with a carbon contribution of less than 10% of the total atomic species confirming the purity of the film. The Co 2p core level spectrum, presented in the left inset of Figure 5.2, consists of two broad doublet peaks at -780.6 eV and -796.5 eV corresponding to the crystal field multiplets of the octahedrally coordinated Co^{2+} ions and shake-up/shake-off satellites components at -787 eV and -804 eV , which are indicative of stoichiometric CoO. [66, 105–108] It should be noted that no metallic Co components are visible at -778 and -793.5 eV in this spectrum, indicating the presence of only the Co^{2+} oxidation state. The corresponding initial O 1s

spectrum (inset, right) consists of a main peak at -529.9 eV attributed to O^{2-} anions in the lattice and of a smaller peak at -531.9 eV attributed to adsorbed hydroxyl species or defect structures at grain boundaries. [107] The relative intensities of the Co and O spectra in this sample indicate a Co:O ratio of $(1 \pm 0.05):1$.

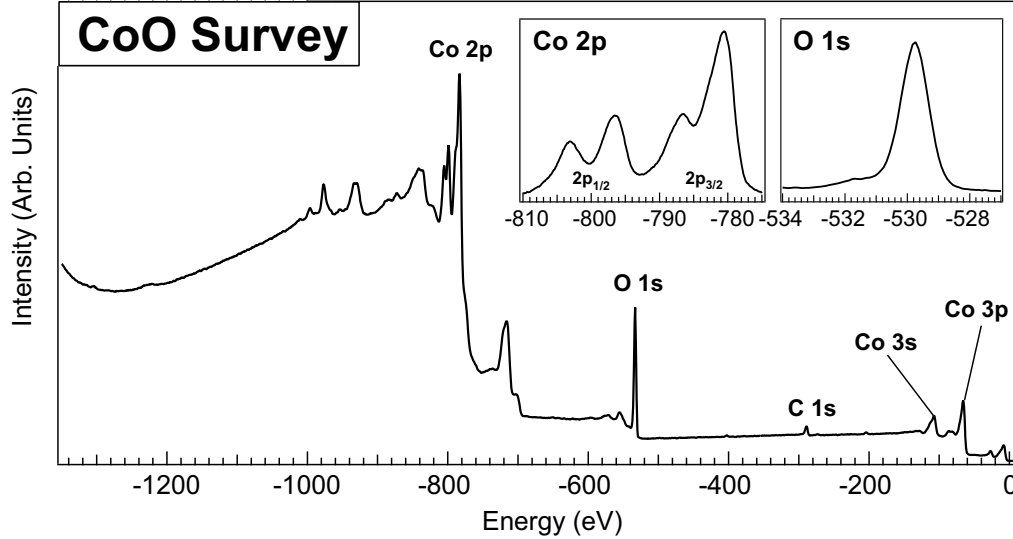


Figure 5.2: XPS survey scan of the initial CoO film after degassing. The corresponding Co 2p and O 1s core level spectra are added in inset.

The valence and conduction bands, measured using UPS and IPS respectively, are presented in Figure 5.3. As usual, the zero of energy for each spectrum is chosen as the Fermi level of the system, so that occupied states have a negative energy and the unoccupied states a positive energy. In this figure, the conduction band is a composite spectrum obtained for different incident electron energies. An electron energy of $E = 20.3$ eV was used to probe the region from 0 to 6 eV, while energies up to $E = 34.3$ eV were used for higher lying unoccupied states. Over this small range of incident electron energies, the IPS cross section is expected to change by a negligible amount. The valence band was measured using a He-II discharge lamp with a primary photon energy of 40.8 eV.

The valence band spectrum of Figure 5.3 is consistent with those of cleaved CoO(100) crystals. [109–111] The electronic states with energies between the valence band maximum and -3 eV are attributed to Co 3d-derived states, while the intensity from -3 to -8 eV is primarily due to O 2p-derived electronic states. [112, 113] The last visible structure found

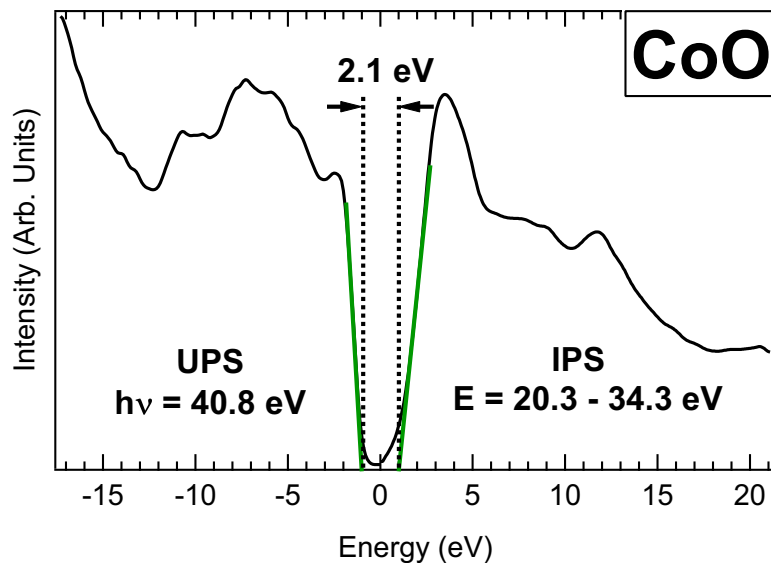


Figure 5.3: Valence band spectrum measured in UPS (energy < 0) and conduction band spectrum measured in IPS (energy > 0) of a 5 nm CoO film on Cu foil. A linear extrapolation of the band edges leads to a measure of the transport gap of CoO of 2.1 eV. The energy scale is referenced to the Fermi level of the system.

at -10 eV is attributed to a nonbinding Co d^6 electronic state. [111]

The IPS spectrum of Figure 5.3 can be compared to the unoccupied states measured previously using electron energy loss spectroscopy (EELS), [114] x-ray absorption spectroscopy (XAS), [115] and bremsstrahlung isochromat spectroscopy (BIS) [105]. The electronic transitions generated in EELS and XAS are both governed by dipolar selection rules, resulting in a partial description of the unoccupied density of states. Spectra for which the transition originates from the Co 2p level reflect a density of state weighted by the extent of hybridization between Co 3d/4s states and O 2p/3s states. Similarly, spectra measured at the O 1s-edge selectively probe states of the conduction band hybridized with O 2p states. In IPS, the unoccupied states of all orbital character are probed only weighted by the cross section of the electronic states involved in the inverse photoemission process, thus providing an approximation of the full density of states of the conduction band. This was discussed in more detail in Chapter 2. In the case of CoO, the unoccupied electronic structure has been described to first order by the octahedral ligand field splitting of hybridized Co-O states, as shown in Figure 5.4. In order of increasing energy, these states are $t_{2g} < e_g < a_{1g} < t_{1u}$. [114] Thus, using the incomplete but complementary information provided by EELS or

XAS at the Co 2p and O 1s edges, the conduction band spectrum measured in IPS can be understood as follows: unoccupied states from 0 to 10 eV are mainly due to hybridized Co 3d states, while from 10 eV to 15 eV are found Co 4s-O 2p states, followed by Co 4p-O 2p states above 15 eV.

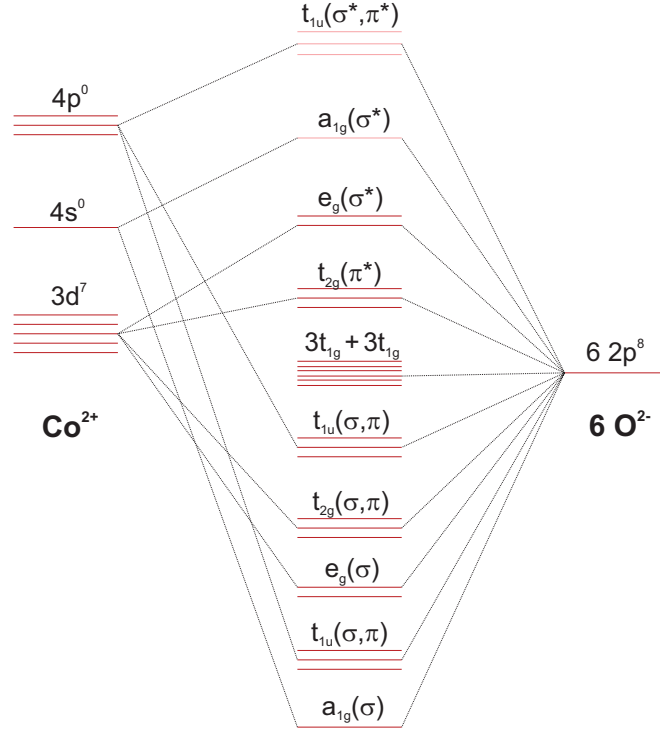


Figure 5.4: Ligand field splitting of Co core levels in an octahedral CoO_6 arrangement.

Since the valence band and the conduction band spectra are both referenced to the Fermi level of the CoO sample, the separation between the band edges is related to the electronic transport gap. By linearly extrapolating the band edges to the background of the spectra, a valence band maximum of -1.0 ± 0.1 eV and a conduction band minimum of 1.1 ± 0.1 eV can be defined. Using this method, a transport gap of 2.1 ± 0.2 eV is measured. Similar results have been obtained earlier from a combination of XPS and BIS measurements, although those measurements suffered from a larger experimental broadening. [105] The results presented here agree very well with the optical gap of 2.0 eV observed in optical absorption measurements. [116] Since the valence band maximum and conduction band minimum are both comprised of Co 3d-derived states, we can classify CoO as a Mott-Hubbard insulator, i.e. a compound which is insulating despite having a partially filled d -band.

Finally, we report the electron affinity (EA) of the CoO film. This quantity is obtained as the energy difference between the vacuum level and the conduction band minimum, measured from a combination of UPS and IPS spectroscopies. A wide valence band spectra generated from an He I radiation ($h\nu = 21.2$ eV) is measured with a -5 V applied bias on the sample. The total width of the spectrum, $W = 16.1$ eV, is extracted using a linear extrapolation of the data to the background intensity level at both the high- and low-kinetic-energy ends of the spectrum. The electron affinity is obtained as $EA = h\nu - W - E_{\text{gap}}$, where $h\nu$ is the photon source energy and $E_{\text{gap}} = 2.1$ eV is the experimentally measured transport gap from UPS and IPS spectroscopies. Using this procedure, we arrive at an electron affinity of $EA = 3.0$ eV.

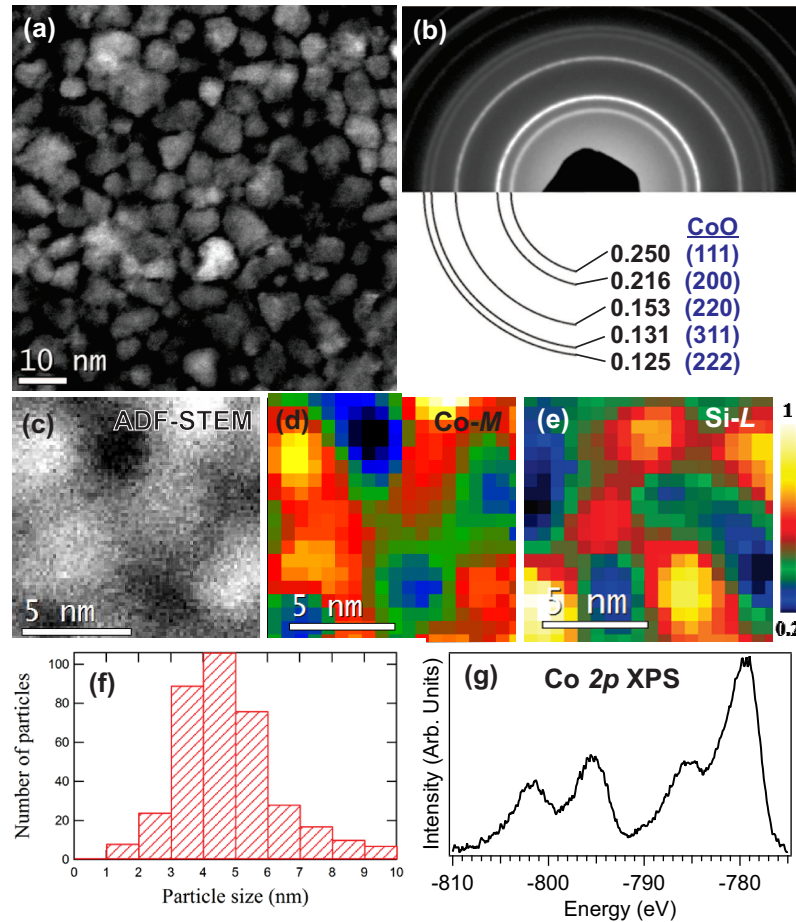


Figure 5.5: (a) ADF-STEM image of a CoO thin film on a SiO_xN_y membrane. (b) SAED pattern confirming the cubic structure of CoO ($Fm\bar{3}m$). (c) STEM image and corresponding elemental maps at (d) the Co-M and (e) the Si-L edges. (f) Size distribution of the CoO nanoparticles. (g) Co 2p XPS spectrum measured on the same film.

TEM measurements, summarized in Figure 5.5, were performed on CoO films grown on SiO_xN_y membranes in order to characterize both the morphology and the crystalline structure of the CoO films. The pristine films have been measured as-grown and after the degassing procedure in order to ensure that no changes occurred upon annealing in UHV. Small area XPS was also performed on the TEM membrane-supported films for consistency.

Figures 5.5(a) and 5.5(b) show the ADF-STEM image and the corresponding SAED pattern, respectively, for a CoO film grown on a SiO_xN_y membrane. The SAED pattern confirms the presence of the cubic $Fm\bar{3}m$ phase of CoO. In ADF-STEM mode, high-Z elements such as Co will appear as bright features. This interpretation is supported by smaller scale STEM images (Figure 5.5(c)) and its corresponding elemental maps for Co and Si (shown respectively in Figure 5.5(d) and (e)). These maps were obtained from the Co-M edge and Si-L edge EELS spectral intensity, acquired at each point of the image. In these images, Co-containing particles appear on a Si-rich background, which is attributed to the TEM thin membrane material. The CoO film thus appears as interconnected particles with an average lateral size distribution centered at about 5 nm, as shown in Figure 5.5(f). Finally, the Co 2p XPS spectrum measured on the same film confirms the presence of CoO.

5.3.2 Lithiation of Polycrystalline CoO Films

Having established the quality of the CoO polycrystalline thin films, both on the Cu substrate and on the SiO_xN_y membrane, films were sequentially exposed to an atomic lithium beam in UHV at a chosen temperature of 150°C. This temperature was low enough to prevent thermal CoO reduction, but high enough to enhance the diffusion rate of Li in the sample. [97] This aspect will be discussed in more detail in the next section.

Figure 5.6 shows the evolution of the core level and valence band spectra, measured by XPS and UPS respectively, of a CoO film grown on a Cu foil, before and after sequential exposures to Li. Despite having a low photoionization cross section at the x-ray energy used in this study, a spectral feature from the Li 1s core level (shown in Figure 5.6(a)) can be observed above the background even at the lowest Li exposures. The intensity of this feature increases after each sequential Li exposure. The broad shape of the Li 1s spectra does not allow an absolute decomposition of the chemical species present, but is consistent

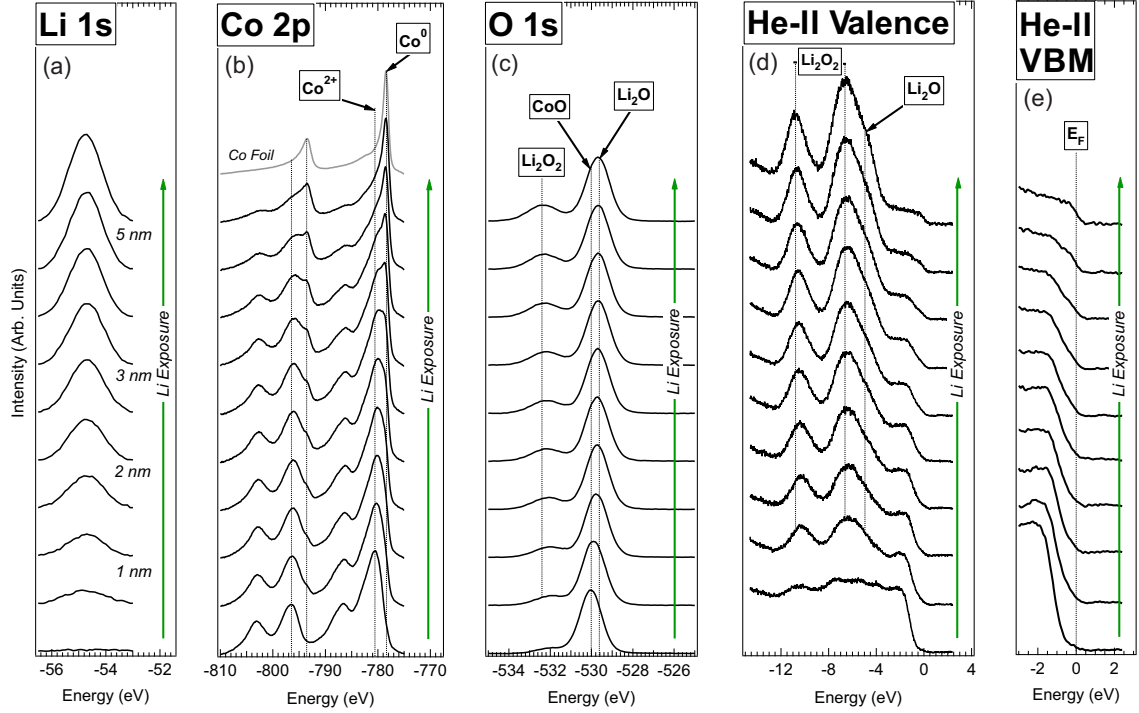


Figure 5.6: Evolution of the (a) Li 1s, (b) Co 2p and (c) O 1s core level spectra and of the (d) valence band spectra before and after sequential Li depositions. (e) A zoomed-in version of the Fermi edge region is added to emphasize the metallic edge development. Green arrows indicate increasing Li exposure. The topmost Co 2p spectrum was obtained from a clean polycrystalline Co sample and is used as a reference for metallic Co. The Li 1s spectra have been normalized to the Co amount (using the Co 3p intensity). The Co 2p and O 1s spectra have been normalized by height to accentuate visual differences between lineshapes. Valence band spectra have been normalized to the highest binding energy intensity.

with a contribution from a main peak at -54.7 eV corresponding to Li_2O and a smaller peak at -55.5 eV attributed to either Li_2O_2 or LiOH , which both have similar peak positions. [100, 108] This peak fitting scheme is justified by the analysis of the remaining core levels and by further XPS studies of lithium oxide formation in UHV. As an example of a clear Li 1s peak fit, the formation of Li_2O and Li_2O_2 on a clean Cu surface is shown in Figure 5.7.

Upon exposure to Li, new features appear in the Co 2p spectra (shown in Figure 5.6(b)) at binding energies of -778.4 eV and -793.5 eV, corresponding to the $2p_{3/2}$ and $2p_{1/2}$ states in metallic Co. [66] A reference spectrum from a clean Co foil, shown at the top of Figure 5.6(b), confirms these peak assignments. The metallic contribution to the Co 2p core level spectra increases with Li exposure. Concurrently, the features associated with Co^{2+} decrease, indicating an almost total conversion from Co^{2+} to Co^0 . In this figure, the

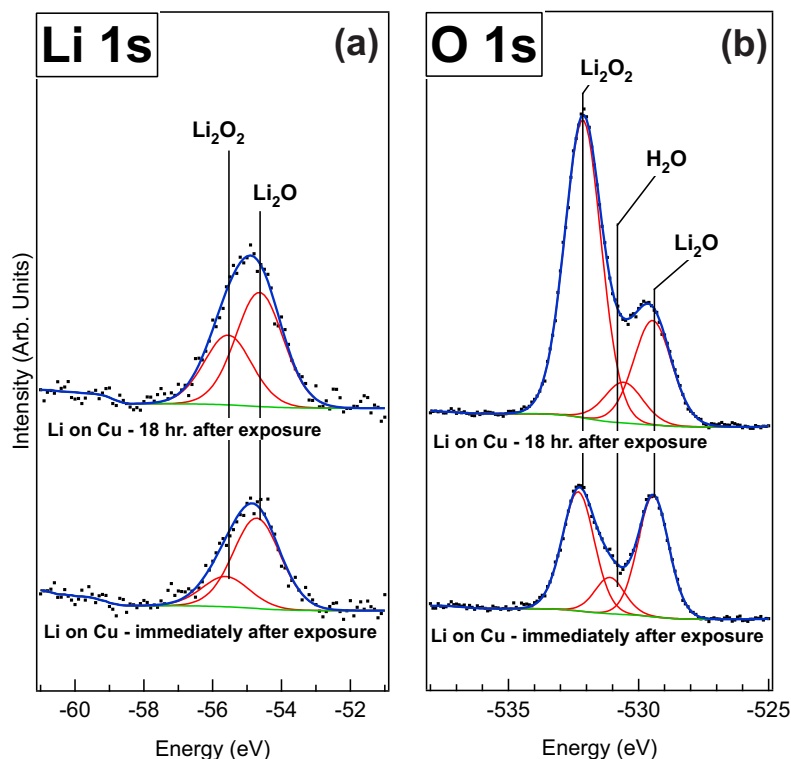


Figure 5.7: Evolution of the (a) Li 1s and (b) O 1s core level spectra of a polycrystalline Cu foil after exposure to atomic Li in UHV. The formation of both Li_2O and Li_2O_2 is observed and is attributed to the reaction of Li with oxygen and water contamination on the Cu surface and with residual water vapor in the vacuum chamber.

Co 2p peaks have been normalized by height so as to enhance the visual differences between spectra. Without this normalization, the Co 2p signal is strongly attenuated by more than two thirds from its initial intensity at the end of lithiation, indicating the presence of a thick overlayer.

In parallel, the O 1s core level spectrum shown in Figure 5.6(c), exhibits a slight broadening upon initial lithiation. This is followed by a shift to a lower binding energy as a function of Li exposure, indicating the formation of Li_2O at the expense of CoO. [108] After the final lithiation, the main O 1s peak energy is -529.6 eV. A smaller feature, which could be associated either with Li_2O_2 or LiOH , also appears at -532.0 eV immediately after the first Li exposure and grows more intense and shifts toward higher binding energy after subsequent Li exposures. The final peak position of this component is -532.4 eV, consistent with previous XPS studies of lithium peroxide formation. [117–119]

Figure 5.6(d) shows the corresponding UPS valence band spectra before and after sequential Li exposures. The lineshape of the clean CoO spectrum was described in the previous section. After the first lithiation, two new features appear at binding energies of -6.4 eV and -10.4 eV, generally attributed to O 2p states in Li_2O_2 . However, in the absence of clear experimental reference spectra, it is difficult to categorically exclude the presence of LiOH. [118, 119] These peaks grow more intense and shift toward more negative binding energy with increasing Li exposure to reach -6.6 eV and -10.9 eV respectively. A smaller shoulder at -5.0 eV, corresponding to O 2p states in Li_2O , is also observed and increases with Li exposure. [118, 119] Lastly, starting from the well defined band edge of CoO, a Fermi edge develops with increasing Li exposure, consistent with the formation of metallic Co, as shown in Figure 5.6(e). It should be noted that due to the particular photon energy used in this measurement (40.8 eV), the valence band spectra are much more surface sensitive than the XPS core level spectra. The strong contribution to the electronic structure of the Li_2O_2 bands in the valence band indicates that Li_2O_2 is most likely forming an overlayer on top of Li_2O or Co. Assuming that this is the case, a simple model using the XPS intensities of the last lithiation step of Figure 5.6, and assuming a 25 Å attenuation length in the lithium oxide compounds, one can estimate the thickness of Li_2O_2 to be about 10 Å. The exact geometry of this reaction will be characterized in further detail using STM and ARXPS in the following chapter.

Figure 5.8 shows the results of a TEM study of the morphology and structure of the final product of the lithiation reaction of a CoO film grown on a SiO_xN_y membrane and fully reduced by exposure to Li at 150°C in UHV (as confirmed by small area XPS). A large area ADF-STEM image and a SAED pattern from the resulting film are shown in Figures 5.8(a) and 5.8(b) respectively. A smaller area image, with its corresponding elemental maps at the Co-M and Si-L edges, are also shown in Figures 5.8(c), 5.8(d) and 5.8(e), respectively. The STEM images indicate a global reduction of the Co-containing particles size, with a distribution centered at 2-3 nm (as shown in the diagram of Figure 5.8(f)), consistent with electrochemical conversion studies of CoO. [24] The final particles appear interconnected, as expected from a conversion material able to sustain cyclability. [120] The Co 2p XPS spectrum shown in Figure 5.8(g) is similar to the one observed at the final lithiation step

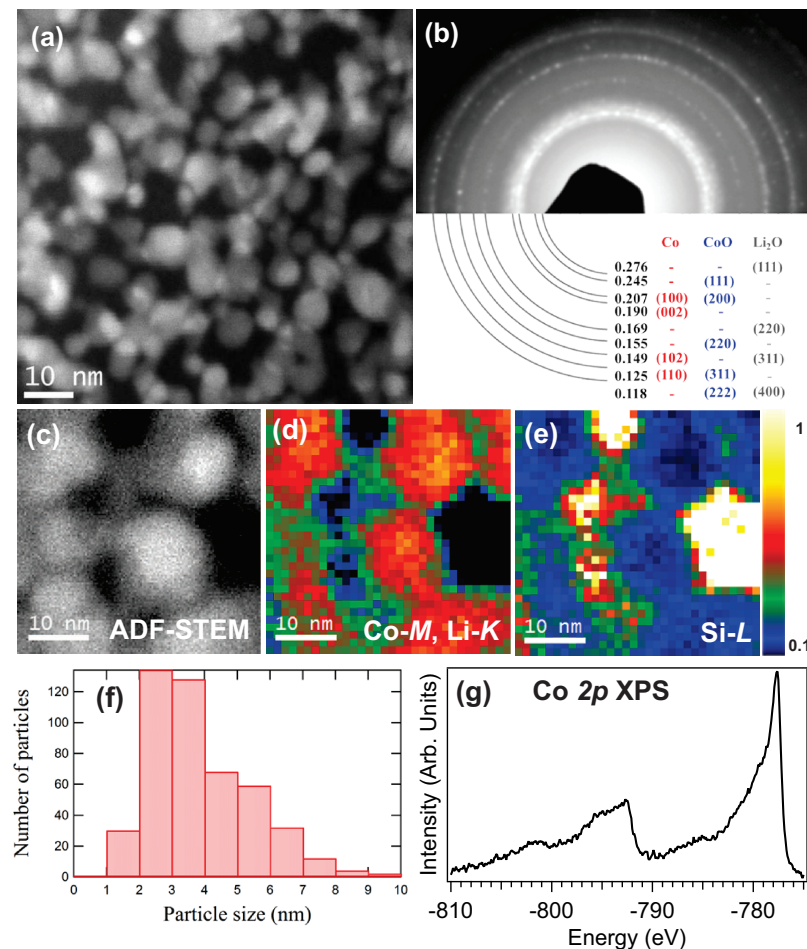


Figure 5.8: (a) ADF-STEM image of a CoO thin film on a SiO_xN_y membrane lithiated at 150°C until full CoO reduction. (b) SAED pattern revealing the presence of a mixed phase composed of Co ($P63/mmc$ symmetry), CoO ($Fm\bar{3}m$ symmetry) and Li_2O ($Fm\bar{3}m$ symmetry). (c) STEM image and corresponding elemental maps at (d) the Co-M and (e) the Si-L edges. (f) Size distribution of nanoparticles composing the final product. (g) Co 2p XPS spectrum measured on the same film.

of Figure 5.6 and indicates that a large amount of the Co is now in the metallic state. An analysis of the SAED pattern confirms the presence of a metallic Co phase (characterized by a $P63/mmc$ symmetry) and of Li_2O (of cubic $Fm\bar{3}m$ structure) coexisting with a minor component of CoO (of cubic $Fm\bar{3}m$ structure). This latter phase could be unreacted CoO, but is most likely due to re-oxidation occurring during the brief exposure of metallic Co to atmosphere upon transport to the TEM.

From these measurements, it is clear that upon lithiation, the CoO film is reduced to its metallic form, with concomitant formation of at least two lithium oxides phases, Li_2O

and Li_2O_2 (although LiOH cannot be excluded). Interestingly, these findings indicate that lithiation of a pristine CoO film under UHV conditions drives the conversion reaction to the same final products and morphology observed in electrochemical cells upon lithium ions insertion in a CoO matrix. In this experiment however, the sample temperature was maintained at 150°C during exposure to lithium, whereas electrochemical cells are typically cycled at room temperature. In the following section, a comparison of the lithiation products of CoO at 150°C and 25°C will help in understanding some mechanistic aspects of the lithiation process.

5.3.3 Comparison of High- and Low-Temperature Lithiations

A semi-quantitative analysis of the XPS data is necessary to further explore the conversion reaction mechanism. The relative concentrations of the three species Li , Co metal (Co^0 oxidation state) and CoO (Co^{2+} oxidation state) can be obtained by analyzing the Li 1s and Co 2p core level spectra shown in Figures 5.9(a) and 5.9(b). The Li 1s core level peak was sufficiently well separated from the Co 3p peak to allow the subtraction of a Shirley type background [121] and integration of the intensity over the relevant energy range (Figure 5.9(a)). Due to the absence of well-defined structure in the Li 1s photoemission peak, this intensity contains the contribution from both the Li_2O and $\text{Li}_2\text{O}_2/\text{LiOH}$ phases. Each Co 2p spectrum could then be fit by a linear combination of Co metal and CoO reference spectra as shown in Figure 5.9(b). This indicates that no other Co oxidation state was present during lithiation, unlike the multi-phase Li-FeF_2 reaction discussed in the previous chapters.

It is now possible to evaluate the extent of CoO reduction as a function of lithium exposure at 150°C and 25°C , by comparing a set of XPS data similar to that presented in Figure 5.6, but lithiated at room temperature. In Figure 5.10, the relative fractions of cobalt in the Co^0 and Co^{2+} oxidation states have been plotted as a function of a normalized detected Li coverage, i.e. the total Li 1s XPS intensity divided by the total Co 3p XPS intensity. A first look at Figure 5.10 indicates dramatic differences due to the sample temperature during Li deposition. At 150°C , the reduction of CoO into Co follows a linear trend and reaches about 80% when the Li:Co ratio reaches a value of 3:1. At 25°C , the

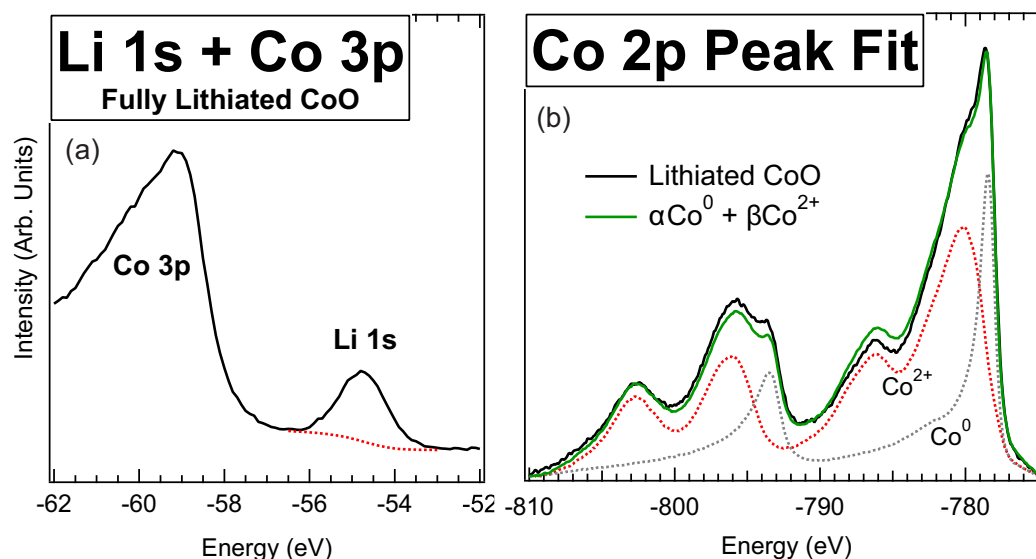


Figure 5.9: (a) XPS core level spectra of the Li 1s and Co 3p regions of the final product of the lithiation of a CoO film, showing the Shirley background used to extract the Li content of the samples. (b) Co 2p spectrum of a CoO film after several Li depositions and peak fit using a linear combination of CoO and Co reference spectra.

sample exhibits a rapid initial transformation, but after the Li:Co ratio reaches a value of about 1:1, the CoO reduction is significantly impeded, with the fraction of metallic Co slowly approaching saturation to a value less than 50% with additional Li exposures. The formation of Li_2O and Li_2O_2 in a UHV chamber was also observed in the absence of a CoO film, as evidenced by the data presented in Figure 5.7. The formation of these compounds is the result of the high reactivity of metallic lithium with the residual O_2 and H_2O partial pressures of the UHV environment (despite the low base pressure of less than 1×10^{-9} Torr). Consequently, not all of the deposited Li is available to react with CoO.

It should be noted that several assumptions have been made in order to draw quantitative conclusions from this data. The first assumption is that the partially-reacted film was a homogenous mixture of Li_2O , CoO, and Co^0 . Since XPS is exponentially more sensitive to surface layers than subsurface layers (due to photoelectron attenuation in the material), species that are preferentially found at the surface will appear much more intense than those in the bulk. The surface sensitivity of XPS is discussed in a more quantitative manner in Chapter 2, and will be explored in more detail in Chapter 6. This aspect of photoemission suggests that the relative amount of Li deposited was likely overestimated by XPS intensities

since it is likely to form an overlayer atop the CoO film. Consequently, the Li:Co ratio on the abscissa axis of Figure 5.10 is greater than the one expected for a simple conversion reaction where two Li atoms are necessary to fully reduce one CoO unit. The second assumption is that the Li 1s and Co 2p XPS spectra sampled the same depth in the film. In fact, the mean free path of electrons in solids depends strongly on their kinetic energy, increasing with electron energy in the energy range of XPS. [42] Since the kinetic energy of Li 1s photoelectrons is approximately twice that of Co 2p electrons, XPS will again tend to overestimate the amount of Li in a sample. Despite these limitations, XPS analysis allowed for direct and reproducible comparison of CoO films lithiated at different temperatures.

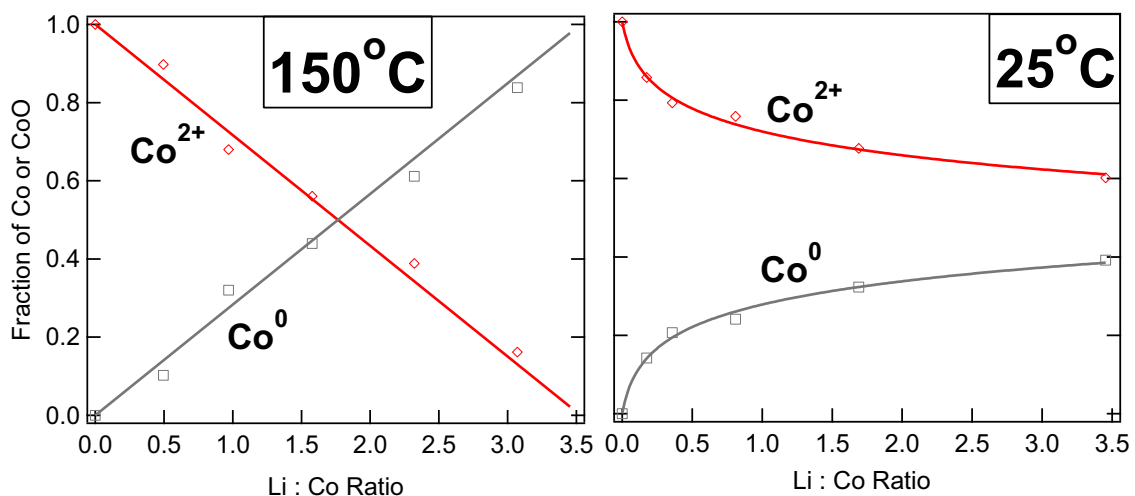


Figure 5.10: Relative amounts of Co^0 and Co^{2+} vs. Li-Co ratio as measured by XPS for a CoO film lithiated at (a) 150°C and (b) 25°C .

The formation of a Li_2O_2 layer (estimated to be 10 \AA thick based on the relative intensities of the O 1s components) is key to understanding the smaller extent of the CoO reduction at 25°C . Raising the sample temperature to 150°C did not significantly modify the amount of Li_2O_2 observed, but instead could have increases the Li diffusivity through the Li_2O_2 layer, thereby allowing the deposited lithium to react with the underlying CoO layer. From a thermodynamic perspective, the reduction of CoO by Li is highly favorable ($\Delta G_f = -1.8\text{ eV}$ per Li) and the existence of an energy barrier to this reaction is unlikely at room temperature as electrochemical conversion readily occurs. Indeed, lithiations performed at 25°C and at 150°C induced the same amount of conversion for the first two or

three sequential exposures. Only afterwards, when a $\text{Li}_2\text{O}_2/\text{LiOH}$ layer developed, did the rate of CoO reduction differ between high- and low-temperature lithiations. A similar temperature dependence has been observed experimentally in Li-air batteries, where increasing the temperature of the cell from 25 to 150°C during cycling considerably improved the rate and capacity. This was attributed to an increased permeation of Li ions in Li_2O_2 . [97] Consistent with this idea, lithium diffusion in Li_2O_2 is believed to be mediated by Li vacancies and is now thought to be a main limiting factor in Li- O_2 batteries. [101, 102] The presence of a LiOH coating at the surface of porous cathodes in Li- O_2 cells was also reported in x-ray diffraction studies, and was correlated with a loss of charge storage capacity. [122] Once again, signatures of LiOH and Li_2O_2 are not sufficiently characterized to clearly identify these compounds with our present experimental techniques. Thermodynamical considerations however, could favor LiOH: in the absence of a substantial energy barrier, the reaction of Li_2O_2 with water should be energetically favorable ($\Delta G_f = -0.45$ eV per Li) and could lead to LiOH formation.

Surprisingly, Li_2O_2 formation has not been reported in conversion batteries using CoO as an electrode. [108, 123, 124] More precisely, the lack of structural information in the electrochemical studies involving CoO , does not rule out the presence of Li_2O_2 or LiOH in these systems. It could also be argued that the stability of these lithium compounds in an electrochemical cell environment is modified in the combined presence of an electrolyte and binder. Hence, Li_2O_2 in an electrochemical cell might quickly transform into, for example, Li_2CO_3 via a reaction with carbonaceous species in the cell. [123] This or other reaction mechanisms could prevent any significant accumulation of Li_2O_2 from occurring.

The temperature dependence of the Li- CoO reaction contrasts strongly with the facile conversion of FeF_2 discussed in the preceding chapters. The formation of Li_2O_2 was not observed during the conversion of either polycrystalline or epitaxial FeF_2 films. Li oxides appeared only after the full reduction of FeF_2 when, presumably, excess metallic lithium was present at the surface of the film. This is shown in Figure 5.11. This suggests that the diffusivity of lithium through $\text{Co}/\text{Li}_2\text{O}$ is significantly lower than through the $\text{Fe}/\text{Fe}_{0.5}\text{LiF}_2$ composite formed in the Li- FeF_2 conversion reaction.

From these measurements, some important statements regarding the qualitative kinetic

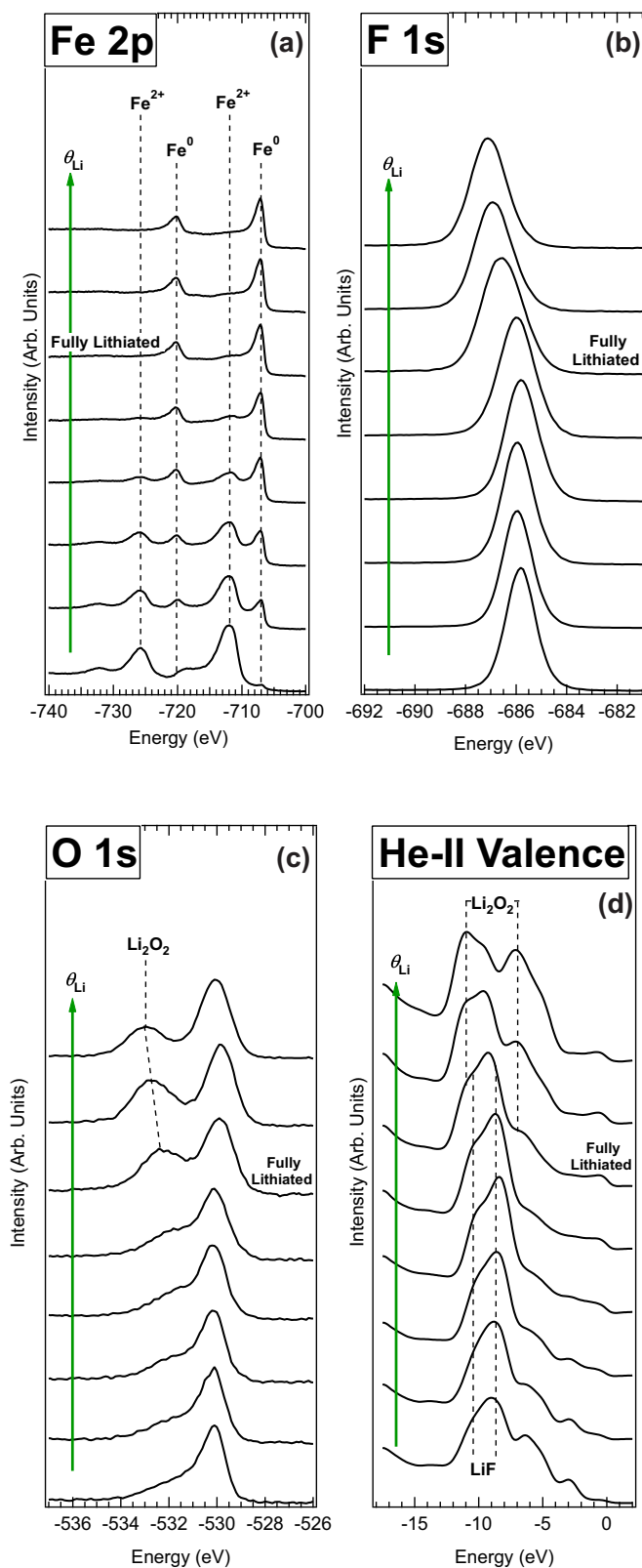


Figure 5.11: Evolution of the (a) Fe 2p, (b) F 1s, (c) O 1s, and (d) valence band spectra of an FeF_2 thin film exposure to lithium. Lithiation of the film beyond that which is necessary for full reduction of the FeF_2 results in the formation of Li_2O and Li_2O_2 .

aspects of the phase transformation during the conversion reaction of CoO can be made. Since no intermediate Co^+ oxidation state was observed during the conversion reaction, the Li diffusivity on the CoO surface was high enough to permit two Li to access each Co^{2+} site. The high mobility of lithium with respect to the mobility of Co also leads to local precipitation of small (2-3 nm) Co nanoparticles. This is important in the formation of an interconnected conducting metallic network, which would provide electrical conductivity within the insulating lithium oxide matrix. Higher Co mobility could lead to ripening of the nanoparticles and a disruption in the electrical conductivity between each particle. A similar reduction in the size of the CoO particles upon conversion has also been observed in electrochemically cycled CoO-based anodes. [24] In this respect, these results are again analogous to those observed during the conversion reaction of FeF_2 . [25]

5.4 Conclusion

Thin films of polycrystalline CoO were grown by reactive deposition of Co metal onto Cu foil or SiO_xN_y membranes in 1×10^{-7} Torr O_2 at room temperature. The overall quality of the films was probed using XPS and TEM. Additionally, using a combination of UPS and IPS measurements, the valence and conduction band spectra, as well as a transport gap of 2.1 eV and an electronic affinity of 3.0 eV were reported.

Exposure to atomic lithium can lead to full conversion with formation of Co and Li_2O , but the presence of a parasitic growth of Li_2O_2 or LiOH at the surface of the sample can suppress CoO reduction by impeding Li diffusion. The lithium oxide compounds forming an overlayer could be the result of the slower kinetics of CoO conversion (as opposed to what is observed for FeF_2 [25]) leaving metallic lithium free to react with the residual gases in UHV. This process could be exacerbated by the low lithium mobility in these oxides. [102] Full conversion was obtained at 150°C , when presumably Li diffusion is activated in the surface oxides.

The results presented here raise important considerations for conversion batteries that utilize transition metal oxide electrodes such as CoO, Cr_2O_3 , Fe_2O_3 or FeOF . The formation of Li_2O_2 or LiOH compounds has not yet been reported in electrochemical studies of metal

oxide batteries, but their presence cannot be ruled out. Hence, the poor cycling stability and voltage hysteresis in these materials could be due in part to the irreversible formation of Li_2O_2 .

The subsequent chapter will discuss the geometry of the Li-CoO reaction for two different crystalline orientations of CoO. This will elucidate the stratification of different chemical species that occurs upon the exposure of CoO to Li and provide more quantitative information about the diffusion of Li into the pristine and partially-reacted CoO films.

Chapter 6

Epitaxial Cobalt Oxide Films

6.1 Introduction

In order to study the reactivity of different CoO faces, thin films have been grown in two different orientations: CoO(100) and CoO(111). The CoO(100) surface is expected to be the predominant face exposed in CoO nanoparticles due to its low surface energy, as evidenced by the ease with which CoO crystals are cleaved along the (100) plane. However, several studies of rock salt (111) surfaces suggest that these surfaces are stabilized by hydroxyl terminations and could in fact be energetically favorable in hydroxyl-rich environments. [125, 126] Hence, it is important to consider both surfaces in order to characterize the reaction of lithium with CoO nanocomposites.

The crystalline structure of CoO is discussed in the previous chapter. The (100) surface, shown schematically in Figure 6.1(a) consists of alternating Co^{2+} and O^{2-} ions arranged in a square lattice. The CoO(111) surface can be either oxygen- or cobalt-terminated depending upon the preparation used. In the following experiments, an excess of O_2 was provided to the surface during film growth, ensuring an oxygen-terminated surface. This surface has hexagonal symmetry with nearest neighbor distances of $\frac{\sqrt{2}}{2}a_0 = 3.01 \text{ \AA}$. Assuming bulk-like termination, the CoO(111) surface can be thought of as a series of (100)-like nanofacets, as illustrated by the blue-shaded surfaces in Figure 6.1(b).

6.2 Sample Preparation and Characterization

Both sets of films were grown by electron beam induced physical vapor deposition of Co metal in an atmosphere of 3×10^{-7} Torr O_2 . The orientation of each film was determined by the choice of substrate: CoO(100) was grown on an Ag(100) single crystal following the

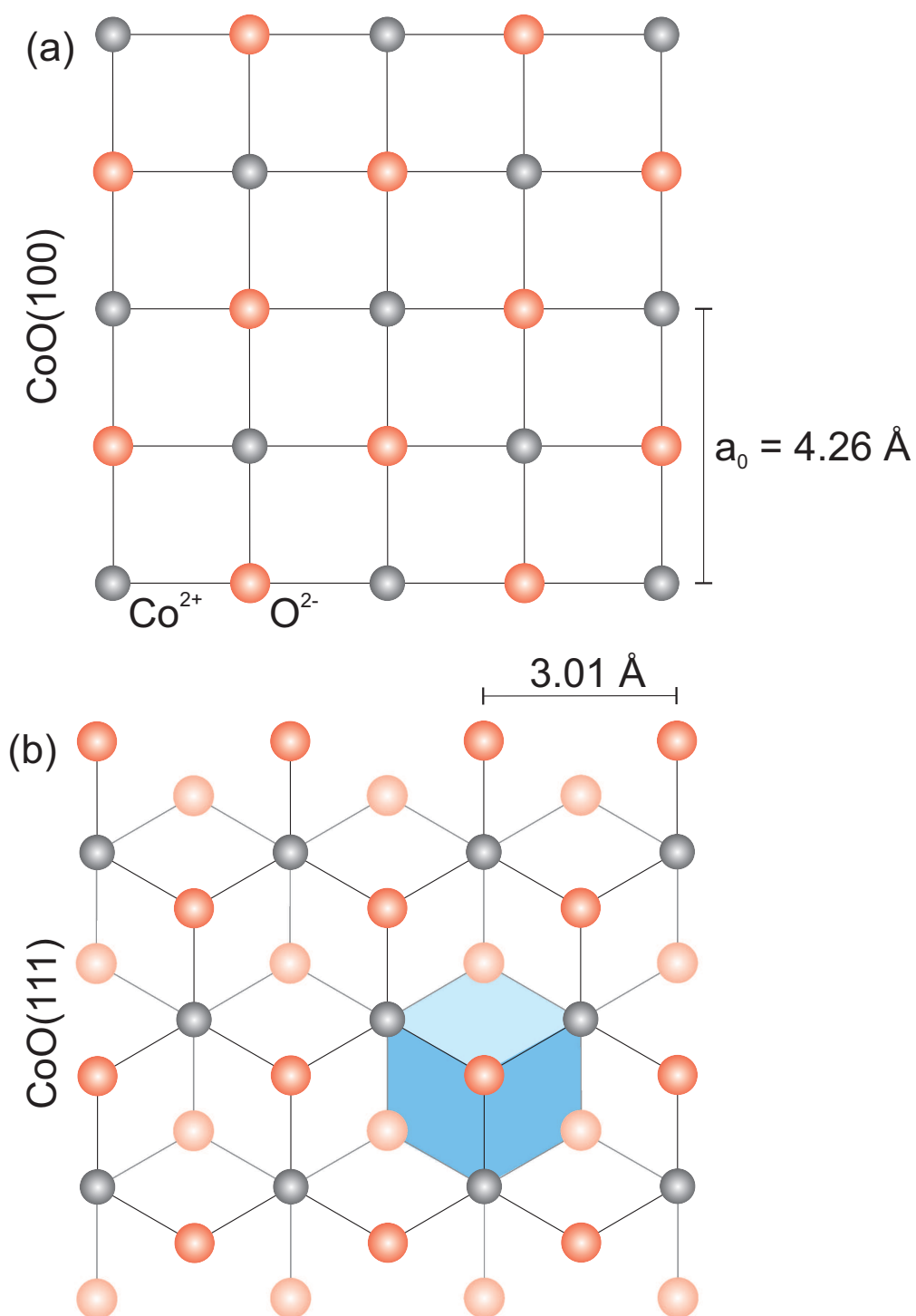


Figure 6.1: Schematics of the (a) CoO(100) and (b) CoO(111) surfaces assuming bulk-like terminations. Gray spheres are cobalt ions, while dark red and light red spheres denote surface and subsurface oxygen ions respectively. The blue cube in (b) denotes the (100)-like nano-facets on the CoO(111) surface.

procedure described by Neddermeyer and coworkers, [127–131] while CoO(111) was grown on an Ir(100) crystal following the work of Heinz and coworkers. [125, 132–141] Although the growth of these CoO films has been explored in detail in the aforementioned literature, the quality and morphology of the films varied greatly as a function of the growth parameters. Hence, the preparation of each film will be discussed here.

6.2.1 CoO(100) on Ag(100)

In order to avoid exposing the CoO films to air, sample preparation was performed in two different UHV chambers corresponding to the measurement techniques available in each chamber. For STM measurements, CoO(100) was grown in the preparation chamber of an Omicron VT Scanning Probe Microscope with a base pressure of 1×10^{-10} Torr. For XPS measurements, CoO(100) was prepared in a Thermo ESCALAB 250Xi chamber with a base pressure of 7×10^{-10} Torr. Sample preparation was identical in both chambers in order to produce films of consistent crystallinity, stoichiometry, and purity.

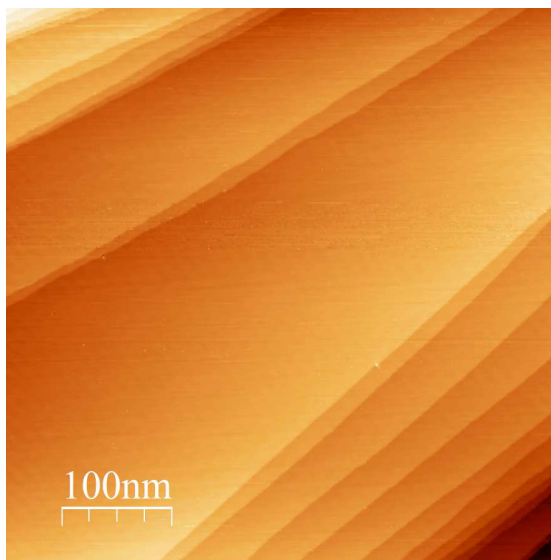


Figure 6.2: STM image of an Ag(100) surface after sputtering and annealing. Image acquired at -2.0 V and 0.5 nA.

Preparation of the Ag(100) substrate was a simple procedure, typically consisting of 1-3 cycles of sputtering with 1 keV Ar^+ ions at a sample current of $10 \mu\text{A}$ and annealing at 450°C for 10 minutes. Figure 6.2 shows an STM image of the resulting surface, which

exhibits flat Ag(100) terraces as large as 200 nm in width. Since the Debye temperature of silver is significantly lower than room temperature (~ 215 K), [142] atomic resolution of the surface was generally not possible to attain. However, LEED patterns confirmed that a well-ordered (100) surface was reliably obtained after these sputter-anneal cycles. XPS spectra of the resulting surface showed no oxygen or carbon contamination within the detection limits of the experimental setup (0.1%).

After confirming that the Ag(100) surface was clean and well-ordered, CoO(100) films were grown by electron beam evaporation of Co metal in 3×10^{-7} Torr O_2 at a rate of about 3 Å (1.4 ML) per minute. The rate of CoO deposition was monitored by a quartz crystal microbalance placed next to the substrate and periodic corrections were made to the filament current of the evaporator in order to maintain a constant growth rate. During the film growth, the substrate was heated to 200°C in order to minimize the surface roughness of the CoO. [127] Lower substrate temperatures were found to result in pillar-like growth modes. Upon reaching the desired film thickness, the Co source was turned off and the O_2 flux was maintained for 10 minutes in order to ensure that the surface was fully oxidized. The sample was then annealed at 200-300°C in UHV in order to remove weakly bound O_2 and other adsorbates from the surface.

Figure 6.3 shows STM images of two different CoO films grown using this method. For films with fractional surface coverages (left), the CoO film formed 50-100 nm domains whose boundaries were typically parallel to the (100)-like directions of the substrate. In this image, the Ag(100) substrate appears as a series of recessed domains with smooth surfaces. The CoO(100) domains, characterized by their rougher appearance and protrusion from the surface, extended across the step edges of the Ag substrate. This so-called “carpet-like” growth mode is particularly evident near the Ag region marked by the star (*) symbol in on the left side of Figure 6.3. This region shows four different layers of the substrate, whereas the surrounding CoO film consists of a single bilayer. For thicker films, such as the one on the right side of Figure 6.3, the CoO domains were smaller (10-20 nm) and had rounded boundaries. The small bright spots in this image are experimental artifacts attributed to the transfer of adsorbed species from the STM tip to the film and vice versa. The difference in film morphology between fractional and full coverage has been explained

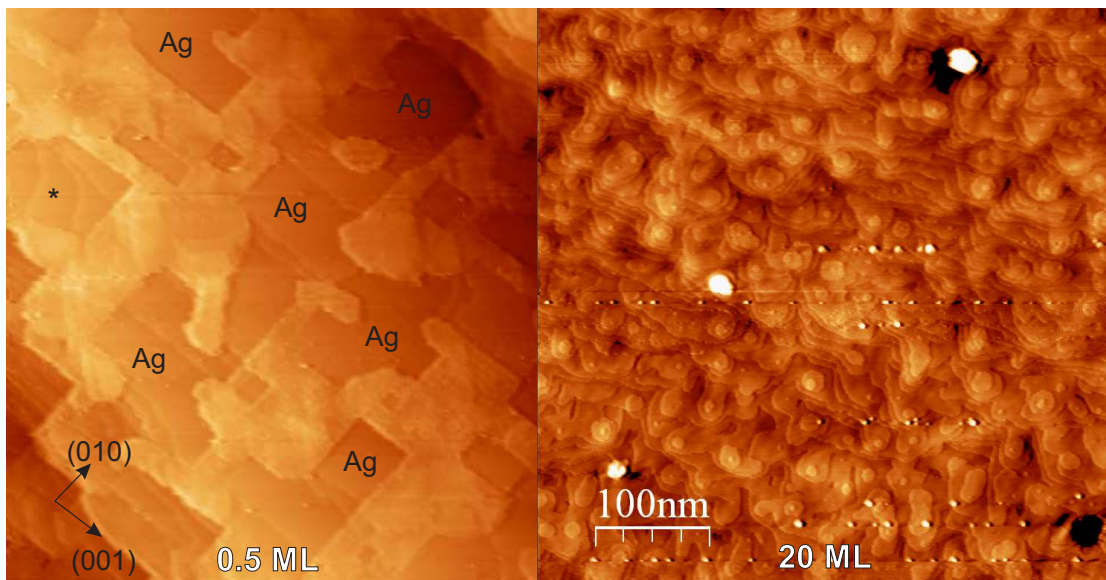


Figure 6.3: STM images of CoO(100) films 0.5 ML (left) and 10 ML (right) grown on Ag(100). At low coverages (< 1 ML), CoO forms 50-100 nm domains whose boundaries are parallel to the neighbor directions of the Ag(100) lattice. At higher coverages, CoO domains are 10-20 nm in size and have rounded boundaries. Both images were acquired at a sample bias of -2.5 V and tunneling current of 0.2 nA.

as a two-dimensional growth mode of CoO at high coverages, during which the elevated sample temperature accommodates irregular domain boundaries. [127]

XPS spectra taken from the multilayer CoO(100) films showed the presence of only cobalt, oxygen, and silver, confirming the purity of the samples. Figure 6.4 shows a survey spectrum and associated core level spectra from one such sample. The Co 2p core level (inset) is consistent with those of polycrystalline CoO, as discussed in the previous chapter. The O 1s core level (inset) was fit with a single component at an energy of 529.9 eV, which is the characteristic binding energy of O^{2-} ions in bulk CoO. No water or hydroxyl related peaks (binding energy of -532 eV) were observed in the O 1s spectrum. Similarly, the C 1s spectrum (inset) showed no signal above the background intensity, suggesting that the amount of carbonaceous contamination was less than 0.1%. The Ag 3d spectrum (inset) displayed two weak doublet peaks due to the attenuated signal from the Ag(100) substrate. Using a simple model of a uniformly thick CoO film on an infinitely thick Ag substrate, the thickness of the film was estimated to be 5.5 nm based on the relative intensities of the Co 2p and Ag 3d XPS peaks.

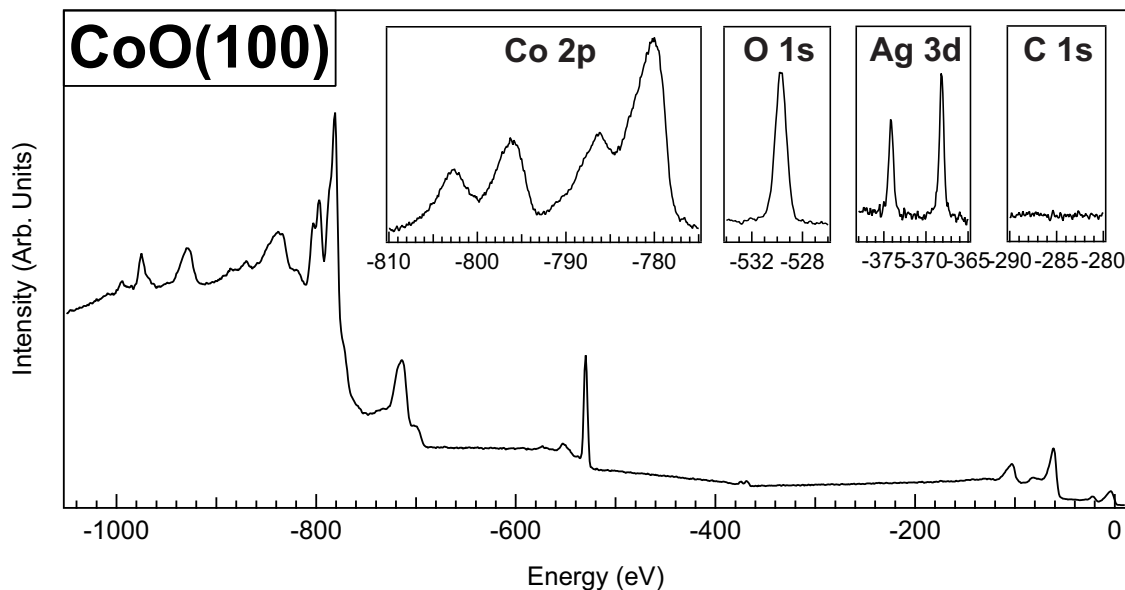


Figure 6.4: XPS survey spectrum of a CoO(100) film grown on Ag(100). Co 2p, O 1s, Ag 3d, and C 1s core level spectra (inset) confirm the purity, stoichiometry, and phase of the film.

Due to the 4% lattice mismatch between Ag ($a=4.09\text{ \AA}$) and CoO ($a=4.26\text{ \AA}$), compressive strain was induced in the CoO(100) film. [111, 129] This strain resulted in a modification of the electronic structure of CoO near the Fermi energy. Hence, ultraviolet photoemission spectroscopy (UPS) was used as a fingerprint for CoO(100). Figure 6.5 shows UPS spectra taken from CoO(100) and polycrystalline CoO. The intensity of the valence band features at -2 eV and -4 eV are significantly increased in epitaxial CoO(100). [129] This difference in the UPS spectra enabled a reliable identification of the CoO(100) surface in the XPS analysis chamber, where LEED and STM were not available.

6.2.2 CoO(111) on Ir(100)

Preparation of the CoO(111) films involved a complex treatment of the Ir(100) surface in order to obtain a flat (1×1) phase which was suitable for epitaxial film growth. First, the Ir crystal was degassed at 500°C and sputtered with 500 eV Ar^+ ions in order to remove the surface oxide and most adsorbed contaminants. Subsequent cycles of annealing at 800°C in 3×10^{-7} Torr O_2 and UHV removed the remaining carbonaceous contamination and resulted in a stable (5×1) surface, as shown in Figure 6.6(a). The (5×1) surface consisted

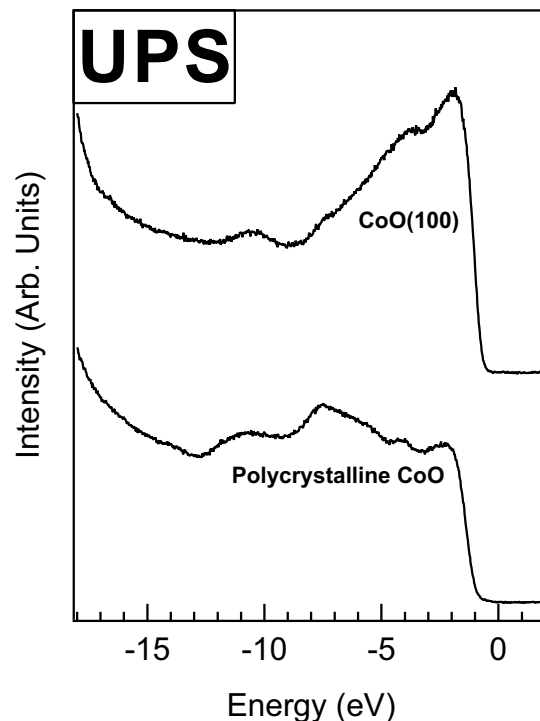


Figure 6.5: Comparison of UPS spectra acquired from an epitaxial CoO(100) film on Ag(100) and a polycrystalline CoO film grown on Cu foil. Variations in peak intensities can be attributed to the strain on the (100) film.

of raised monoatomic rows whose height was 0.5 \AA higher than the surrounding substrate. The average distance between these rows was five times greater than the lattice spacing. [133, 134, 140]

The (5×1) reconstruction could be lifted by heating the Ir crystal to 200°C in 5×10^{-7} Torr O_2 for 10 minutes. This resulted in a flat oxygen-terminated surface. The remaining oxygen was then removed by heating to 480°C in UHV for 1 minute and subsequently in 5×10^{-7} Torr H_2 for 10 minutes. The resulting surface was nearly flat, although some raised atomic rows still remained, as shown in Figure 6.6(c). If the final UHV anneal was too hot, portions of the surface reverted back to a (5×1) reconstruction. Similarly, if the O_2 dose was not high enough, the (5×1) reconstruction was not lifted entirely. Figure 6.6(b) shows a surface which is partially flat, resulting from one of the two aforementioned preparation issues. A subsequent cycle of annealing in O_2 and H_2 was then necessary to obtain a flat (1×1) surface which was suitable for CoO(111) growth.

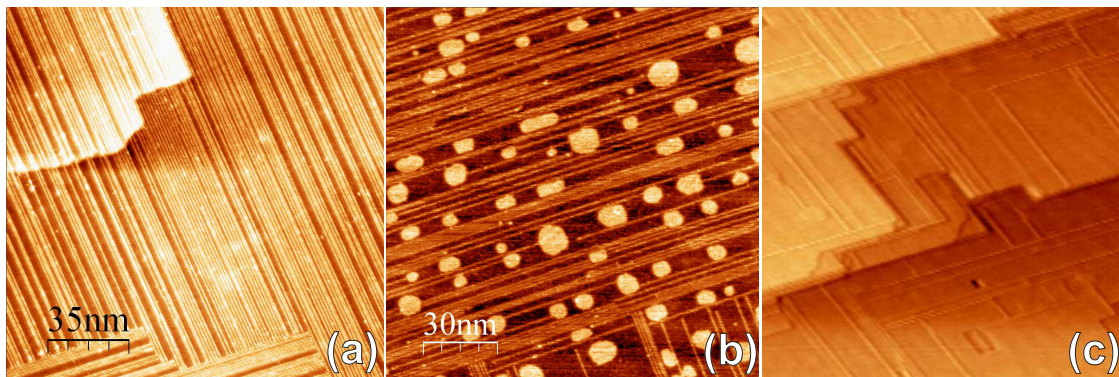


Figure 6.6: STM images of the Ir(100) surface showing the transition from a (5×1) reconstruction to a flat (1×1) phase. Images were taken after (a) annealing at 800°C in UHV (b) one cycle of O_2 and H_2 anneals and (c) two cycles of O_2 and H_2 anneals as described in the text. All frames are 150×150 nm.

Similar to the growth of $\text{CoO}(100)$ discussed above, (111) -oriented films were grown by e-beam PVD of cobalt in 3×10^{-7} Torr O_2 at a rate of about 3 \AA (1.4 ML) per minute. The Ir substrate was held at room temperature during deposition in order to prevent faceting of the polar surface during growth. [137] When the desired film thickness was reached, the Co source was turned off and the O_2 flux was maintained while the sample was heated to 250°C in order to improve the crystallinity of the film. The as-deposited film exhibited Co 2p XPS features consistent with Co_3O_4 , as expected from previous studies of cobalt oxide films. [137] Post-annealing in UHV was then used to reduce the films from $\text{Co}_3\text{O}_4(111)$ to $\text{CoO}(111)$. The temperature of the film was slowly raised to $500\text{--}600^\circ\text{C}$ until a significant increase in the chamber pressure, attributed to the production of O_2 , was observed. This change in stoichiometry was confirmed by a corresponding change in the Co 2p XPS features, which were then consistent with those of previously measured CoO films.

Due to the need for LEED and STM characterization of the Ir substrate at each step of the preparation, sample growth in the ESCALAB XPS chamber was not possible. Instead, all samples were grown in the STM chamber, transferred to the ESCALAB, and degassed to remove adsorbates. Some restructuring of the $\text{CoO}(111)$ surface was believed to occur due to this exposure. However, this should only have affected the topmost atomic layers of the film.

STM images of the resulting $\text{CoO}(111)$ films, shown in Figure 6.7, revealed atomically

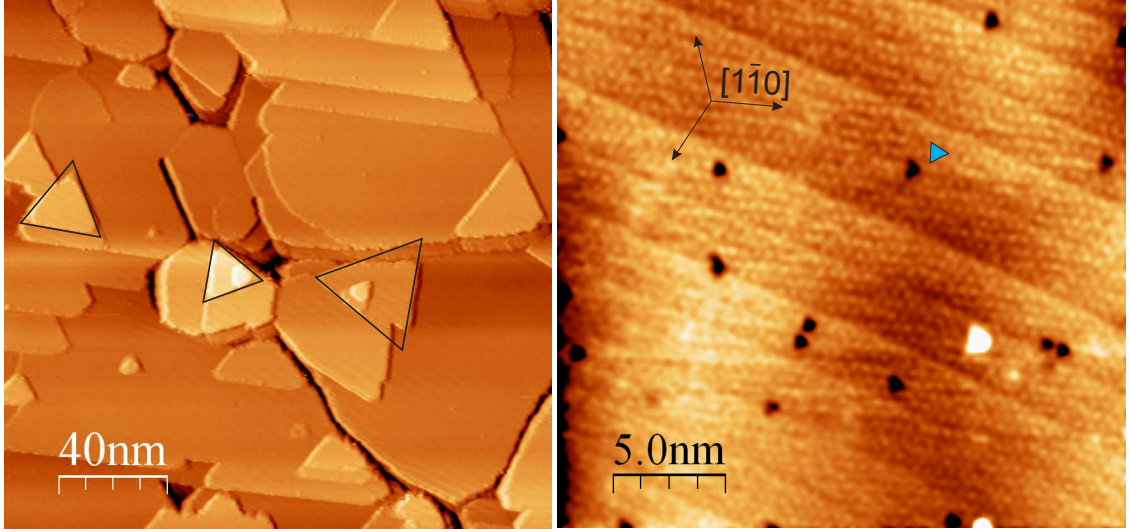


Figure 6.7: (Left) 200×200 nm STM image of a CoO(111) film grown on Ir(100) which exhibits 10-100 nm domains and step edges oriented along the nearest neighbor directions of the (111) surface. (Right) 25×25 nm atomic resolution image showing the hexagonal symmetry of the surface. Both images were acquired at a tip bias of 2.5 eV and a tunneling current of 0.2 nA.

flat domains whose lateral size ranged from 10-100 nm. The step edges of these domains were oriented along the nearest neighbor directions, forming (100)-like facets between different layers of the film. This resulted in equilateral triangular domains. Due to the four-fold symmetry of the Ir(100) substrate, neighboring CoO(111) domains were rotated from one another by 90° increments. Three triangular features, each from a different domain, are outlined in the left image of Figure 6.7. The right image of Figure 6.7 shows an atomic resolution STM image taken from the middle of a CoO(111) terrace, which confirms the hexagonal surface structure of the film. The black triangular features, which can be described by a $(\sqrt{3} \times \sqrt{3})R30^\circ$ superstructure, were attributed to surface oxygen vacancies. The boundaries of these oxygen defect features were then formed along the next nearest neighbor directions of the CoO(111) surface. An example of one such defect feature is illustrated by the blue triangle in the right image of Figure 6.7. A slight buckling or corrugation of the surface with a period of 2.6 nm and an amplitude on the order of 0.1 \AA is also visible in this image. This has previously been attributed to the result of a square Ir(100) substrate attempting to accommodate a hexagonal CoO(111) overlayer. [125] However, surface relaxation caused by the polar nature of the CoO(111) film cannot be ruled out as a contributing

factor.

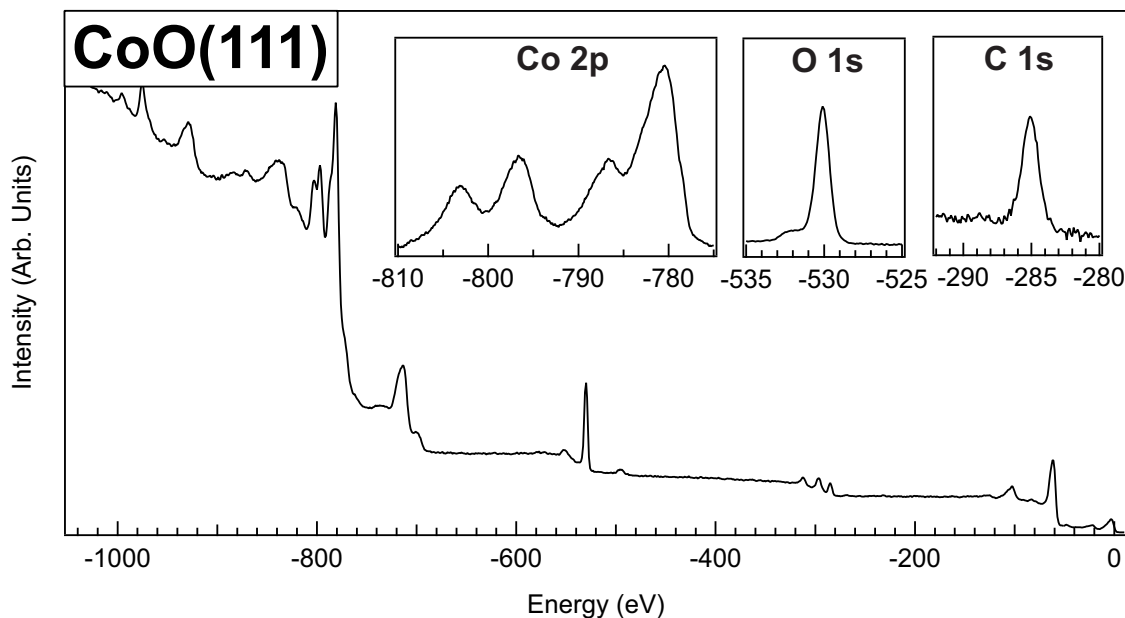


Figure 6.8: XPS survey spectrum of a CoO(111) film grown on Ag(100). Co 2p, O 1s, and C 1s core level spectra (inset) confirm the stoichiometry and phase of the film, as well as the presence of hydroxyl and carbonaceous contamination.

XPS spectra of the CoO(111) film, shown in Figure 6.8 confirmed the stoichiometry of the sample. The Co 2p and the main component of the O 1s were identical to those of the CoO(100) film. The small O 1s peak at -532 eV and the C 1s peak at -284.8 eV indicated the presence of about one monolayer of water and carbon contamination on the surface of the film due to the exposure to air. Due to the overlap of the Ir 5d and Co 3p core level peaks, the thickness of the film could not be precisely determined using ARXPS. However, due to the similarity of the growth procedure of the (111) and (100) films, this film is estimated to be about 5 nm thick.

6.3 Results and Discussion

Similar to the previously discussed CoO and FeF₂ samples, the Li-CoO conversion reaction was induced by evaporating Li from a getter source (SAES Getters) onto the surface of the film at a rate of about 0.7 Å/min. All Li exposures were performed in UHV chambers attached to the respective analysis chambers in order to avoid exposing the highly reactive

Li products to air. Lithiation was performed at 150°C in order to enhance the Li diffusivity through the Li_2O_2 overlayer, which was discussed in the previous chapter.

6.3.1 Conversion of $\text{CoO}(100)$

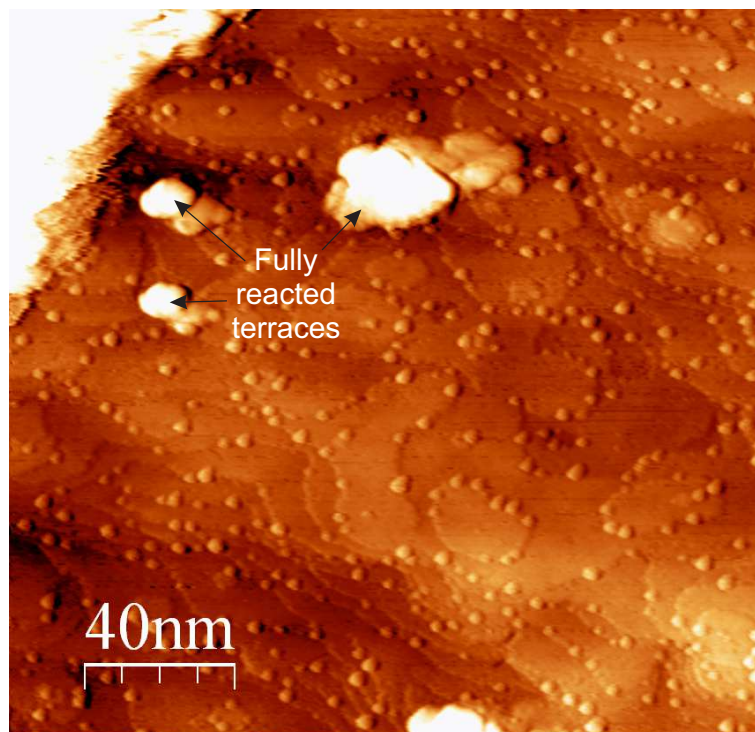


Figure 6.9: A 3 nm thick $\text{CoO}(100)$ films after 0.4 ML of Li exposure. Image acquired at +2.5 V and 1 nA.

Figure 6.9 shows an STM image of a 3 nm thick $\text{CoO}(100)$ film after exposure to about 0.4 ML Li. Bright round features with lateral diameters of 2-5 nm appear at the step edges of the CoO terraces. These are attributed to metallic Co^0 nanoparticles formed from the reduction of the CoO film. These Co^0 particle dimensions are consistent with the particle sizes observed upon the reduction of polycrystalline CoO films, discussed in Chapter 5, and with the particles observed in electrochemically reduced films. [24] The position of these Co^0 particles at the step edges of the $\text{CoO}(100)$ terraces, and the absence of particles on top of the (100) terraces, suggests that Li preferentially reacted with undercoordinated oxygen ions at edge or corner sites. This is intuitively obvious, since five bonds must be broken in order to remove a surface O^{2-} anion from the $\text{CoO}(100)$ lattice, whereas only four or

three bonds must be broken in order to remove edge or corner oxygen ions respectively. Furthermore, due to the relative instability of LiO_2 and LiO species, [143] an oxygen ion can only be removed from the CoO lattice by reacting with two Li atoms to form Li_2O . Density-functional theory calculations of Li adsorption on $\text{MgO}(100)$ [144] have shown that Li monomers diffuse on the MgO surface until reaching step edges or defect sites, where they bond with energies on the order of 1 eV. A similar diffusion process on the $\text{CoO}(100)$ surface would cause the Li-CoO conversion reaction to initiate at these sites before spreading to the rest of the film.

Bright regions with lateral dimensions of 10-20 nm and measured heights of 2-3 nm are also visible in Figure 6.9. These features can be attributed to highly reacted $\text{CoO}(100)$ domains. A simple calculation using the relative volumes of the reactants and products suggests that a volumetric expansion of 80-120% is associated with the conversion of CoO (the exact percentage depends upon the amount of Li_2O that has transformed into Li_2O_2). Hence, the height of the reacted features above the unreacted $\text{CoO}(100)$ surface is approximately equal to the depth of the reacted material beneath the surface. This suggests that the reaction in these bright regions has penetrated the full thickness of the film. This anisotropy in the surface reaction further suggests that Li is highly mobile on the $\text{CoO}(100)$ surface, possibly due to the elevated temperature at which the Li exposure was performed. The preferential reaction of CoO terraces also suggests that a partially-reacted $\text{CoO}(100)$ surface region is more susceptible to further reduction. This could be due to the enhanced diffusivity of Li into the reacted $\text{CoO}(100)$ surface, as seen in the reduction of $\text{FeF}_2(110)$ films, or to the higher density of surface defects induced in the partially reacted regions.

The wide band gaps of Li_2O (~ 7 eV) [145] and Li_2O_2 (~ 6 eV) [146] most likely preclude these species from being imaged in STM. Their presence can instead be inferred from the grainy or streaky nature of the post-lithiation STM images. This is particularly evident in the high resolution images of the CoO surface shown in Figure 6.10. These streaks, which are always aligned with the scanning directions of the STM, can be partially attributed to interactions between the STM tip and mobile $\text{Li}_2\text{O}/\text{Li}_2\text{O}_2$ conversion reaction products on the surface of the CoO film. Direct confirmation of the presence of lithium oxides was, however, possible with XPS, which will be discussed in detail below.

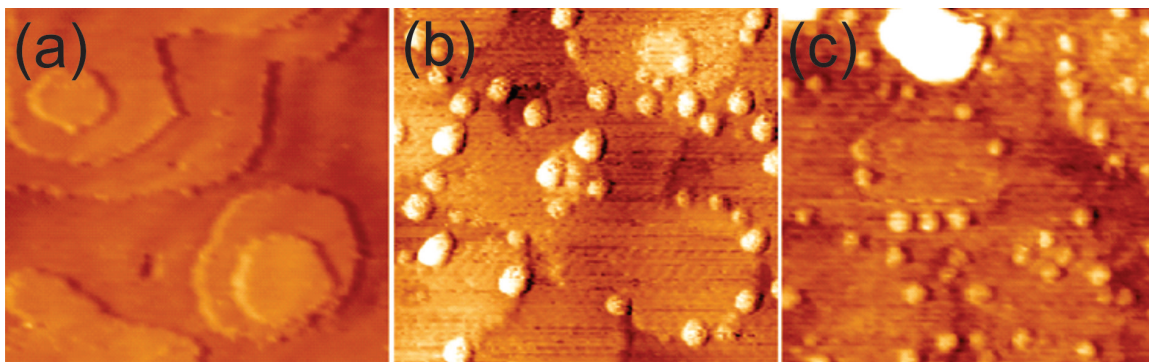


Figure 6.10: STM images of a CoO(100) film (a) as grown, (b) after exposure to 0.2 ML Li, and (c) after exposure to 0.4 ML Li. All images are 50×50 nm and were acquired at +2.5 V and 1 nA.

Figure 6.11 shows a CoO(100) film with fractional surface coverage after exposure to 0.4 ML of lithium. Similar to the 3 nm film, small CoO^0 particles and large reacted terraces are visible on the surface upon lithiation. The reacted terraces are clustered around the regions of exposed Ag(100) substrate, suggesting that the Ag acted as a conduit for Li diffusion into specific CoO domains. This also suggests that the initial nucleation sites of the Li-CoO(100) conversion reaction provide preferential sites for further Li diffusion into the surface, thus allowing some CoO domains to completely react while the rest of the surface remains mostly unreacted. This aspect of the CoO(100) conversion reaction is significant, since a CoO electrode in an electrochemical environment will have an inhomogeneous solid-electrolyte interface layer which similarly acts as a conduit for Li diffusion into specific CoO particles or domains. Thus, in an electrochemical cell, some CoO particles will react completely and immediately upon exposure to lithium, while others will remain unreacted. This could lead to uneven degradation of CoO electrodes in electrochemical cells, which could shorten the useful lifespan of the cell.

For lithium exposures greater than one monolayer, the reacted CoO surface could no longer be imaged using STM due to the insulating nature of the reaction products. ARXPS was then used to probe the stoichiometry of the CoO film after each lithium exposure. Similar to the procedure described in Chapter 4, the sample was rotated with respect to both the x-ray source and the electron analyzer such that the emission angle could be varied from 0° - 50° . A series of core level spectra was then taken at 5° increments. Figure 6.12

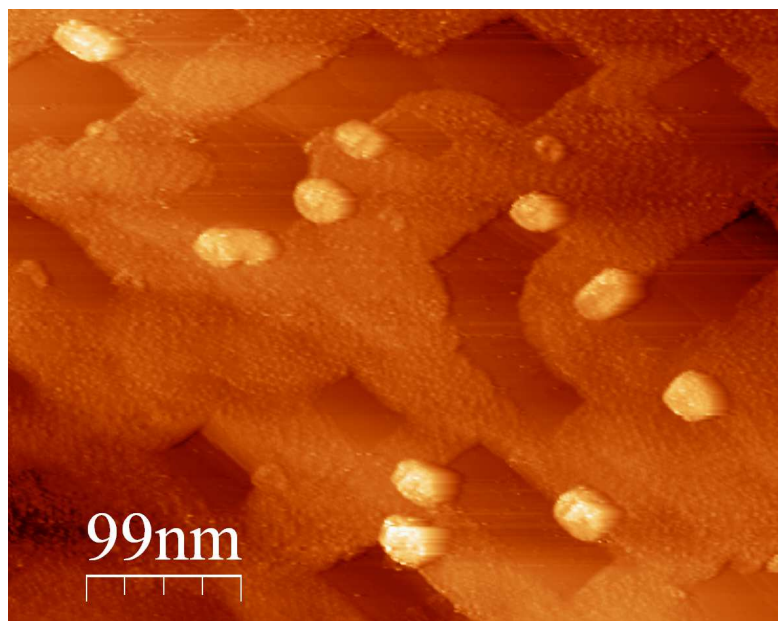


Figure 6.11: A fractional coverage CoO(100) film after 0.4 ML of Li exposure. Image acquired at +2.5 V and 1 nA.

shows a representative sample of ARXPS data and corresponding ratio plots after about 2 ML of Li deposition. The Co 2p, O 1s, and Li 1s core levels were analyzed, and each core level provided complementary information that could be used to calculate the geometry of the lithiated CoO(100) film.

Similar to the analysis used for polycrystalline CoO, the Co 2p lineshape could be fit with a linear combination of Co metal and CoO reference spectra, as shown in Figure 6.12(a). This again suggests that no intermediary compounds formed during the reduction of CoO. The relative intensities of the metallic and oxide components were then used to calculate the Co:CoO ratio as a function of angle, shown in Figure 6.5(d), which in turn was used to find the amount and geometry of the Co^0 conversion reaction product. A simple analysis shows that since the Co:CoO ratio increased as a function of emission angle, the Co^0 must have formed an overlayer atop the remaining unreacted CoO. The exact geometry of this overlayer could then be determined by modeling the XPS intensities and constructing an $R(\theta)$ curve (red line, Figure 6.12(d)) for each lithium exposure. This will be discussed in further detail below.

The O 1s spectrum could be decomposed into two distinct components, as shown in

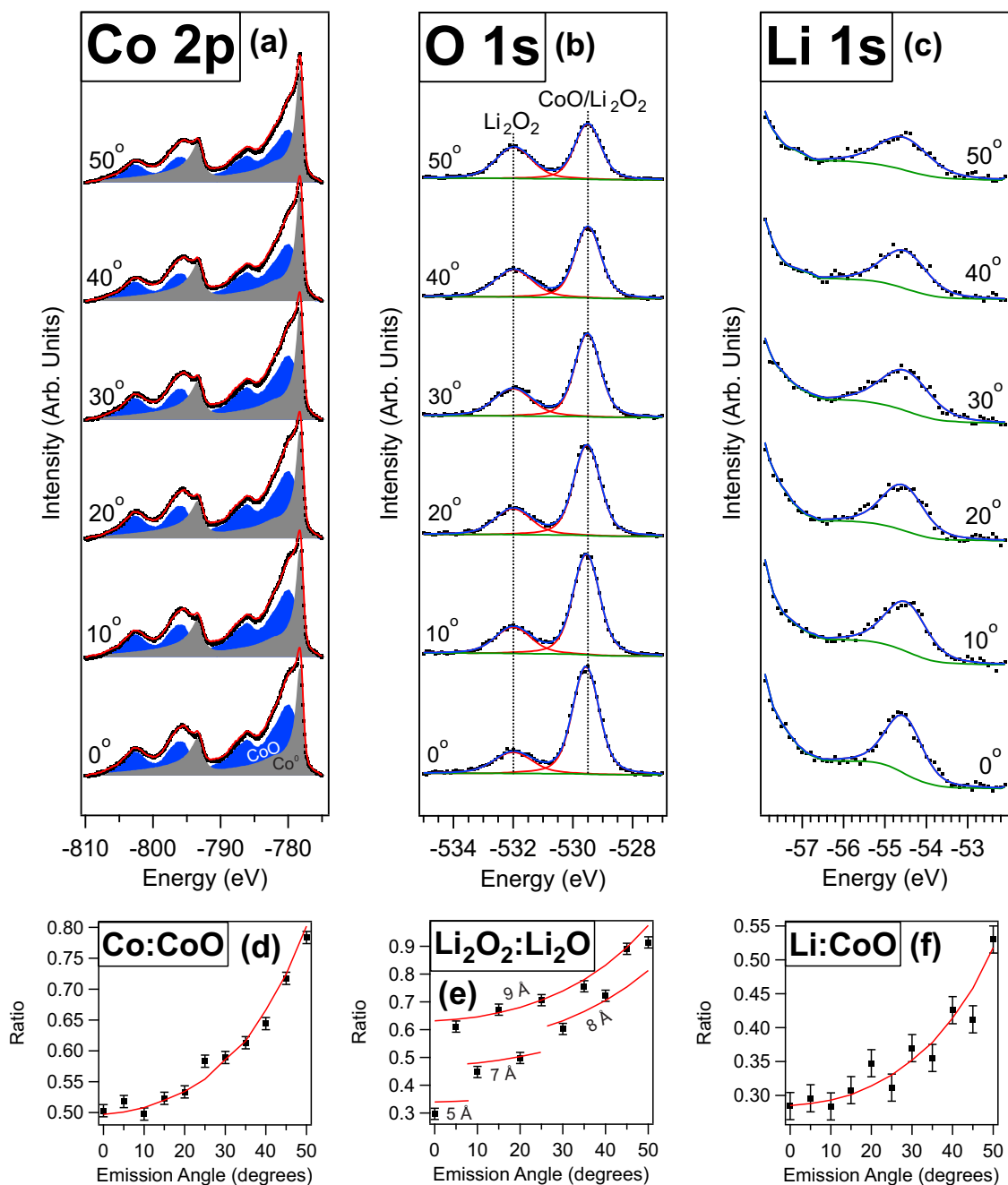


Figure 6.12: ARXPS spectra of a CoO(100) film after 2 ML of Li exposure. The geometry of the sample can be determined by simultaneously fitting the Co:CoO, Li₂O₂:Li₂O, and Li:CoO ratios.

Figure 6.12(b). The peak at -529.5 eV is attributed to both CoO and Li₂O, whose O 1s electronic states are nearly energetically degenerate. [147] The peak at -532 eV is attributed to Li₂O₂, which formed from the reaction of Li₂O with residual O₂ or H₂O vapor in the UHV chamber. The Li₂O₂:(Li₂O+CoO) ratio (hereafter abbreviated as Li₂O₂:Li₂O) also generally increased as a function of angle. However, the ratio at angular integers of 10° (0°, 10°, 20°, 30°, 40°, 50°) were consistently lower than those of the intermediate angles (5°, 15°, 25°, 35°, 45°), as seen in Figure 6.5(e). This is due to the growth of the Li₂O₂ overlayer over the duration of the ARXPS measurements, each of which typically lasted 6-8 hours. Since the 10° increments were measured first, the thickness of Li₂O₂ overlayer increased by several Angstroms before the data for the intermediate angles was acquired. Hence, several $R(\theta)$ curves were calculated for each set of O 1s data, as shown in Figure 6.5(e). The thickness of the Li₂O₂ overlayer consistently increased by about 5 Å during each set of ARXPS measurements.

Lastly, the intensity of the Li 1s signal was measured at each angle, as shown in Figure 6.12(c). In principle, the Li 1s could be fit by two components at -54.5 and -55.5 eV, representing the Li₂O and Li₂O₂ peaks respectively. This is the reason for the apparent broadening of the peak from 0° to 50°. However, the intensity of the Li 1s signal was generally too low to enable a reliable peak fit. Despite this, the total Li 1s intensity could be used to calculate the thickness of the lithium oxide/peroxide overlayer on the CoO substrate. Since the total thickness of this layer was not greatly affected by the oxidation of Li₂O₂ during the ARXPS measurements, a single $R(\theta)$ curve could be used to fit the data, as shown in Figure 6.5(f).

Using the ARXPS data acquired after each Li exposure, a model of the full Li-CoO(100) reaction can now be constructed. Similar to the model used for the Li-FeF₂(110) reaction, the geometric model for Li-CoO(100) assumed that the Li₂O and Co⁰ formed an overlayer on the unreacted CoO(100) substrate. The surface coverage of each species was then constrained to be proportional to the specific volume of that species. The model used two different overlayer thicknesses, whose values (D and d) and fractional coverages (Θ_D and $\Theta_d = 1 - \Theta_D$) could be varied to fit the ARXPS data. An Li₂O₂ overlayer was assumed to be present in a uniform (though time-dependent) thickness $d_{\text{Li}_2\text{O}_2}$ over the Li₂O/Co⁰ layer.

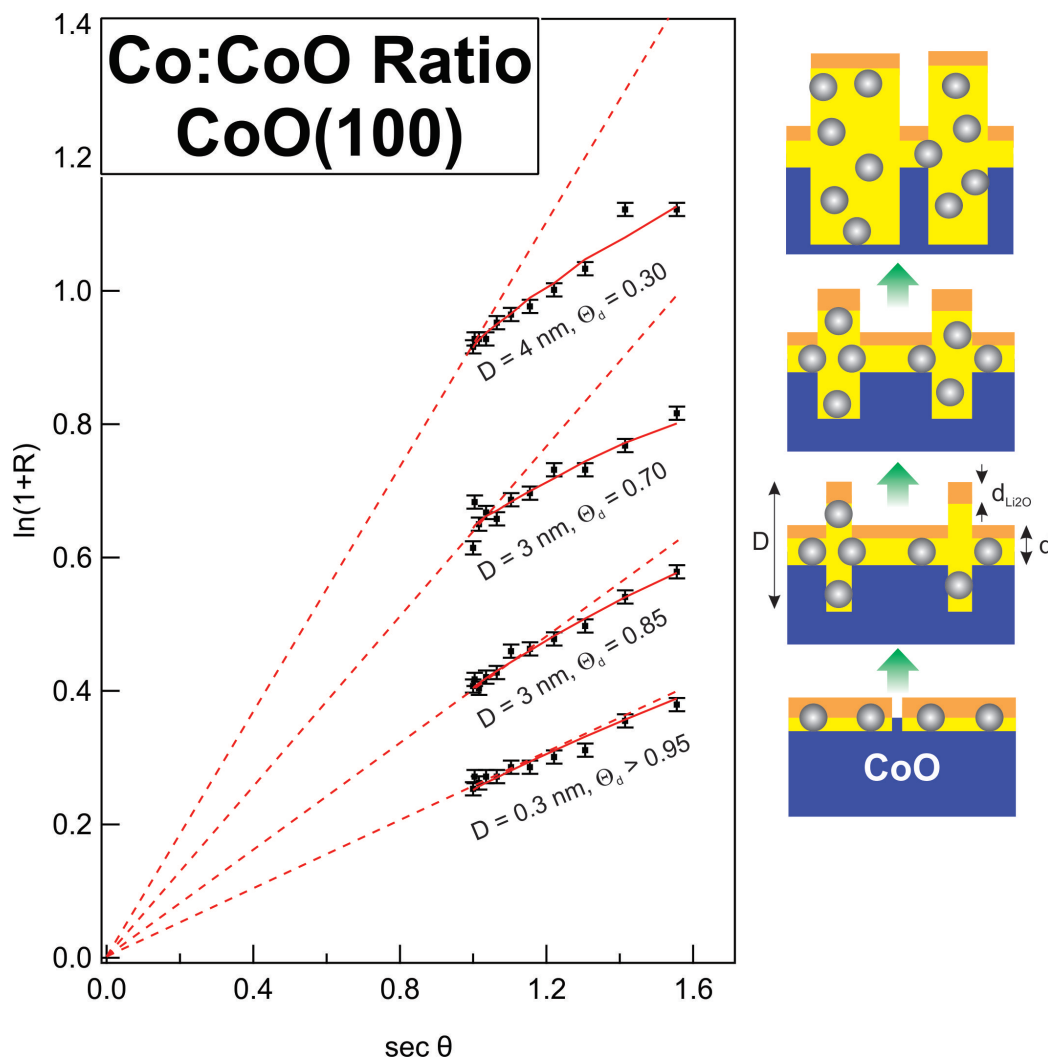


Figure 6.13: ARXPS data of a CoO(100) film before and after a series of Li exposures. Dashed lines correspond to the the expected Co:CoO ratio for a uniformly thick Co + Li₂O overlayer on a CoO substrate.

These parameters of the model were then varied in order to minimize the combined error (sum of squares) of the $R(\theta)$ curves for each of the three peak ratios discussed above.

Figure 6.13 shows the linearized $R(\theta)$ plots for the Co:CoO ratio after several different Li exposures and corresponding models used to calculate the fits to the data (solid red curves). As discussed in Chapter 4, linearized $R(\theta)$ curves corresponding to uniformly thick overlayers should have (artificially extrapolated) y-intercepts that lie at the origin, as denoted by the dashed red lines. Hence, a visual analysis of the $R(\theta)$ curves suggests that the initial lithiation produced a uniformly thick overlayer, while subsequent lithiations yielded

overlayers with varying thicknesses. Indeed, the model that produced the best agreement with all three sets of $R(\theta)$ curves suggested that the initial Li exposure led to the reaction of nearly the entire top monolayer of the CoO(100) film, forming a uniform 0.3 nm thick layer of Li₂O and Co⁰. Upon the completion of the first set of ARXPS measurements, nearly all of the Li₂O had further oxidized to Li₂O₂. Upon the subsequent Li exposure, narrow tendrils of conversion regions permeated several nanometers into the CoO(100) film. The 200% expansion associated with this conversion reaction caused these regions to protrude from the CoO surface by an amount equal to their depth below the surface, thus leading to the 10-20 nm wide features observed in the STM images of Figures 6.9 and 6.11. The ARXPS model suggests that about 15% of the surface area was occupied by these highly-reacted regions. This is a larger fraction of the surface than the aforementioned STM images would suggest. However, the difficulty of imaging the insulating highly-reacted regions could have led to a selection bias in the measurements, i.e. regions with the least conversion were possible to image while regions with the most conversion were not.

Li Exposure	d (nm)	D (nm)	Θ_d	r^2
5 min	0.5 ± 0.1	0.5 ± 0.1	> 0.95	0.959
10 min	0.7 ± 0.1	3 ± 1	0.85 ± 0.05	0.975
15 min	0.8 ± 0.2	3 ± 1	0.70 ± 0.05	0.947
20 min	0.8 ± 0.2	4 ± 1	0.50 ± 0.05	0.916
25 min	0.8 ± 0.2	4 ± 1	0.30 ± 0.05	0.953
30 min	0.8 ± 0.2	5 ± 1	0.10 ± 0.05	0.899

Table 6.1: Depth and homogeneity of the Li-CoO(100) reaction front for different amounts of Li exposure

This heterogeneity in the reaction front can be attributed to preferential Li diffusion through surface defects or Li₂O/Co⁰ grain boundaries, as was seen in lithiated FeF₂(110). Higher Li doses caused the tendrils of reacted material to expand laterally, such that the fractional coverage of the highly-reacted regions Θ_D increased from 0.15 ± 0.05 to 0.70 ± 0.05 while both d and D remained nearly constant. This implies that, at 150°C, the Li diffusivity through the Li₂O/Co⁰ composite was significantly higher than the diffusivity directly into the CoO(100) surface. This can be understood from a purely geometric standpoint, since the rock salt (100) surface does not have channels that are large enough to accommodate

lithium diffusion, while the $\text{Li}_2\text{O}/\text{Co}^0$ nanocomposite has numerous grain boundaries. This expansion of the reacted regions continued upon subsequent Li exposures until nearly all of the $\text{CoO}(100)$ was reduced. Table 6.1 summarizes the progression of the reaction depth versus Li exposure.

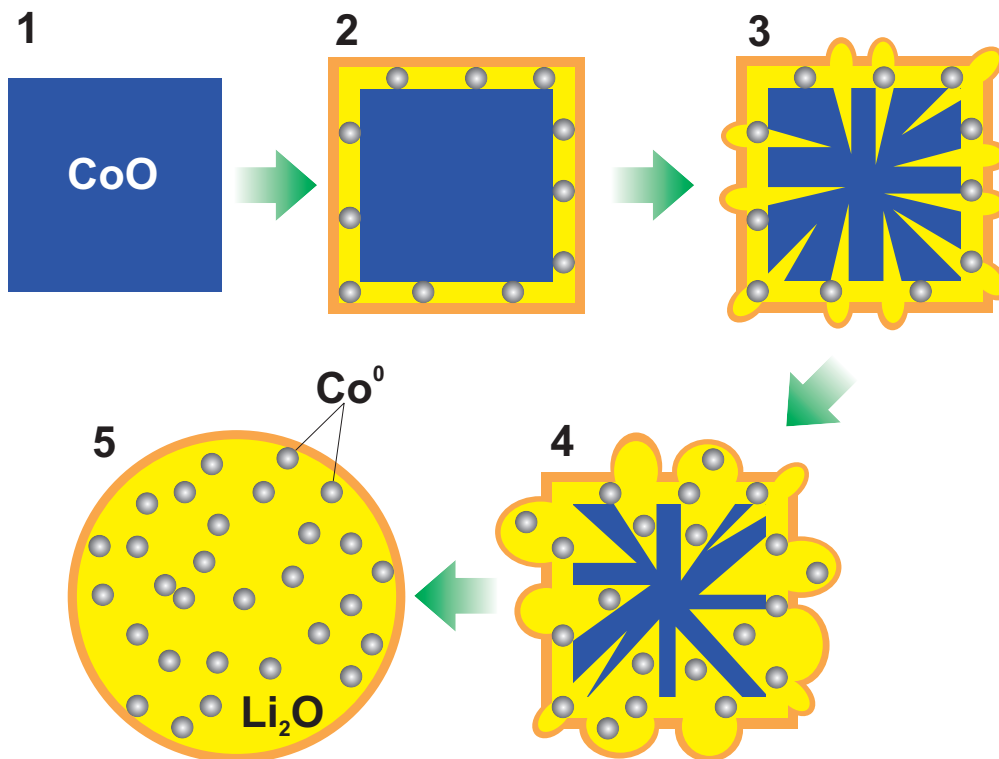


Figure 6.14: Schematic of the Li-CoO conversion reaction for a CoO nanoparticle with (100)-oriented crystalline faces.

This reaction schematic can now be applied to a full particle, assuming a cubic particle with only the (100)-like crystalline faces exposed. Figure 6.14 shows a cross-sectional schematic of the conversion reaction of a CoO nanoparticle whose crystalline faces are all oriented along (100)-like directions. (1) Starting with a cubic CoO particle, (2) lithium initially reacts with the surface layer to form an outer shell composed of 2-5 nm Co^0 particles embedded in an Li_2O matrix. The outer layer of this shell either oxidizes due to contamination in the electrolyte or else forms a carbon-rich SEI layer. (3) Thin tendrils of converted material with diameters on the order of 10 nm penetrate to the core of the CoO particle, causing material to expand outwards from the surface of the particle. (4) These tendrils expand and further reduce the particle, leaving some areas close to the surface still

unreacted. (5) The conversion reaction fully consumes the particle, leaving an $\text{Li}_2\text{O}/\text{Co}^0$ nanocomposite with an outer shell composed of Li_2O_2 and/or other SEI compounds.

6.3.2 Conversion of $\text{CoO}(111)$

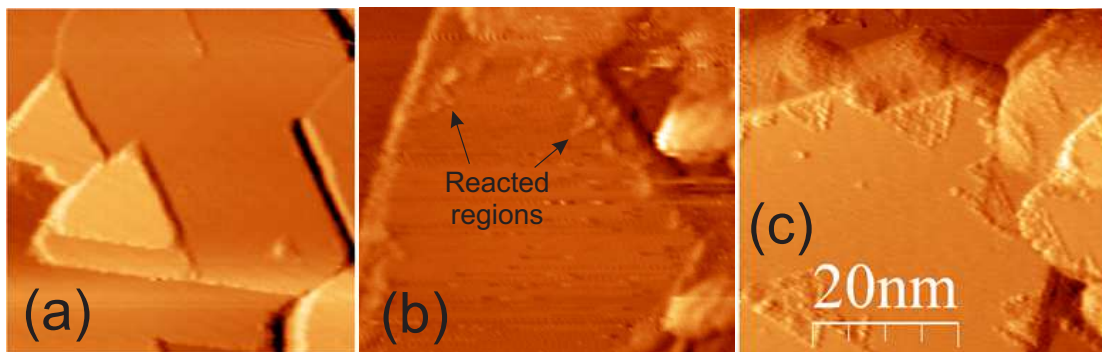


Figure 6.15: STM image of a $\text{CoO}(111)$ surface (a) as grown, (b) after exposure to 0.2 ML Li, and (c) after exposure to 0.4 ML Li. All images are $50 \times 50 \text{ nm}$ and were acquired at $+2.5 \text{ V}$ and 1 nA .

Figure 6.15 shows STM images of the $\text{CoO}(111)$ surface as grown and after two sequential lithium exposures. Upon initial exposure to lithium, triangular features with lateral dimensions of 2-5 nm and apparent heights of about 1 \AA appeared at the step edges and defect sites of the $\text{CoO}(111)$ surface, as shown in Figure 6.15(b). The boundaries of these features were found to align with the nearest neighbor directions of the $\text{CoO}(111)$ surface, i.e. the direction of the step edges in each CoO domain. Further Li exposures caused these features to expand laterally while remaining the same height and orientation with respect to the $\text{CoO}(111)$ lattice, as shown in Figure 6.15(c).

Figure 6.16 shows a high-resolution image of a $\text{CoO}(111)$ terrace after 0.4 ML of Li exposure. Note that each triangular features on this terrace is oriented with its sides parallel to the nearest neighbor directions of the lattice, denoted by the labels on the left side of the image. Small triangular structures within the larger features can also be seen at this resolution. The size of the smallest triangular features is about $3 \text{ \AA} \times 3 \text{ \AA}$, which corresponds to the lattice spacing of the $\text{CoO}(111)$ surface.

While elemental identification of these features was not possible with STM, geometric analysis of the CoO and Li_2O crystal structures provides some insight into the nature of

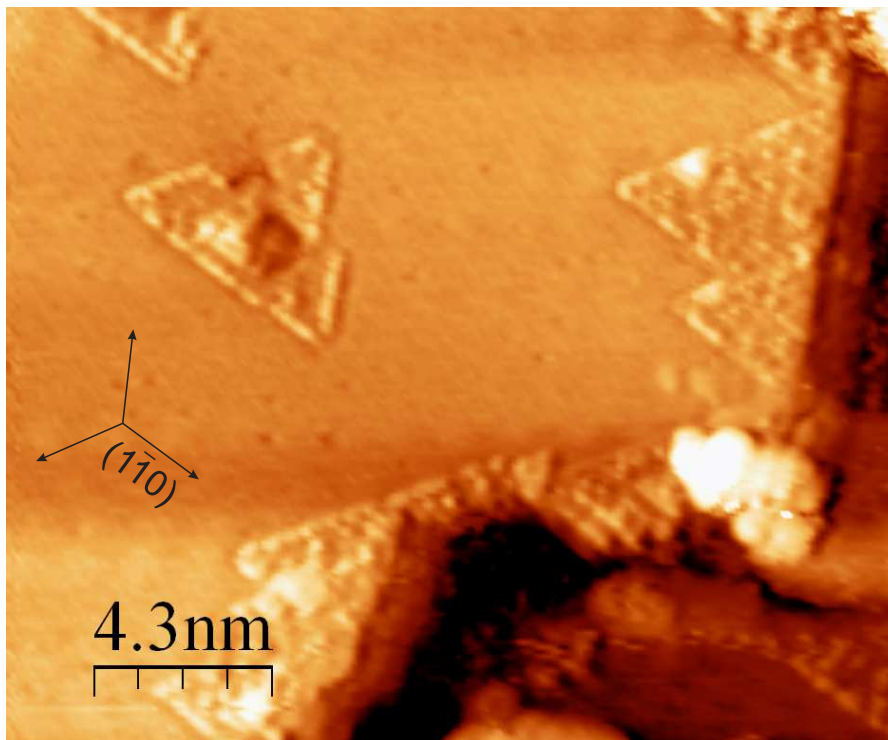


Figure 6.16: STM image of a CoO(111) surface after exposure to 0.4 ML Li at 150°. Image acquired at +2.5 V and 1 nA.

these surface structures. Li_2O crystallizes in the cubic antiferroite $\text{Fm}\bar{3}\text{m}$ structure with lattice constant $a = 4.62 \text{ \AA}$. [102, 146] This structure can be described as a cubic rock salt structure with half of the O^{2-} anions removed. Similar to CoO, the $\text{Li}_2\text{O}(111)$ surface can then be understood as alternating sheets of Li and O, with half of the oxygen sheets removed. The nearest neighbor spacing of the $\text{Li}_2\text{O}(111)$ surface, assuming bulk-like termination, is 3.26 \AA , which is 8% larger than that of the CoO(111) surface. Figure 6.17 shows a comparison of these surfaces.

Density functional theory calculations by Radin and coworkers [146] have suggested that the $\text{Li}_2\text{O}(111)$ surface is the most energetically favorable of the Li_2O terminations, with a surface energy ($30 \text{ meV}/\text{\AA}^2$) roughly half that of the $\text{Li}_2\text{O}(100)$ ($75 \text{ meV}/\text{\AA}^2$) and $\text{Li}_2\text{O}(110)$ ($56 \text{ meV}/\text{\AA}^2$) surfaces. Hence, it is reasonable to expect Li_2O evolved from the conversion reaction to form features which predominantly expose the (111) surface. A structure of this type can be easily accommodated by forming an epitaxial layer of $\text{Li}_2\text{O}(111)$ atop the CoO(111) surface, wherein the Li_2O overlayer consumes the topmost layer of O^{2-} anions

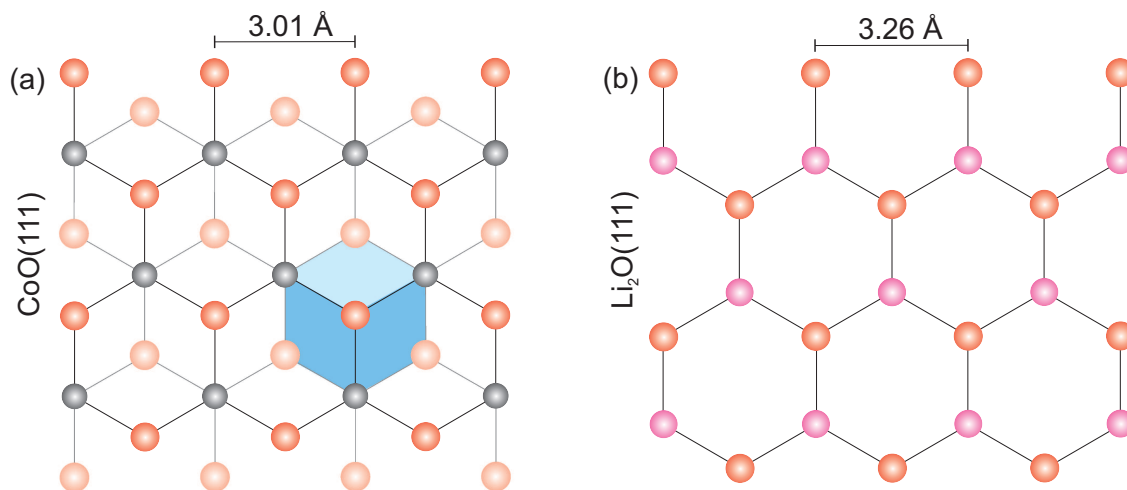


Figure 6.17: Crystalline structures of the $\text{CoO}(111)$ and $\text{Li}_2\text{O}(111)$ surfaces. Co^{2+} ions are gray, surface (subsurface) O^{2-} ions are red (light red), and Li^+ ions are pink.

from the CoO surface, thereby reducing the Co^{2+} cations in the second layer to Co^0 . This would have the added energetically favorable effect of reducing the polarity of the CoO surface. Furthermore, since the energy of the (110)-like surfaces of Li_2O is slightly less than that of the (100)-like surfaces, the Li_2O domains can be expected to terminate with (110)-like facets, which would run parallel to the nearest-neighbor directions of the (111) surface, as seen in the STM images of Figures 6.15 and 6.16. Consequently, the triangular features observed in these images are attributed to the epitaxial growth of $\text{Li}_2\text{O}(111)$ on the $\text{CoO}(111)$ surface.

Once again, STM imaging was not possible for higher Li exposures due to the insulating nature of the Li_2O and Li_2O_2 reaction products. However, ARXPS could again be used to determine how the conversion reaction proceeded into the bulk of the $\text{CoO}(111)$ film. It is important to re-emphasize that the $\text{CoO}(111)$ films were not synthesized in the XPS chamber, and hence were exposed to air during the transfer from the growth chamber to the XPS chamber. This likely caused some faceting of the surface, as well as the adsorption of water and carbonaceous contamination. However, the stoichiometry and chemical states of the reaction products were found to be exactly the same as those of the $\text{Li-CoO}(100)$ reaction. The most pronounced difference between the (100) and (111) films was the variation in the $\text{Co}:\text{CoO}$ ratio as a function of electron emission angle, suggesting that the uniformity of the

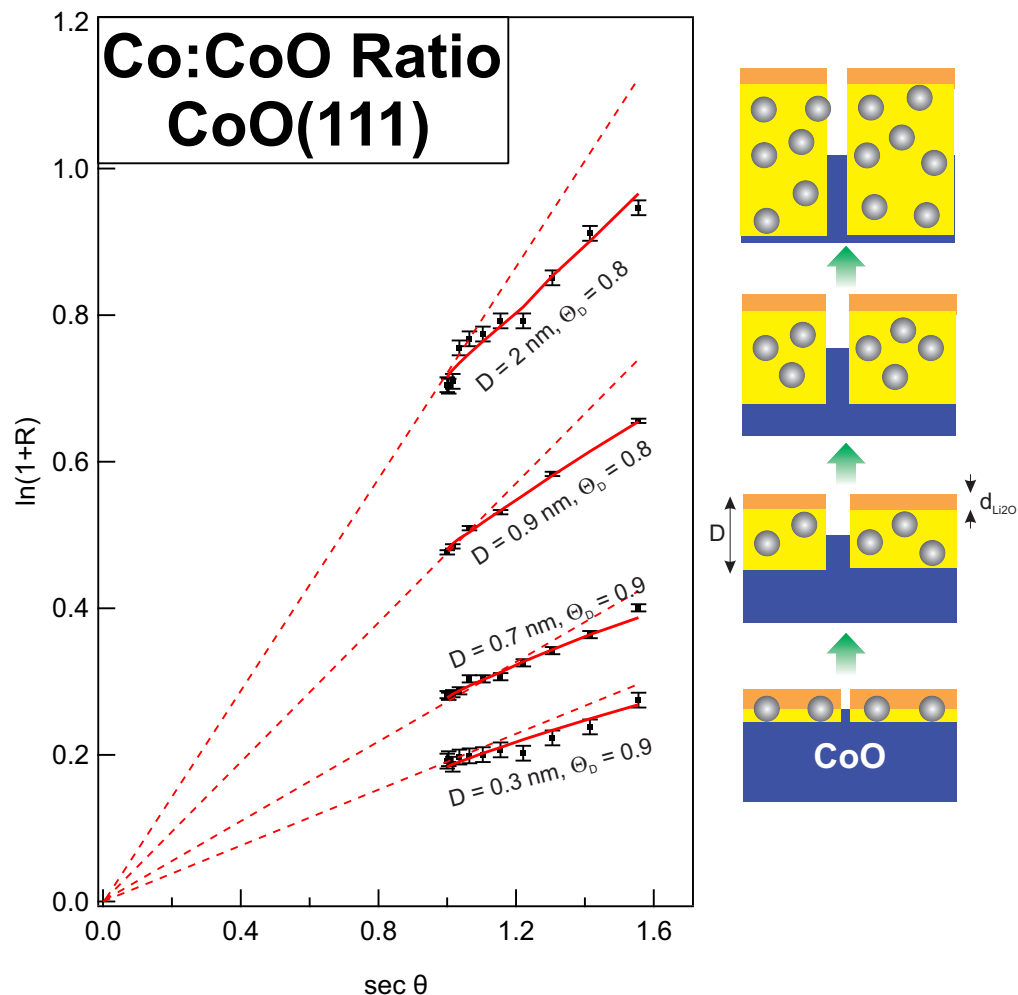


Figure 6.18: ARXPS data of a CoO(111) film for four different amounts of Li exposure. Dashed lines correspond to the the expected Co:CoO ratio for a uniformly thick Co + Li₂O overlayer on a CoO substrate.

Li-CoO(111) reaction was different from that of the Li-CoO(100) reaction. The linearized $R(\theta)$ plots for four different Li exposures and the associated schematic diagrams of the Li-CoO(111) reaction are shown in Figure 6.18. For all Li exposures, the geometry of the resulting CoO(111) was best modeled by an overlayer with majority thickness D , whose coverage Θ_D accounted for 80-90% of the CoO(111) surface. The remaining surface was assumed to consist of unreacted CoO.

For low Li exposures, the geometry of the Li-CoO(111) reaction was similar to that of the Li-CoO(100) reaction discussed previously. At this stage in the reaction, the thickness of the reacted layer was about 0.3 nm, and the conversion reaction had consumed 90% of

the surface layer of the CoO(111) film. However, further Li exposures caused the reaction front to proceed in a nearly planar fashion through the CoO film, leaving only 10-20% of the surface CoO unreacted. This can be understood as a results of the deposited lithium consuming each layer of oxygen in the film before the reaction proceeded to the next layer. The formation of Li_2O and Co^0 particles likely caused some anisotropy in the Li diffusivity into the surface of the partially reacted CoO(111) film, causing 10-20% of the CoO to remain unreacted. However, the reaction front was consistently more planar, and the thickness of the reacted overlayer more uniform, than that of the CoO(100) film discussed in the previous section. Table 6.2 summarizes the overlayer thicknesses and uniformity as a function of Li exposure.

Li Exposure	D (nm)	Θ_D	r^2
5 min	0.3 ± 0.1	> 0.90	0.874
10 min	0.7 ± 0.1	0.90 ± 0.05	0.967
15 min	0.9 ± 0.2	0.90 ± 0.05	0.995
20 min	1.5 ± 0.2	0.80 ± 0.05	0.987
30 min	2.0 ± 0.2	0.80 ± 0.05	0.980

Table 6.2: Depth and homogeneity of the Li-CoO(111) reaction front for different amounts of Li exposure

A cross sectional schematic can now be constructed to predict the behavior of a three-dimensional CoO(111) particle with only the (111)-like sides exposed. This is shown in Figure 6.19. As mentioned previously, a particle of this nature could be present in electrochemical cells with small amount of water contamination, due to the stabilizing effect of hydroxyl species on the CoO(111) surface. In this case, the reaction of a CoO particle would steadily progress from the outer shell of the particle inward, forming a uniformly thick overlayer of Co^0 and Li_2O over the surface of the unreacted material. This uniformity in the reaction would lead to more homogeneous degradation of a CoO-based electrode over time, which could be a desirable property in Li-ion batteries. This simple cross sectional model ignores the effect of the (100)-like surfaces of the CoO nanoparticle becoming exposed during the conversion reaction. In order to more accurately model a conversion reaction in three-dimensions, atomistic simulations are likely necessary.

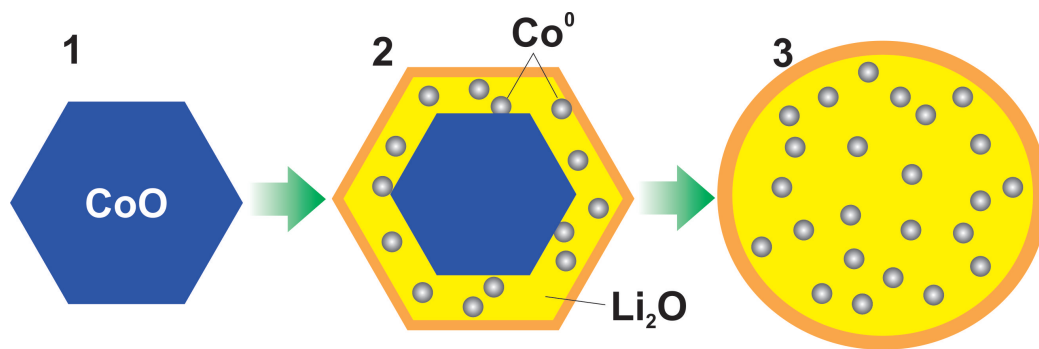


Figure 6.19: Schematic of the Li-CoO conversion reaction for a CoO nanoparticle with (111)-oriented crystalline faces.

6.4 Conclusion

CoO(100) and (111) thin films react with Li in dramatically different geometries, despite forming the same reaction products. In both cases, the surface layer of CoO is consumed upon small Li exposures. However, the formation of Co⁰ and Li₂O particles on the CoO(100) surface leads to anisotropic diffusion of Li into the remaining unreacted material, thus forming tendrils of reacted material that quickly reach the full depth of the CoO film. For CoO(111), the layers of O²⁻ anions are consumed in sequence, from the surface of the film to the bulk, thus leading to a planar reaction front. The differences observed here could be vital to the performance of CoO electrodes in electrochemical cells, since the uneven degradation of the electrode could be harmful to the overall performance of the cell.

In order to more accurately model the diffusion of Li on and into the different CoO surfaces, atomistic modeling, similar to the Li-FeF₂ reaction simulations discussed in Chapter 4, is likely necessary. Additionally, a full characterization of the temperature dependence of the Li-CoO reaction using both STM and ARXPS would provide insight into the role of Li diffusivity and Co⁰ particle ripening on the anisotropy of the Li-CoO(100) reaction. Lastly, the ARXPS measurements of the Li-CoO(111) measurements should be performed without first exposing the film to air, since the roughness of the initial surface could contribute to the slight inhomogeneity of the reaction observed in ARXPS.

Bibliography

- [1] J.-M. Tarascon, Phil. Trans. R. Soc. A. **368**, 3227 (2010).
- [2] J. Meija, T. Coplen, M. Berglund, W. Brand, P. D. Bivre, M. Grning, N. Holden, J. Irrgeher, R. Loss, T. Walczyk, et al., Pure Appl. Chem. **88**, 265 (2016).
- [3] D. Linden and T. R. Reddy, *Handbook of Batteries* (2002).
- [4] J. B. Goodenough and Y. Kim, Chem. Mater. **22**, 587 (2010).
- [5] J. Graetz, C. A. Yazami, and B. Fultz, Electrochemical and Solid-State Letters **9**, A194 (2003).
- [6] S. Oswald, K. Nikolowski, and H. Ehrenberg, Surface and Interface Analysis **42**, 916 (2010).
- [7] R. Malini, U. Uma, T. Sheela, M. Ganesan, and N. G. Renganathan, Ionics **15**, 301 (2009).
- [8] R. E. Doe, K. A. Persson, Y. S. Meng, and G. Ceder, Chem. Mater. **20**, 5274 (2008).
- [9] J. Cabana, L. Monconduit, D. Larcher, and M. R. Palacín, Adv. Mater. **22**, E170 (2010).
- [10] H. Li, P. Balaya, and J. Maier, Journal of The Electrochemical Society **151**, A1878 (2004).
- [11] F. Badway, F. Cosandey, N. Pereira, and G. G. Amatucci, Journal of the Electrochemical Society **150**, A1318 (2003).
- [12] F. Badway, N. Pereira, F. Cosandey, and G. G. Amatucci, Journal of the Electrochemical Society **150**, A1209 (2003).

- [13] G. Amatuucci and N. Pereira, *Journal of Fluorine Chemistry* **128**, 243 (2007).
- [14] M. Sina, R. Thorpe, S. Rangan, R. Bartynski, G. Amatuucci, and F. Cosandey, In preparation (2014).
- [15] J. Ko, K. Wiaderek, N. Pereira, T. Kinnibrugh, J. Kim, P. Chupas, K. Chapman, and G. Amatuucci, *Appl. Mat. Interfaces* **6**, 10858 (2014).
- [16] F. Wang, R. Robert, N. Chernova, N. Pereira, F. Omenya, F. Badway, X. Hua, M. Ruotolo, R. Zhang, L. Wu, et al., *J. Am. Chem. Soc.* **133**, 18828 (2011).
- [17] F. Wang, H.-C. Yu, L. Wu, N. Pereira, K. Thornton, A. V. der Ven, Y. Zhu, G. Amatuucci, and J. Graetz, *Nat. Comm.* **3**, 1 (2012).
- [18] F. Cosandey, D. Su, M. Sina, N. Pereira, and G. Amatuucci, *Micron* **43** (2011).
- [19] K. Wiaderek, O. Borkiewicz, E. Castillo-Martinez, R. Robert, N. Pereira, G. Amatuucci, C. Grey, P. Chupas, and K. Chapman, *J. Am. Chem. Soc.* **135**, 4070 (2013).
- [20] J.-S. Do and C.-H. Weng, *Journal of Power Sources* **146**, 482 (2005).
- [21] Y. Yu, C.-H. Chen, J.-L. Shui, and S. Xie, *Angew. Chem. Int. Ed.* **44**, 7085 (2005).
- [22] W. Yao, J. Yang, and Y. Nuli, *J. Electrochem. Soc.* **155**, A903 (2008).
- [23] F. Badway, I. Plitz, S. Grugeon, S. Laruelle, A. Gozdz, and J.-M. Tarascon, *Electrochem. Solid State Lett.* **5**, A115 (2002).
- [24] P. Poizot, S. Laruelle, L. Dupont, and J.-M. Tarascon, *Nature* **407**, 496 (2000).
- [25] S. Rangan, R. Thorpe, R. A. Bartynski, M. Sina, F. Cosandey, O. Celik, and D. D. T. Mastrogiovanni, *The Journal of Physical Chemistry C* **116**, 10498 (2012).
- [26] R. Thorpe, S. Rangan, R. Whitcomb, A. Basaran, T. Saerbeck, I. Schuller, and R. Bartynski, *Phys. Chem. Chem. Phys.* **17**, 15218 (2015).
- [27] S. Rangan, R. Thorpe, R. A. Bartynski, M. Sina, F. Cosandey, O. Celik, and D. Mastrogiovanni, *J. Phys. Chem. C* **116**, 10498 (2012).

- [28] R. Thorpe, S. Rangan, A. Howansky, and R. Bartynski, In Preparation (2016).
- [29] J. F. Watts and J. Wolstenholme, *An Introduction to Surface Analysis by XPS and AES* (2003).
- [30] A. Roth, *Vacuum Technology* (Elsevier Science Publishers, 1976).
- [31] J. O'Hanlon, *A User's Guide to Vacuum Technology* (John Wiley and Sons, 1980).
- [32] D. Woodruff and T. Delchar, *Modern Techniques of Surface Science* (1994).
- [33] J. Sakurai, *Modern Quantum Mechanics* (Addison-Wesley Publishing Company, 1994).
- [34] J. G. Ferreira and M. T. Ramos, *X-Ray Spectroscopy in Atomic and Solid State Physics* (Plenum Press, 1988).
- [35] J. H. Scofield, *Theoretical Photoionization Cross Sections from 1 to 1500 keV* (1973), URL <http://www.osti.gov/scitech/servlets/purl/4545040>.
- [36] J. Waber and D. Cromer, J. Chem. Phys. **42** (1965).
- [37] V. Schmidt, *Electron Spectrometry of Atoms using Synchrotron Radiation* (Cambridge University Press, 1997).
- [38] J. Fuggle and S. Alvarado, Phys. Rev. A **22** (1980).
- [39] F. de Groot and A. Kotani, *Core Level Spectroscopy of Solids* (Taylor & Francis Group, LLC, 2008).
- [40] S. Doniach and M. Sunjic, J. Phys. C **3** (1970).
- [41] C. Fadley, J. Elec. Spec. and Rel. Phen. **178-179**, 2 (2010).
- [42] A. Zangwill, *Physics at Surfaces* (1988).
- [43] N. Stoffel and P. Johnson, Nuc. Instr. and Meth. in Phys. Res. **A234**, 230 (1985).
- [44] P. Johnson, S. Hulbert, R. Garrett, and M. Howells, Rev. Sci. Instr. **57**, 1324 (1986).

- [45] S. Krause, A. Scholl, and E. Umbaach, Phys. Rev. B **91** (2015).
- [46] J. M. Cowley, *Diffraction Physics*, vol. 3 (Elsevier, 1995), 3rd ed.
- [47] N. Cabrera and N. Mott, Rep. Prog. Phys. **12**, 163 (1948).
- [48] S. R. Qiu, H.-F. Lai, and J. A. Yarmoff, Physical Review Letters **85**, 1492 (2000).
- [49] S. R. Qiu and J. A. Yarmoff, Physical Review B **63**, 1 (2000).
- [50] Y. Ma, G. Lockwood, and S. Garofalini, J. Phys. Chem. C **115**, 24198 (2011).
- [51] H. Perkins and Y. Hazony, Phys. Rev. B **5**, 7 (1972).
- [52] V. L. Chevrier, G. Hautier, R. E. Doe, G. Ceder, S. Rangan, and R. A. Bartynski, Unpublished (2010).
- [53] G. Racah, Phys. Rev. **62**, 438 (1942).
- [54] Y. Tanabe and S. Sugano, J. Phys. Soc. Jpn. **9**, 753 (1954).
- [55] Y. Tanabe and S. Sugano, J. Phys. Soc. Jpn. **9**, 766 (1954).
- [56] Y. Tanabe and S. Sugano, J. Phys. Soc. Jpn. **11**, 864 (1956).
- [57] T. Kambara, J. Phys. Soc. Japan **24**, 1242 (1968).
- [58] R. T. Poole, J. D. Riley, J. G. Jenkin, J. Liesegang, and R. C. G. Leckey, Phys. Rev. B **13**, 2620 (1976).
- [59] C. Sugiura, Journal of the Physical Society of Japan **60**, 2710 (1991).
- [60] S. Nakai, A. Kawata, M. Ohashi, M. Kitamura, C. Sugiura, T. Mitsuishi, and H. Maezawa, Physical Review B **37**, 10895 (1988).
- [61] T. E. Westre, P. Kennepohl, J. G. DeWitt, B. Hedman, K. O. Hodgson, and E. I. Solomon, Journal of the American Chemical Society **119**, 6297 (1997).
- [62] F. Cosandey, J. F. Al-Sharab, F. Badway, G. G. Amatucci, and P. Stadelmann, Microscopy and Microanalysis **13**, 87 (2007).

- [63] J. Pištora, M. Lesnák, E. Lišková, Š Višnovský, I. Harward, P. Maslankiewicz, K. Balin, Z. Celinski, J. Mistrk, T. Yamaguchi, et al., *Journal of Physics D* **43**, 155301 (2010).
- [64] R. Gupta and S. Sen, *Physical Review B* **10**, 71 (1974).
- [65] R. Gupta and S. Sen, *Physical Review B* **12**, 15 (1975).
- [66] A. Grosvenor, B. Kobe, M. Biesinger, and N. McIntyre, *Surf. Interface Anal.* **36**, 1564 (2004).
- [67] R. Gupta and S. Sen, *Physical Review B* **10**, 71 (1974).
- [68] R. Gupta and S. Sen, *Physical Review B* **12**, 15 (1975).
- [69] W. Pardee, G. Mahan, D. Eastman, R. Pollak, L. Ley, F. McFeely, S. Kowalczyk, and D. Shirley, *Phys. Rev. B* **11**, 3614 (1975).
- [70] L. Yin, I. Adler, L. Matienzo, and S. Grim, *Chem. Phys. Lett* **24**, 81 (1974).
- [71] P. A. van Aken, V. J. Styrsa, B. Liebscher, A. B. Woodland, and G. J. Redhammer, *Physics and Chemistry of Minerals* **26**, 584 (1999).
- [72] C. Ro and R. W. Linton, *Surf. Sci. Spec.* **1**, 277 (1992).
- [73] R. Poole, J. Jenkins, J. Liesegang, and R. Leckey, *Phys. Rev. B* **11**, 5179 (1975).
- [74] D. Lapiano-Smith, E. Eklund, and F. Himpsel, *Appl. Phys. Lett.* **59**, 2174 (1991).
- [75] D. Roessler and W. Walker, *J. Phys. Chem. Solids* **28**, 1507 (1967).
- [76] F. Cosandey, D. Su, M. Sina, N. Pereira, and G. Amatucci, *Micron* **43**, 22 (2012).
- [77] Y. Ma and S. Garofalini, *J. Am. Chem. Soc.* **134**, 8205 (2012).
- [78] R. Shannon, *Acta Cryst.* **A32**, 751 (1976).
- [79] J. Slater, *J. Chem. Phys.* **41** (1964).
- [80] A. V. der Ven and G. Ceder, *Electrochem. Solid-State Lett.* **3**, 301 (2000).

- [81] G. H. Vineyard, J. Phys. Chem. Solids **3**, 121 (1957).
- [82] Y. Ma and S. Garofalini, Phys. Chem. Chem. Phys. **16**, 11690 (2014).
- [83] J. Nogues, T. Moran, D. Lederman, I. Schuller, and K. Rao, Phys. Rev. B **59**, 6984 (1999).
- [84] Z.-P. Li, J. Eisenmenger, C. W. Miller, and I. K. Schuller, Phys. Rev. Lett. **96** (2006).
- [85] V. Holy, J. Kubena, I. Ohlidal, K. Lischka, and W. Plotz, Phys. Rev. B **47**, 15896 (1993).
- [86] A. Nelson, J. Appl. Cryst. **39**, 273 (2006).
- [87] T. Fuji, F. de Groot, G. Sawatzky, F. Voogt, T. Hibma, and K. Okada, Phys. Rev. B **59**, 3195 (1999).
- [88] S. Kerber, J. Bruckner, K. Wozniak, S. Seal, S. Hardcastle, and T. Barr, J. Vac. Sci. Tech. A **14**, 1314 (1996).
- [89] S. Yamamoto, H. Bluhm, K. Anderson, G. Ketteler, H. Ogasawara, M. Salmeron, and A. Nilsson, J. Phys. Cond. Matt. **20** (2008).
- [90] T. L. Barr and S. Seal, J. Vac. Sci. Tech. **13**, 1239 (1995).
- [91] P. C. Graat and M. A. Somers, Applied Surface Science **100**, 36 (1996).
- [92] M. Kasrai and D. Urch, J. Chem. Soc., Faraday Trans. 2 **75**, 1522 (1979).
- [93] C. Powell and A. Jablonski, *NIST Electron Effective-Attenuation-Length Database, Version 1.3, SRD 82* (National Institute of Standards and Technology, Gaithersburg, MD, 2011).
- [94] A. Jablonski and C. Powell, Surf. Sci. Rep. **47** (2002).
- [95] A. Jablonski and C. Powell, Surf. Sci. **520** (2002).
- [96] C. Powell and A. Jablonski, Nucl. Instr. Meth. Phys. Res. **A601** (2009).

- [97] S. K. Das, S. Xu, A.-D. Emwas, Y. Y. Lu, S. Srivastava, and L. Archer, *Energy Environ. Sci.* **5**, 8927 (2012).
- [98] T. Ogasawara, A. Débart, M. Holzapfel, P. Novák, and P. Bruce, *J. Am. Chem. Soc.* **128**, 1390 (2006).
- [99] J. Christenson, P. Albertus, R. Sanchez-Carrera, T. Lohmann, B. Kozinsky, R. Liedtke, J. Ahmed, and A. Kojic, *J. Electrochem. Soc.* **159**, R1 (2012).
- [100] Y.-C. Lu, E. Crumlin, G. Veith, J. Harding, E. Mutoro, L. Baggetto, N. Dudney, Z. Liu, and Y. Shao-Horn, *Nature Scientific Reports* **2** (2012).
- [101] S. P. Ong, Y. Mo, and G. Ceder, *Phys. Rev. B* **85**, 081105 (2012).
- [102] M. Radin, J. Rodriguez, and D. Siegel, *Proceedings of the Battery Congress* **60** (2011).
- [103] R. Kannan and M. Seehra, *Phys. Rev. B* **35**, 6847 (1987).
- [104] P. Silinsky and M. Seehra, *Phys. Rev. B* **24**, 419 (1981).
- [105] J. van Elp, W. Eskes, P. Kuiper, G. Sawatzky, F. de Groot, and T. Turner, *Physical Review B* **44**, 6090 (1991).
- [106] K. Okada and A. Kotani, *J. Phys. Soc. Japan* **61**, 449 (1992).
- [107] K. S. Kim, *Physical Review B* **11**, 2177 (1975).
- [108] R. Dedryvere, S. Laruelle, S. Grugeon, P. Poizot, D. Gonbeau, and J.-M. Tarascon, *Chem. Mater.* **16**, 1056 (2004).
- [109] G. Thornton, N. Brookes, D. L.-Law, D. Warburton, and P. Wincott, *Physica Scripta* **41**, 625 (1990).
- [110] J. Mackay and V. Henrich, *Phys. Rev. B* **39**, 6156 (1989).
- [111] Z.-X. Shen, J. Allen, and P. e. a. Lindberg, *Phys. Rev. B* **42**, 1817 (1990).
- [112] C. Rödl, F. Fuchs, J. Furthmüller, and F. Bechstedt, *Phys. Rev. B* **79**, 235114 (2009).
- [113] R. Eder, *Phys. Rev. B* **78**, 115111 (2008).

- [114] C. Mitterbauer, G. Kothleitner, W. Grogger, H. Zandbergen, B. Freitag, P. Tiemeijer, and F. Hofer, *Ultramicroscopy* **96**, 469 (2003).
- [115] E. Kurmaev, R. Wilks, A. Moewes, L. Finkelstein, S. Shamin, and J. Kunes, *Phys. Rev. B* **77**, 165127 (2008).
- [116] G. Pratt Jr. and R. Coelho, *Physical Review* **116**, 281 (1959).
- [117] Q.-H. Wu, A. Thissen, and W. Jaegermann, *Applied Surface Science* **250** (2005).
- [118] Q.-H. Wu, A. Thissen, and W. Jaegermann, *Surface Science* **578**, 203 (2005).
- [119] D. Ensling, A. Thissen, and W. Jaegermann, *Applied Surface Science* **255**, 2517 (2008).
- [120] F. Wang, R. Robert, N. A. Chernova, N. Pereira, F. Omenya, F. Badway, X. Hua, M. Ruotolo, R. Zhang, L. Wu, et al., *Journal of the American Chemical Society* **133**, 18828 (2011).
- [121] D. A. Shirley, *Phys. Rev. B* **5**, 4709 (1972).
- [122] R. Black, S. H. Oh, J.-H. Lee, T. Yim, B. Adams, and L. F. Nazar, *Journal of the American Chemical Society* **134**, 2902 (2012).
- [123] M. Dolle, P. Poizot, L. Dupont, and J.-M. Tarascon, *Electrochemical and Solid-State Letters* **5**, A18 (2002).
- [124] S. Grugeon, S. Laruelle, L. Dupont, and J.-M. Tarascon, *Solid State Sciences* **5**, 895 (2003).
- [125] C. Giovanardi, L. Hammer, and K. Heinz, *Phys. Rev. B* **74**, 6214 (2006).
- [126] K. Refson, R. Wogelius, D. Fraser, M. Payne, M. Lee, and V. Milman, *Phys. Rev. B* **52**, 10823 (1995).
- [127] I. Sebastian, T. Bertrams, K. Meinel, and H. Neddermeyer, *Faraday Discuss.* **114**, 129 (1999).
- [128] I. Sebastian and H. Neddermeyer, *Surface Science* **454-456**, 771 (2000).

- [129] M. Heiler, A. Chasse, K.-M. Schindler, M. Hollering, and H. Neddermeyer, Surface Science **454-456**, 36 (2000).
- [130] C. Hagendorf, R. Shantyr, K. Meinel, K.-M. Schindler, and H. Neddermeyer, Surface Science **532-535**, 346 (2003).
- [131] S. Sindhu, M. Heiler, K.-M. Schindler, W. Widdra, and H. Neddermeyer, Surface Science **566-568**, 471 (2004).
- [132] K. Heinz, G. Schmidt, L. Hammer, and K. Muller, Phys. Rev. B **32**, 6214 (1985).
- [133] A. Schmidt, W. Meier, L. Hammer, and K. Heinz, J. Phys. Cond. Matt. **14**, 12353 (2002).
- [134] L. Hammer, W. Meier, A. Klein, P. Landfried, A. Schmidt, and K. Heinz, Phys. Rev. Lett. **91** (2003).
- [135] W. Meyer, K. Biedermann, M. Gubo, L. Hammer, and K. Heinz, J. Phys. Cond. Matt. **20** (2008).
- [136] K. Heinz and L. Hammer, Prog. in Surf. Sci. **84**, 2 (2009).
- [137] K. Biedermann, M. Gubo, L. Hammer, and K. Heinz, J. Phys. Cond. Matt. **21** (2009).
- [138] M. Gubo, C. Ebensperger, W. Meyer, L. Hammer, and K. Heinz, J. Phys. Cond. Matt. **21** (2009).
- [139] C. Ebensperger, M. Gubo, W. Meyer, L. Hammer, and K. Heinz, Phys. Rev. B **81** (2010).
- [140] M. Gubo, L. Hammer, and K. Heinz, Phys. Rev. B **85** (2012).
- [141] K. Heinz and L. Hammer, J. Phys. Cond. Matt. **25** (2013).
- [142] C. Kittel, *Introduction to Solid State Physics* (John Wiley and Sons, 2005), 8th ed.
- [143] U. Das, K. C. Lau, P. C. Redfern, and L. A. Curtiss, J. Phys. Chem. Lett. **5**, 813 (2014).

- [144] L. Xu and G. Henkelman, Phys. Rev. B **82** (2010).
- [145] L. Liu, V. Henrich, W. Ellis, and I. Shindo, Phys. Rev. B **54**, 2236 (1996).
- [146] M. Radin, F. Tian, and D. Siegel, J. Mater. Sci. **47**, 7564 (2012).
- [147] R. Thorpe, S. Rangan, M. Sina, F. Cosandey, and R. A. Bartynski, J. Phys. Chem. C **117**, 14518 (2013).

Appendix A

Kinetic Theory of Gases

The use of ultra-high vacuum chambers for electron-based techniques is motivated by the need for clean sample surfaces and a high mean free path for electrons in the chamber. The following derivations provide simple derivations of the pressures needed in order to ensure that both of these criteria are met. The goal of these derivations was to use well-known physical constants whenever possible.

A.1 Monolayer Surface Contamination

This section discusses the formation of contaminants on sample surfaces using the kinetic theory of gases. The derivation below assumes that the ideal gas law is applicable at all gas pressures, although it is typically only useful in low-pressure regimes where inter-molecular collisions are negligible. However, the final result will be applied to an ultra-high vacuum regime, where the low density of gases makes the ideal gas law a reasonable approximation.

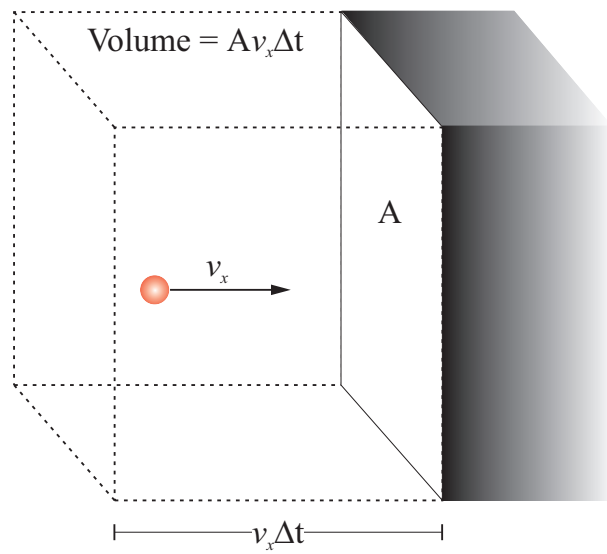


Figure A.1: A particle impinging on a surface

A.1.1 Simple Approximation

Consider a flat surface region with area A in a gas of particles, as shown in Figure A.1. The pressure of a gas on a surface is given by the average force per unit area. This force is equal to the average momentum change of a particle upon collision with the surface multiplied by the number of collisions, N_{coll} :

$$P = \frac{F}{A} = \frac{N_{\text{coll}}}{A} \left\langle \frac{m \Delta v_x}{\Delta t} \right\rangle. \quad (\text{A.1})$$

If we assume that every particle sticks to the surface, then the average momentum change is simply equal to the average initial momentum of the particle:

$$P = \frac{N_{\text{coll}}}{A} \frac{m \langle v_x \rangle}{\Delta t}. \quad (\text{A.2})$$

The number of collisions per unit area per unit time can then be obtained by rearranging terms:

$$\frac{N_{\text{coll}}}{A \Delta t} = \frac{P}{m \langle v_x \rangle}. \quad (\text{A.3})$$

If we approximate the average x -velocity $\langle v_x \rangle$ by the root mean square velocity $v_{x,\text{rms}} = \sqrt{\langle v_x^2 \rangle}$, we can use the following relationship:

$$v_{\text{rms}} = \sqrt{\langle v^2 \rangle} = \sqrt{\langle v_x^2 + v_y^2 + v_z^2 \rangle} \quad (\text{A.4})$$

$$= \sqrt{\langle 3v_x^2 \rangle} \quad (\text{A.5})$$

$$= \sqrt{3} \sqrt{\langle v_x^2 \rangle}. \quad (\text{A.6})$$

Since $v_{\text{rms}} = \sqrt{\frac{3kT}{m}}$, where k is Boltzmann's constant and T is temperature, we obtain the following result:

$$\langle v_x \rangle \approx v_{x,\text{rms}} = \sqrt{\frac{kT}{m}}. \quad (\text{A.7})$$

Equation A.3 can then be rewritten as

$$\frac{N_{\text{coll}}}{A \Delta t} \approx \frac{P}{m} \frac{m}{kT} = \frac{nkT}{m} \sqrt{\frac{m}{kT}} = n \sqrt{\frac{kT}{m}}. \quad (\text{A.8})$$

We can then solve this equation by plugging in values for n , kT , and m . Assuming standard temperature and pressure conditions, $n = 1$ mol per 24 liters, $kT = 25$ meV, and $m = 18 \text{ GeV}/c^2$ for water molecules, where $c = 3 \times 10^{10} \text{ cm/s}$ is the speed of light. We then have

$$\frac{N_{coll}}{A\Delta t} \approx \frac{6 \times 10^{23}}{24 \text{ L}} \left(\frac{1 \text{ L}}{1000 \text{ cm}^3} \right) \sqrt{\frac{0.025 \text{ eV}}{18 \times 10^9 \text{ eV}/c^2}} \quad (\text{A.9})$$

$$\approx 10^{24} \text{ Collisions/cm}^2/\text{s} \quad (\text{A.10})$$

Assuming the surface has a lattice spacing of about 3 \AA , a surface coverage of one monolayer corresponds to

$$1 \text{ ML} = \left(\frac{1 \text{ Collision}}{3 \times 10^{-10} \text{ m}} \right)^2 \left(\frac{1 \text{ m}}{10 \text{ cm}} \right)^2 \approx 10^{15} \text{ Collisions/cm}^2. \quad (\text{A.11})$$

Hence, the rate of surface coverage is

$$\frac{N_{coll}}{A\Delta t} \approx 1 \text{ ML/s} \quad (\text{A.12})$$

A.1.2 Rigorous Derivation

Consider the surface shown in Figure A.1. A particle whose velocity is $\vec{v} = v_x \hat{x} + v_y \hat{y} + v_z \hat{z}$ moves towards the surface during a short time interval Δt . The particle will impinge on the wall in this time interval if it is located within a distance of $v_x \Delta t$ of the wall. A volume $v_x \Delta t$ can then be defined near the surface. The number of particles contained in this volume is then given by

$$N_{\text{molecules}} = n A v_x \Delta t \quad (\text{A.13})$$

where n is the number density of molecules in the gas. The number of molecules with x -component of velocity v_x is

$$N_{v_x} = n A \Delta t v_x f(v_x) dv_x \quad (\text{A.14})$$

where $f(v_x)$ is the velocity probability distribution function in the x dimension, which is simply the one-dimensional Maxwell-Boltzmann velocity distribution, given by

$$f(v_x) = \sqrt{\frac{m}{2\pi kT}} \exp\left(-\frac{mv_x^2}{2kT}\right). \quad (\text{A.15})$$

The number of collisions with the surface can then be calculated by

$$N_{\text{coll}} = nA\Delta t \int_{-\infty}^{\infty} v_x f(v_x) dv_x \quad (\text{A.16})$$

$$= 2nA\Delta t \int_0^{\infty} v_x f(v_x) dv_x \quad (\text{A.17})$$

$$= nA\Delta t \sqrt{\frac{2kT}{\pi m}}. \quad (\text{A.18})$$

The number of collisions per unit area per unit time is then

$$\frac{N_{\text{coll}}}{A\Delta t} = \sqrt{\frac{2}{\pi}} n \sqrt{\frac{kt}{m}}. \quad (\text{A.19})$$

Note that this differs from the previously calculated value by only a factor of $\sqrt{2/\pi} = 0.8$. Hence, the amount of time to form one monolayer of contaminants is about one nanosecond.

A.2 Mean Free Path

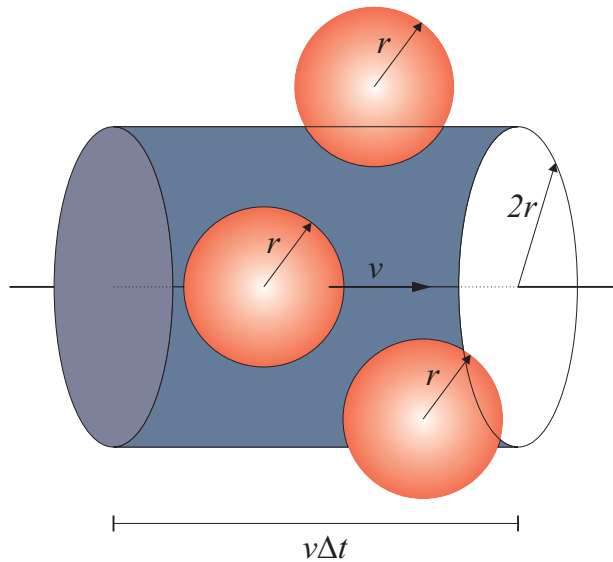


Figure A.2: A particle moving through a gas

A particle with radius r moving through a gas of identical particles sweeps out an interaction cross sectional area given by $\pi(2r)^2$. Note that the use of $2r$ instead of r accounts for the radius of other particles. Over a short time period of Δt , the particle sweeps out a cylinder whose volume given by

$$V = 4\pi r^2 \langle v \rangle \Delta t. \quad (\text{A.20})$$

The number of particles located in this volume is then given by nV , and the number of collisions per unit time is

$$\frac{N_{coll}}{\Delta t} = \frac{nV}{\Delta t} = 4\pi r^2 n \langle v \rangle. \quad (\text{A.21})$$

The average time between collisions is simply the reciprocal of this quantity:

$$\frac{\Delta t}{N} = \frac{1}{4\pi r^2 n \langle v \rangle}. \quad (\text{A.22})$$

We can then define the mean free path λ of the particle as the product of the time between collisions and the average velocity of the particle:

$$\lambda = \frac{\Delta t}{N_{coll}} \langle v \rangle \quad (\text{A.23})$$

$$= \frac{1}{4\pi r^2 n} \quad (\text{A.24})$$

At room temperature and atmospheric pressure, and assuming a radius of $r = 0.2 \text{ nm}$

$$\lambda_{\text{air}} = \left(\frac{24 \text{ L}}{6 \times 10^{23}} \right) \left(\frac{1000 \text{ cm}^3}{1 \text{ L}} \right) \left(\frac{10^7 \text{ nm}}{1 \text{ cm}} \right)^3 \left(\frac{1}{4\pi (0.2 \text{ nm})^2} \right) \quad (\text{A.25})$$

$$= 80 \text{ nm} \quad (\text{A.26})$$

In photoemission and inverse photoemission spectroscopy, the interaction between electrons and gases in the chamber should be minimized. Hence, the mean free path of electrons must be much greater than the dimensions of the chamber. Since vacuum chambers are typically on the order of 1 m in size, λ_{vacuum} must be 10^7 - 10^8 longer than λ_{air} , and thus, the vacuum chamber pressure must be below 10^{-8} atm or about 10^{-5} Torr . This is obviously a less stringent constraint on pressure than the one imposed by the previous argument.